ENERGETIC ELECTRON-INDUCED SINGLE EVENT UPSETS IN STATIC RANDOM ACCESS MEMORY

By

Michael Patrick King

Dissertation

Submitted to the Faculty of the

Graduate School of Vanderbilt University

in partial fulfillment of the requirements

for the degree of

DOCTOR OF PHILOSOPHY

in

Electrical Engineering

May 2014

Nashville, Tennessee

Approved:

Professor Robert A. Reed

Professor Robert A. Weller

Professor Marcus H. Mendenhall

Professor Ronald D. Schrimpf

Professor Richard F. Haglund

For my grandfather, Edward Gray, who was my greatest teacher.

ACKNOWLEDGMENTS

The people who have contributed and supported me during my education are an uncountable set.

My thanks must go out to my academic advisor Professor Robert A. Reed. He has been a source of encouragement, support, guidance, and sanity during the time I have spent at Vanderbilt. I would like to thank Professor Robert A. Weller for his good humor, enthusiasm, patience, and help over these many long years and especially during the the final few weeks. I would like to thank Professor Ron D. Schrimpf for his guidance, encouragement, and the many discussions on a variety of topics. I would like to thank Professor Marcus H. Mendenhall for working with me and helping me break down my most difficult problems. I would like to thank Professor Richard F. Haglund for his set of very interesting lectures on the subjects of condensed matter and solid-state physics, which had me excited to learn at a very early hour.

Additional thanks go to Professor Lloyd W. Massengill for his good spirits and guidance on a variety of topics, Professor T. Daniel Loveless for his friendship, and Professor Daniel M. Fleetwood for being a source of guidance, support, and being willing to share his knowledge and intuition. I would like to acknowledge the ISDE staff, which has been very helpful and supportive on many projects and collaborations.

To my friends from California, Tennessee, and everywhere in between, you have always been what anchors me. On the occasion I have lost my perspective,

you have all been there with a helping hand, encouragement, good company, and humor. I consider myself to be a particularly fortunate man for knowing each of you.

To my family who came along with me on this journey. Your love and unwavering faith helped me through the most difficult of times, I hope you know that. Thank you all.

Lastly, to my grandfather, Edward Gray. Thank you for teaching me to be responsible, respectable, and a good man.

Contents

List of Tables vi

List of Figures vii

1 Introduction 1

2 Background 6
- 2.1 Basic Interaction Mechanisms . . . 8
  - 2.1.1 Ion Transport . . . 9
  - 2.1.2 Electron Transport . . . 14
  - 2.1.3 Photon Transport . . . 18
- 2.2 Basic SRAM Topology and Operation . . . 23
- 2.3 Radiation Effects on SRAMs . . . 28
  - 2.3.1 Single-Event Upset in SRAMs . . . 28
  - 2.3.2 Low-Energy Proton-Induced SEUs . . . 36
  - 2.3.3 Muon-Induced SEUs . . . 41
  - 2.3.4 SRAM Cell Imprinting . . . 43
  - 2.3.5 Impact of Transient Radiation on SRAMs . . . 53
- 2.4 Radiation Environments . . . 57
  - 2.4.1 Solar Particle Environment . . . 59
  - 2.4.2 Galactic Cosmic Rays . . . 61
  - 2.4.3 Trapped Particle Environments . . . 65
- 2.5 Ionizing Particle Track Structure . . . 71

3 Experimental Investigation of Electron-Induced SEUs 78
- 3.1 Experimental Setup and Methods . . . 79
- 3.2 Experimental Results . . . 87
- 3.3 Comparison to Low-Energy Proton and Muon SEUs . . . 94

4 Simulation of Electron-Induced SEUs 97
- 4.1 Simulation of X-ray Energy Deposition in SRAMs . . . 97
- 4.2 Electron-Induced SEU Event Rates . . . 103
- 4.3 Impact of Delta-rays on Microelectronics . . . 113

5 Summary and Conclusions 122

Bibliography 124

List of Tables

2.1 Particle Radiations in Near-Earth Orbit and Some Properties 59

3.1 X-ray Supply Voltage, Exposure Time, and Fluence 89

List of Figures

1.1 The sequence of events in electron-induced SEUs is depicted in a series of image panels. The top left image shows a particle strike on the sensitive node of an SRAM indicated by a lightning bolt striking the drain of the nMOSFET *M1*. The top right image shows the absorption of the incident particle, in this case a 10 keV X-ray, and the generation of an energetic photo-electron. This energetic electron undergoes multiple scattering events eventually thermalizing within the sensitive volume of the SRAM. The energy loss of the energetic electron results in the generation of electron-hole pairs that are subsequently collected, as seen in the bottom left panel. Finally, the device- and circuit-level response is shown in the bottom right, where the SRAM transient response on the BL and $\overline{BL}$ nodes latch an error into the memory. . . 3

2.1 Stopping power in silicon is plotted as a function of energy per unit mass (MeV/u) for protons, alpha particles, carbon, oxygen, and iron. Stopping power was calculated using the SRIM/TRIM codes. 11
2.2 CSDA range in silicon as a function of incident ion energy per unit mass for protons, alphas, carbon, oxygen, and iron ions. 13
2.3 Scattering of an incident electron resulting in generation of a secondary electron 15
2.4 Total stopping power, $-\left(\frac{dE}{dx}\right)_{total}$, and CSDA range are plotted as a function of energy in silicon. Collisions dominate energy loss at electron energies less than 1 MeV. Radiative processes are more prevalent at higher electron energies. 18
2.5 The energy dependence of the three major types of photon interactions are shown. The lines shows the values of material Z and photon energy $\hbar\omega$ for which the two neighboring effects are approximately equal. . . 19
2.6 Absorption of an incident photon with energy $\hbar\omega$ resulting in the generation of an energetic photo-electron. Relaxation occurs through the emission of (a) fluorescent radiation or (b) Auger processes that result emission of a low energy electron or electrons. 21
2.7 Diagram of a Compton scattering event between an incident photon with energy $\hbar\omega$ and an electron. 22
2.8 The attenuation cross-section, μ, versus incident photon energy in silicon. 23
2.9 Basic SRAM circuit topology consists of two cross-coupled inverters and two access transistors. 25
2.10 Butterfly curves for 0.1 μm^2 6T-SRAM cell showing SNM of 220 mV, 180 mV and 148 mV at V_{dd}=0.9, 0.8 and 0.7 V respectively. 27

2.11 Current transients in an SRAM cell demonstrate the concept of critical charge. The transient corresponding to 0.23 pC of charge collection is insufficient to cause the SRAM cell to latch into an erroneous state. However, when the amount of collected charge is increased to 0.25 pC the resulting transient is latched into the SRAM cell, resulting in an error. 30
2.12 SPICE analysis of the critical charge dependence on supply voltage . 32
2.13 SEU cross-section bias dependence of an SRAM for alphas with energies 1.56, 3.38, and 5.49 MeV, with LETs (in the sensitive volume) of 1.52, 0.87, and 0.64 MeV-cm^2/mg, respectively. 33
2.14 Estimation of critical charge as a function of technology node feature size. 34
2.15 SRAM fails (an average of write *1* and write *0*) as a function of the incident angle for an SRAM array at 0.8 V, 1.2 V and 1.6 V using 1.5 MeV protons. 37
2.16 The SBU cross-section versus proton energy for both 45 nm and 65 nm SOI SRAMs. 38
2.17 Plot of the SRAM SEU cross-section (in arbitrary units) as a function of voltage for 5.0 MeV and 7.0 MeV alpha particles and for 1.0 MeV and 1.5 MeV protons. 40
2.18 Mass stopping power extracted from Geant4 for protons, pions, muons, and positrons in silicon. Alpha particle stopping power shown for reference. 42
2.19 Simulated muon kinetic energy distributions, as seen at the front of the part, corresponding to experimental momenta including upstream energy losses and straggling (bottom). Error counts for 65 nm, 45 nm, and 40 nm SRAMs versus estimated muon kinetic energy at 1.0 V bias (top). Dashed horizontal line represents an approximate muon-induced SEU cross section for reference. 44
2.20 Error counts for 65 nm SRAM versus supply voltage for approximately 400 keV muons produced by 21 MeV/c momentum selection. Dashed horizontal line represents an approximate muon-induced SEU cross section for reference. 45
2.21 ΔV_{th} versus time, for n-channel transistors irradiated to 1.0 Mrad(Si) and annealed at 25°C. 47
2.22 SRAM cell imbalance versus radiation and anneal time, based on the data of Figure 2.21. 48
2.23 Impact of STI radiation damage on the current-voltage characteristics of nMOSFET fabricated in TSMC 0.18 μm CMOS. 50

2.24 Worst-case Monte Carlo derived read SNM pre- and post-irradiation. The thin blue and dashed green lines show the post-irradiation SNM, while the thick red lines show the pre-irradiation response. The worst-case, i.e., the smallest box that fits within the "eyes" is improved after irradiation. 51
2.25 Pre-irradiation SRAM cell trip points measured driving the BL and $\overline{BL}$, shown in (a). BL_{ND} and $\overline{BL}_{ND}$ are normal distribution curves for the SRAM DC switch point. In (b), measured SRAM cell node trip points after irradiation to 1.5 Mrad(Si). The BL trip points are shifted up, i.e., the write margin is increased (easier write) and the $\overline{BL}$ write margin is reduced (it becomes more difficult to write). 52
2.26 Photocurrent waveforms, at a dose rate of 5×10^9 rad(Si)/sec for the (a) bulk and (b) epi cases. 55
2.27 Schematic representation of the power distribution with the SRAM cells shown as "black boxes". 56
2.28 Upset bit-map with no pre-test total dose for (a) 1.02×10^9,(b)1.08×10^9 and (c)1.16×10^9 rad(Si)/sec. 58
2.29 Daily fluences of > 0.88 MeV protons due to solar particle events between approximately 1974 and 2002. 61
2.30 The particle flux spectra computed by CREME96 for a Near-Earth Interplanetary or Geosynchronous orbit during the worst day scenario with 100 mils of aluminum shielding. Common species shown, all others omitted. 62
2.31 Abundances of particles species in the GCR spectrum up through Z = 28. 63
2.32 GCR energy spectra for protons, helium, oxygen and iron during solar maximum and solar minimum conditions. 64
2.33 The electron population with energies > 1 MeV as predicted by the AE-8 model for solar maximum conditions. 67
2.34 The trapped proton population with energies > 10 MeV as predicted by the AP-8 model for solar maximum conditions. 68
2.35 Time and energy dependence of the mean electron flux at geostationary altitudes over about 2.5 solar cycles. 69
2.36 Line plots of the differential electron fluxes as predicted by the inner region GIRE and GIRE2 models. 70
2.37 Differential flux spectrum for electrons in the Jovian and Europa environment phase of the Juno spacecraft mission to the Jupiter planetary system. 71
2.38 The spatial distribution of ionization energy in emulsion for incident particles with differing relative velocity. These calculations, based on Katz theory, describe the average dose deposited as a function of radial distance, t, from the incident ion track. 73

2.39 Calculated *e-h* pair density generation is shown as a function of radial distance from the ion track at a depth of 1 μm within a volume of silicon for (a) 395 MeV Cu and (b) 25 MeV Cu. 75
2.40 2.40(a) Cross-sectional TEM image showing thin composite oxide-nitride spacer on 25 nm wide gate at 90 nm pitch. 2.40(b) Top-down SEM image of the 0.1 μm^2 6T-SRAM cell after STI fill and gate-first metal gate patterning, with cell dimensions of 0.18 μm and 0.554 μm. . . . 76

3.1 An automated test system allows independent control of two Keithley 2410 SourceMeters for the SRAM test chip and test board interface through a LAN/GPIB gateway. Control commands are transmitted to the SRAM test board through a USB connection from a laptop. This system allows the supply voltage of the SRAM to be modulated *in situ*. The device under test is exposed to energetic X-rays under varied supply voltage conditions. 79
3.2 Example timing diagram for measuring upsets at reduced bias. Read and write operations are performed under nominal bias condition, V_{DDNOM}. During exposure the rail is reduced to a value, V_{DDEXP}, for the duration of the experiment. Upon conclusion of the exposure, the nominal rail is restored, a final read operation is performed, and any errors recorded. 81
3.3 X-ray and electron spectra produced by the ARACOR 4100 X-ray irradiator. The average energy is 10 keV and the maximum energy is 50 keV, corresponding to the endpoint bremsstrahlung energy. For the error rate testing in this study, the spectrum is modified by a 1 mm aluminum attenuator, which reduces the flux of low-energy X-rays incident onto the DUT. The electron fluences corresponding to monoenergetic 50 keV X-rays interacting with the active silicon region in the “forward” (scattering events in the active device overlayer materials, denoted BEOL) and “reverse” (scattering events in the device substrate) beam directions are shown on the right. 82
3.4 50 keV photo-electrons exiting the aluminum attenuator have insufficient energy to transport through the 3.5 cm air gap and back end of line (BEOL) materials to reach the active silicon. Only photo-electrons generated in the DUT itself can interact with the device material in the sensitive silicon region. 84
3.5 A 10 keV X-ray is normally incident on the simulated device structure of a 45 nm SRAM. It subsequently undergoes photoabsorption resulting in the generation of a energetic electron. The resulting electron then transports through the device material, depositing energy in excess of 9.3 keV within the sensitive volume of the SRAM. 85

3.6 ΔV_{OT} as a function of equilibrium dose for MOS capacitors irradiated with beam current and voltage of 1 mA and 50 kV, respectively. Devices were biased with 10 V on the gate during irradiation. The use of a 1 mm Al attenuator causes a increase in equilibrium dose required to achieve equivalent shifts in ΔV_{OT} by a factor of 17, indicating the nominal dose rate of 1.7 krad(SiO_2)/min is reduced to 100 rad(SiO_2)/min. 86
3.7 Experimental errors induced during irradiation with X-rays in an ARACOR 4100 X-ray irradiator. The bias sensitivity of critical charge in SRAMs provides strong evidence of energetic electron-induced upsets in modern SRAMs. 90
3.8 Experimental errors induced during irradiation with X-rays in an ARACOR 4100 X-ray irradiator. Results are for Test Chip B, errors are plotted as a function of distance from row 0, corresponding to V_{DD} lines, and row 128, corresponding to V_{SS} lines at a supply voltage of 0.35 V. Errors occur randomly within the SRAM cell and do not preferentially occur near supply voltage or ground rails. 91
3.9 SEU probability dependence on supply voltage for X-ray irradiation, compared to low-energy protons and muons in 28 nm SRAMs. Results show that under nominal bias conditions protons and muons are capable of inducing upsets in 28 nm SRAMs while this sensitivity is absent for energetic electrons generated during X-ray exposure. Under reduced bias conditions, X-ray SEUs exhibit a larger dependence on supply voltage than muons and protons in the 28 nm technology nodes. 93
3.10 SEU probability dependence on supply voltage for X-ray irradiation, compared to low-energy protons and muons in 45 nm SRAMs. Results show that under nominal bias conditions protons and muons are capable of inducing upsets in 45 nm SRAMs while this sensitivity is absent for energetic electrons generated during X-ray exposure. Under reduced bias conditions, X-ray SEUs exhibit a larger dependence on supply voltage than muons and protons in the 45 nm technology nodes. 95

4.1 MRED simulation results of the attenuated ARACOR spectrum, seen in Figure 3.3, normally incident on a 45 nm bulk SRAM structure. The vertical black lines represent the lower-limit estimates of critical charge for a 45 nm SRAM. The results provide supporting evidence suggesting that energetic electrons generated by incident X-rays are capable of depositing sufficient energy to exceed the estimated upset threshold. 99

4.2 Incident 10 keV electrons/δ-rays are shown scattering in a 50 nm cube of silicon. Event 4.2(a) shows a 2.1 keV energy deposition event that produces additional electrons/δ-rays in a chain of inelastic scattering events. Event 4.2(b) shows a 2.6 keV energy deposition event that produces several tertiary electrons/δ-rays in a series of inelastic scattering events. 101
4.3 Comparison of simulated versus experimental normalized cross-section for Test Chip D, a 45 nm bulk SRAM. 102
4.4 The differential flux spectrum of incident electrons is plotted using the AE-8 description of the electron environment, at geosynchronous orbit during solar maximum with 150 mils aluminum shielding. It is noted that 150 mils of aluminum is sufficient to shield the simulated SRAM from protons in this environment. 104
4.5 Differential electron flux for unshielded, 100 mils, 730 mils, and 870 mils of aluminum shielding in the Jovian and Europa tour phase of the Juno spacecraft mission to the Jupiter planetary system. 105
4.6 Differential proton flux for unshielded, 100 mils, 730 mils, and 870 mils of aluminum shielding in the Europa tour phase of the Juno spacecraft mission to the Jupiter planetary system. 106
4.7 MRED simulations performed on the 45 nm structure from Figure 4.1 using the AE-8 description of the electron environment, at geosynchronous orbit during solar maximum with 150 mils aluminum shielding. Simulation results show that the event rate of electrons is small for devices operated at nominal supply voltage. However, more sensitive devices will experience a significant increase in single electron events. These results suggest that operating SRAMs under reduced bias conditions will result in a dramatic increase in single electron events. . . 107
4.8 MRED simulations performed on the 45 nm structure from Figure 4.1 using the differential electron flux of Figure 4.5 for shielding thicknesses of 100, 730, and 870 mils of aluminum. Results show that shielding has some impact on the overall electron-induced SEU error rate in the Jovian and Europa environments as shown by the slight reduction in event rates for equivalent orbits. Devices operated in a low-power or quiescent mode are likely to experience an unacceptably large upset rate while in proximity to the Jupiter planetary system. 109
4.9 MRED simulations performed on the 45 nm structure from Figure 4.1 using the electron environment of Figure 4.5 and proton environment of Figure 4.6 for shielding thicknesses of 100, 730, and 870 mils of aluminum. Proton-induced SEU error rates are observed to be higher than electron-induced SEU error rates at nominal supply voltage. Electron-induced SEU error rates become higher than proton-induced error rates under reduced bias conditions. 110

4.10 Representation of a the energy deposition from δ-rays generated by a single 560 MeV N ion incident on a large silicon structure. Each box represents the energy deposited by δ-rays in a specific region. The magnitude of energy deposited at each location is represented as color intensity, where warmer colors are larger energy deposition events. . . 115
4.11 Simulation results show good agreement for energy deposited within a 50 nm cube by the Katz model (solid red line) and MRED for 25 MeV/u He. The lower edge of the box is the average energy, the upper edge of the box is the 90th percentile event, and the whisker is the largest energy deposition event. While the average energy within a 50 nm cube shows a strong dependence on the radial distance, MRED shows that large energy deposition events occur at radial distances greater than 10 μm. 116
4.12 Simulation results show good agreement for energy deposited within a 50 nm cube by the Katz model (solid red line) and MRED for 25 MeV/u Ne. The lower edge of the box is the average energy, the upper edge of the box is the 90th percentile event, and the whisker is the largest energy deposition event. Large energy deposition events are again shown to occur at radial distances larger than 10 μm. 117
4.13 Cumulative energy distribution as a function of radial distance for 15 MeV/u and 40 MeV/u Ne ions. Results show the frequency of δ-ray energy deposition events depend on LET and energy of the incident particle. 120

Chapter 1

Introduction

The ability to store and read information is critical for reliable system operations in modern electronics. Information is stored in dense arrays of devices and circuits whose purpose is to maintain mission critical instructions, record data, and return that information for further computation or analysis. Circuit- and device-level memories exist in the form of volatile and non-volatile elements. The static random access memory (SRAM) is a semiconductor memory that uses cross-coupled latching circuits to store information

SRAMs are renowned for fast read and write times, small areal density, exhibit a non-destructive read operation, and do not require periodic refreshing of data since information persists while the memory is powered. The SRAM represents a stable memory that has become an essential circuit-level cell because of its rapid read and write times, making it ideal high-performance reconfigurable logic as well as microprocessor and system level cache. Radiation sensitivity of circuit-level memory is an important consideration when evaluating reliability concerns of modern technology in a variety of hazardous environments including military, space, nuclear, and the terrestrial level. Single-event upset (SEU) is an example of the sensitivity of modern microelectronics to ionizing radiation. SEUs are defined as the erroneous change of state of a semiconductor memory, such as an SRAM, stemming from energy deposition by an ionizing particle that results in charge generation within a sensitive region of the microelectronic element.

In pursuit of performance and density goals, the semiconductor industry continues to scale complementary metal–oxide– semiconductor (CMOS) technologies to smaller

feature sizes with reduced operating voltages. Continuing decreases in device dimensions and operating voltage reduce the critical charge required to produce a SEU, affecting the reliability of modern technologies in space and terrestrial environments. Decreasing critical charge has led to the emergence of SEUs induced by lightly ionizing particles, such as low-energy protons and muons [1, 2]. Traditionally, the primary radiation effects caused by energetic electrons in the trapped radiation environments of Earth and Jupiter were considered to be total-ionizing dose (TID), displacement damage (DD), and spacecraft charging (or electrostatic discharge (ESD)) [3, 4]. However, there has been increasing interest in the spatial distribution of charge produced by lightly ionizing particles, including high-energy secondary electrons [5–11]. These secondary electrons, also called δ-rays, lose their kinetic energy through ionization, producing electron-hole (e-h) pairs that may cause SEUs. Attempts to quantify contributions from energetic electrons to the upset rate in memories fabricated in advanced technology nodes through simulation has obtained in conflicting conclusions [5–11]. Despite extensive simulation efforts [5–11], lack of experimental data has left the role of energetic electrons in the SEU response of modern SRAMs an open question.

In this dissertation, a low-energy X-ray source is used to generate energetic electrons to evaluate the susceptibility of CMOS SRAMs fabricated in the 28 nm and 45 nm technology nodes to electron-induced SEUs. Throughout this dissertation, "electron-induced SEUs" refer to events in which the initiating particle is a high-energy electron (δ-ray); the eventual upsets are produced by thermalized e-h pairs generated as the δ-rays lose their energy through ionization. The sequence of events in electron-induced SEUs is depicted in a series of image panels shown in Figure 1.1. The top left image of Figure 1.1 shows a particle strike on the sensitive node of an SRAM indicated by a lightning bolt striking the drain of the nMOSFET *M1*. The

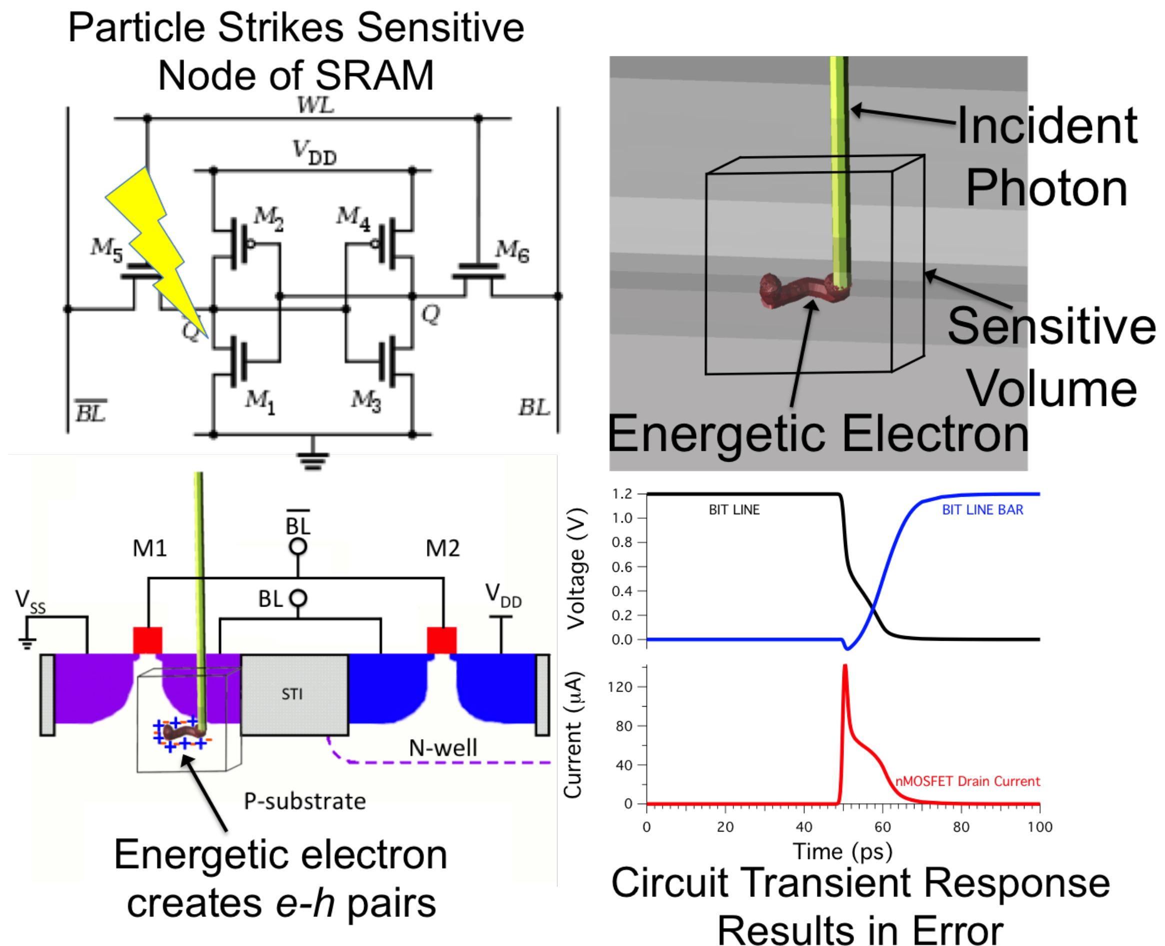

Figure 1.1 The sequence of events in electron-induced SEUs is depicted in a series of image panels. The top left image shows a particle strike on the sensitive node of an SRAM indicated by a lightning bolt striking the drain of the nMOSFET *M1*. The top right image shows the absorption of the incident particle, in this case a 10 keV X-ray, and the generation of an energetic photo-electron. This energetic electron undergoes multiple scattering events eventually thermalizing within the sensitive volume of the SRAM. The energy loss of the energetic electron results in the generation of electron-hole pairs that are subsequently collected, as seen in the bottom left panel. Finally, the device- and circuit-level response is shown in the bottom right, where the SRAM transient response on the BL and $\overline{BL}$ nodes latch an error into the memory, after [12].

top right image of Figure 1.1 shows the absorption of the incident particle, in this case a 10 keV X-ray, and the generation of an energetic photo-electron. This energetic electron undergoes multiple scattering events eventually thermalizing within the sensitive volume of the SRAM. The energy loss of the energetic electron results in the generation of electron-hole pairs that are subsequently collected, as seen in the bottom left of Figure 1.1. Finally, the device- and circuit-level response is shown in the bottom right, where the SRAM transient response on the BL and $\overline{BL}$ nodes latch an error into the memory. It is the energetic photo-electron shown in the top-right panel of Figure 1.1 that is responsible for initiating the error that is ultimately latched into memory and the reason this phenomenon is referred to as "electron-induced SEU".

Upsets are observed within 10% of nominal supply voltage for the 28 nm technology node. That these memory upsets are indeed electron-induced SEUs is supported by Monte Carlo radiation-transport simulations, which show that single energetic electrons deposit sufficient ionizing energy to generate charge in the sensitive volume of the device that is well in excess of estimated critical charge values. The relative importance of electron-induced SEUs is compared to other physical processes, such as direct ionization from low-energy protons [1, 13–15] and muon-induced upsets [2, 16] in determining error rates of selected SRAMs fabricated in 28 nm and 45 nm technology generations. The impact of electron-induced SEU on scaling of feature size and voltage in modern CMOS processes, ultra-low power applications, and error rates in the space radiation environment is discussed in detail.

The organization of this dissertation is as follows. Chapter 2 presents background material including a review of SRAM topology, operation, stability, discussion of relevant topics of radiation effects in SRAMs, a review of the space radiation environment, and a summary of past work on ionizing particle track structure. Chapter 3 presents the experimental setup and methods used in this work, show and discuss

experimental results of SEUs observed during X-ray irradiation of 28 nm and 45 nm bulk silicon SRAMs, and compare electron-induced SEUs to low-energy proton and muon data. Chapter 4 presents results of simulations supporting the X-ray investigations of Chapter 3 that show good agreement with experimental results. Single-event upset error rates are estimated using simulation techniques. The consequences and importance of these results are discussed for the space radiation environment. Analysis of the contribution of δ-rays generated in heavy-ion irradiation to single- and multiple-bit upset rates is also discussed. Finally, Chapter 5 presents conclusions and discusses the significance of these results for modern technology nodes.

Chapter 2

Background

Reliable operation of electronic memories is a primary concern for the semiconductor industry. Electronic components used in space applications experience harsh environments and hazards when compared to applications at the terrestrial level, including additional risk of fault or failures in electronics due to the presence of ionizing radiation. The interaction of ionizing radiation with microelectronics in the space environment and at the terrestrial level has been observed to cause both temporary and permanent damage to semiconductor devices, circuits, and systems. Remote satellites and planetary exploration probes, such as the Juno spacecraft, whose mission is to explore the Jovian environment and moons, cost in excess of 1.1 billion USD [17], or in the case of the James Webb Space Telescope, 8.7 billion USD [18]. The construction and operation of such equipment necessitates the use of cost-effective electronics, placing a premium on reliability while balancing the expense of implementing and ensuring the quality of flight components.

This chapter presents background information essential for the discussions and topics presented in Chapters 3 and 4. Section 2.1 covers basic interaction mechanisms of heavy-ion, electron, and photon transport processes. Section 2.2 presents a review of the topology, operation, and stability of the six-transistor (6-T) SRAM. Section 2.3 discusses the broad topic of ionizing radiation effects in SRAMs. These topics are further broken down into single-event effects (SEEs), TID effects, and transient radiation effects. Subcategories include SEUs, the observation of SEUs due to low-energy protons and muons, SRAM cell imprinting, and the impact of transient radiation environments on SRAMs. Section 2.4 presents information related to so-

lar particle events, galactic cosmic rays, and trapped particles in the space radiation environment. Finally, Section 2.5, covers heavy-ion track structure and presents an overview of recent studies regarding the effects of δ-rays on microelectronics.

A large segment of Section 2.3 focuses on SEUs, which are the erroneous change of state of an electronic memory due to ionizing radiation depositing energy within a sensitive region of the circuit/device element. The change of information state is due to energy deposited within a sensitive region of an SRAM cell. The collection of generated e-h pairs within the sensitive region then results in the SRAM transitioning from one state to the complement, producing an erroneous information state. In the context of an SRAM cell this corresponds to the change in state of the memory, either from a *0* to *1* state or *1* to a *0* state. For applications in space, SEUs have been attributed to particles emanating from the galactic cosmic ray (GCR) environment, energetic protons and alpha particles, which can be found in the trapped radiation environments near Earth and the Jovian environment, and particles eminating from the sun in solar particle events. For satellites ranging from geostationary to low Earth orbits, the primary radiation concerns are solar particle events and particles trapped by the Earth's magnetic field. Interplanetary probes are exposed to the solar particle environment, the GCR environment, and the radiation environment specific to the mission destination.

The large financial expense associated with space applications introduces additional stringent reliability requirements due to the high cost of mission failure. Higher reliability requirements in the space radiation environment have often necessitated the use of electronic components that are "radiation-hardened" or at best "radiation-tolerant" devices that have increased resistance to the effects of radiation. Commercial-off-the-shelf parts are appealing to designers as a venue to reduce cost of production and power consumption, however, these trade-offs often come with an

increase sensitivity to ionizing radiation and mission risk.

In the terrestrial environment, commercial enterprise depends on cloud computing, routers, and servers for computation, transactions, and communications. Faults in these types of systems represent unacceptable losses of time, financial transactions, and connectivity. Traditionally, SEUs in the terrestrial environment have been dominated by neutrons and alpha particles emitted by packaging contaminants [2, 19–21]. However, recent studies have shown that modern SRAMs fabricated in sub-65 nm technology nodes are susceptible to direct ionization effects from lightly ionizing muons [2, 16, 21], by far the most abundant particle species in the terrestrial radiation environment [2, 22, 23].

The particle spectrum present in the space and terrestrial radiation environment have different characteristics and therefore introduce reliability concerns unique to the application. Understanding the threat and source of reliability concerns is essential for effective mitigation strategies and maintaining stable operation of critical electronic systems.

2.1 Basic Interaction Mechanisms

Radiation interacts with semiconductor device materials through many physical processes. Those interactions, in turn, determine the energy deposition profile in an ionizing particle event. The magnitude and spatial distribution of energy deposited in a single ionizing particle event determines the device and circuit level response.

The average energy lost per unit path length (dE/dx) by an incident ionizing particle in a target medium can be described by the stopping power metric, or mass stopping power when normalized to the density of the target medium, and is represented in units of MeV-cm^2/mg. Stopping power is also referred to as linear energy transfer (LET). Stopping power can further be broken down into electronic and

nuclear stopping power components. The electronic stopping power component corresponds to energy lost by the incident particle to the electron gas of the medium. The nuclear stopping power component involves any elastic ion–nucleus interactions, also known as Coulomb scattering. The total stopping power can be described as the superposition of the electronic and nuclear stopping power components.

In this section, the transport of ions, electrons, and photons are discussed. While nuclear processes are significant and the dominate interaction mechanism for a wide variety of particles and energies, the focus of these discussions revolve around electronic energy loss mechanisms.

2.1.1 Ion Transport

Energetic particles, in the form of solar protons, trapped protons, and heavier elements from the GCR environment, are highly ionizing and frequently interact with semiconductor device materials in the space radiation environment. These particles interact with the electron gas of the target material through the electromagnetic force. Interactions result in energy loss by the incident particle and ionization of the target material, exciting some valence band electrons into the material conduction band. In the presence of an electric field, these electrons can be collected and contribute to an ion-induced transient current.

The mean energy loss for an incident particle, $\overline{S}$ or LET, is described by the modified Bethe-Bloch equation [24]

$$-\frac{dE}{dx} = \frac{4\pi}{m_e c^2}\frac{N_A Z\rho}{A}\frac{z_{eff}^2}{\beta^2}\left(\frac{e^2}{4\pi\epsilon_0}\right)^2 L(v) \tag{2.1}$$

$$L(v) = \frac{1}{2}\ln\left(\frac{2m_e\gamma^2c^2\beta^2 W_{max}}{I^2}\right) - 2\beta^2 - \frac{\delta(\beta\gamma)}{2} - \frac{C(I,\beta\gamma)}{Z} \tag{2.2}$$

where e is elementary charge, z_{eff} is the effective charge state of the incident particle, β is relative velocity, $\frac{v}{c}$, where v is the incident particle velocity, m_e is the electron

mass, c is the speed of light, γ is the Lorentz factor, $(1-\beta^2)^{-1/2}$, ϵ_0 is the permittivity of free space, I is the mean ionization energy, W_{max} is the maximum energy transferred to an electron, N_A is the Avogadro number, ρ, Z, and A are the target material density, proton number, and molar mass constant, respectively. The modified Bethe-Bloch equation is valid for heavy charged particles less than 100 GeV where $\beta \gg \frac{z}{137}$ [24]. Additional corrections to the Bethe-Bloch equation correct less than 1% error for low-energy charged particles [24].

Equation 2.1 shows that the LET of an incident particle depends on many parameters of the incident particle and target material. Correction terms are necessary to accurately represent the stopping power of ions at low energy. The $\delta(\beta\gamma)$ term corresponds to density corrections necessary for relativistic particles with kinetic energy greater than the incident particle rest mass [24]. The $C(I, \beta\gamma)$ terms corresponds to shell corrections for non-relativistic protons, accounting for detailed interactions between bound state electrons and incident protons [24].

From Equation 2.1 the LET of an incident particle in a target material depends on the effective charge state and relative velocity. It can be concluded that for similar velocity ($\beta = \frac{v}{c}$), singly-charged particles (i.e. muons, pions, protons, electrons, and positrons) have approximately equivalent LETs. It is, however, necessary for additional corrections to be made for singly-charge particles and their corresponding antiparticles due to the Barkas effect, the most notable example of this is positrons and electrons [25].

Stopping power curves in silicon are shown as a function of incident ion energy per unit mass in Figure 2.1 for protons, alpha particles, carbon, oxygen, and iron. The stopping power curves shown in Figure 2.1 were calculated using the SRIM/TRIM radiation transport codes [24]. The maximum value of stopping power for a given particle species is known as the Bragg peak. The stopping power curves shown in

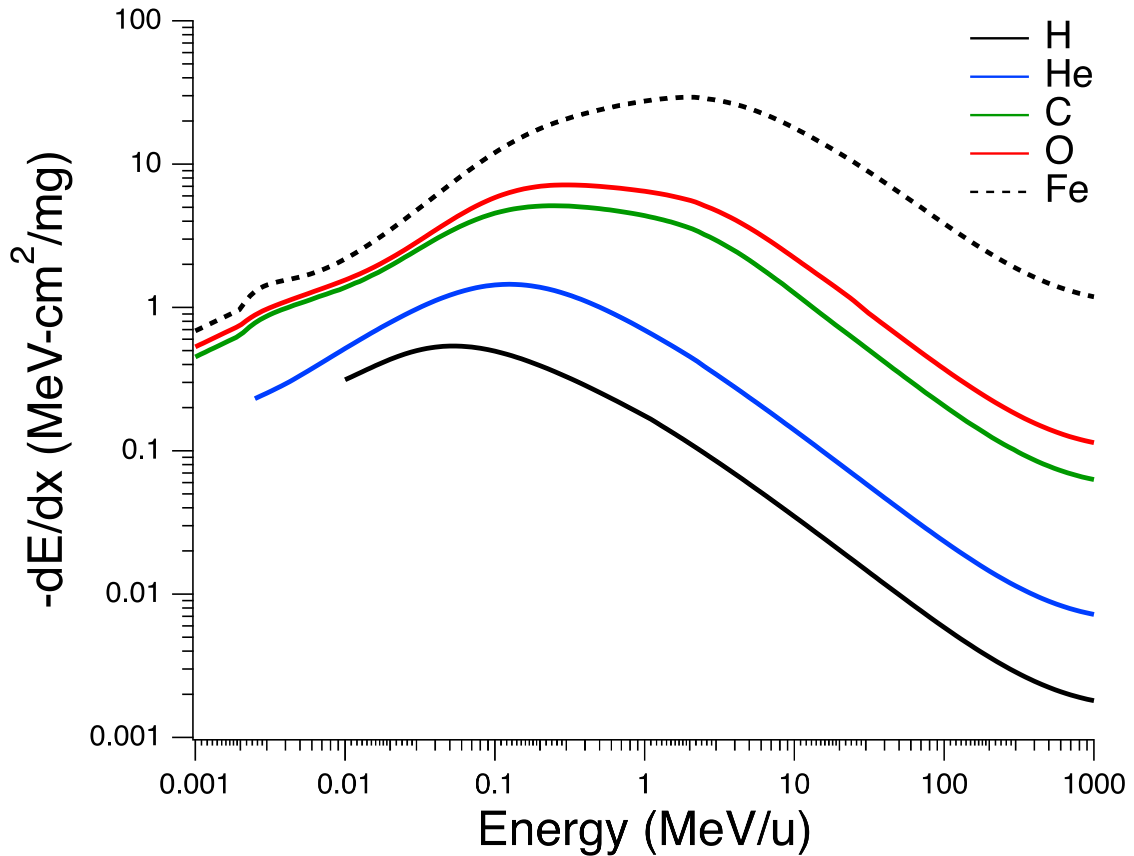

Figure 2.1 Stopping power in silicon is plotted as a function of energy per unit mass (MeV/u) for protons, alpha particles, carbon, oxygen, and iron. Stopping power was calculated using the SRIM/TRIM codes [24].

Figure 2.1 are approximately maximum when the velocity of the incident particle energy approaches the Fermi velocity, the velocity corresponding to electrons with energy equal to the Fermi energy, E_f, of the target material. Furthermore, equivalent stopping power can be obtained for a given ion species with different incident energies. This indicates that identical particle species with different energy on average lose the same amount of energy for equivalent penetration into the target material. Since the particle energies available at terrestrial based accelerators cannot replicate the high energy spectra of particles in the space radiation environment this principle forms the basis of most ground-based parts qualifcation testing for space applications.

The energy lost to the target material through direct ionization generates *e*-*h* pairs in semiconductor materials. The average energy to create an *e*-*h* pair in silicon is 3.6 eV [26–28]. In this sense, one can equate the energy lost by ionizing particles with the generation of charge in semiconductor devices.

The average range of an energetic particle in a target material as its trajectory terminates can be accurately described by the continuous slowing down approximation (CSDA). The CSDA range assumes that particles transport in a straight line trajectory and variations in energy loss are negligible compared to the total stopping power [29]. It is difficult to define a CSDA range for particles with erratic trajectories due to interactions where large energy loss and large angle deflections occur, this is a valid consideration for energetic electrons with energy less than 10 keV. The CSDA range is obtained by integrating the reciprocal of the total stopping power from the Bethe-Bloch equation, Equation 2.1, with respect to the incident ion energy.

$$R(E) = \int_{E_{abs}}^{E} \frac{dE'}{S(E')} \tag{2.3}$$

Equation 2.3 describes the CSDA range calculation, where $R(E)$ is the range of a particle with energy E, $S(E)$ is the stopping power as described by Equation 2.1 and E_{abs} is the energy at which the particle is assumed to be absorbed (i.e. at rest) within the target material. It should be noted that Equation 2.3 is only valid for the energy range and conditions where the modified Bethe–Bloch equation is also valid.

The resulting CSDA range approximations in silicon as a function of incident ion energy per unit mass for protons, alpha particles, carbon, oxygen, and iron ions are shown in Fig 2.2. The CSDA range curves shown in Figure 2.2 were calculated using the SRIM/TRIM radiation transport codes [24].

The range of many of these ion species at energies corresponding to the radiation belts around Earth and Jupiter, GCR, and solar wind environments is much greater

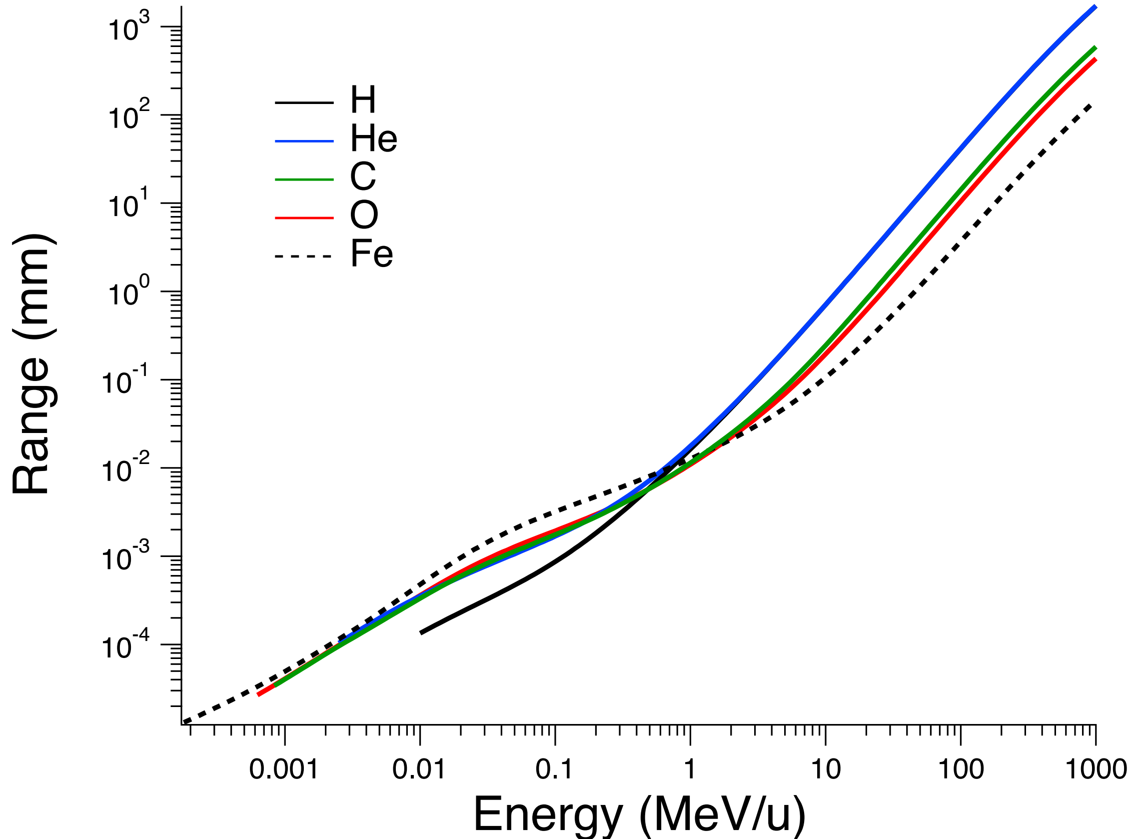

Figure 2.2 CSDA range in silicon as a function of incident ion energy per unit mass for protons, alphas, carbon, oxygen, and iron ions.

than that of the spacing, pitch, and thicknesses of modern semiconductor device structures. This indicates that single ionizing particle radiation events that occur at large angle of incidence can interact with and perturb multiple devices and circuits.

In 1988, Stapor *et al.* illustrated the potential for differences in the response of microelectronics for two incident ions with similar LET due to differences in the resulting energy deposition profiles [30]. These conclusions were supported by analyzing the transient response of devices to ions having the same LET but different energies in [31]. Similar conclusions were reached by Weller and Kobayashi in works published in 2003 and 2004, respectively, which illustrated the importance of energy deposition

profiles for proton and alphas in determining the device response to ionizing radiation [5, 32].

The LET metric has been robust and effective for understanding and modeling the SEU response of SRAMs for many years and continues to serve as the basis for the majority of SEE analysis [33–35]. The application of LET to SEU/SEE analysis relies on the assumption that knowledge about the average energy deposition event is sufficient to predict the circuit response to an ionizing particle event. In recent years however, additional physical mechanisms have been required to explain SEU cross sections where LET alone has been insufficient [36–40]. With the observation of low-energy proton- and muon-induced SEUs the SRAMs fabricated in sub-65 nm technology nodes show trends of increased device SEU sensitivity to ionizing radiation that does not appear to be slowing. The sensitivity of SRAMs to lightly ionizing particles and the concept of critical charge is be discussed in Section 2.3.

2.1.2 Electron Transport

Electrons are negatively charged elementary subatomic particles with a mass of 0.511 MeV/c^2. By comparison, the proton mass is 938.23 MeV/c^2 and the muon mass is 105.7 MeV/c^2, making the electron approximately 1836 and 206 times lighter than other common singly-charged particles. Energetic electrons interact with a target material predominantly through electromagnetic processes. Two energy loss mechanisms are important for electrons interacting with a target medium, inelastic scattering with atomic electrons and elastic scattering with target nuclei.

Collisions are the dominant energy loss mechanism for low and intermediate electron energies, where the incident electron interacts with atomic electrons of the target material. These are interactions that produce *e*-*h* pairs, ionization, or result in the ejection of additional energetic electrons from the band structure of the material. The

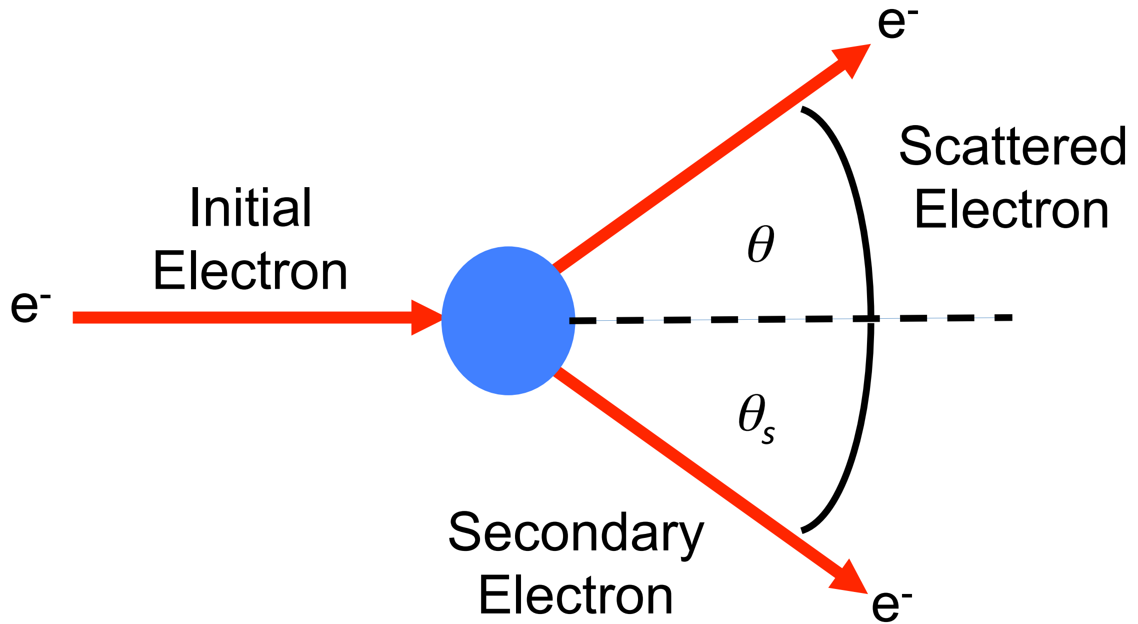

Figure 2.3 Scattering of an incident electron resulting in generation of a secondary electron

initial formalism of inelastic scattering with single atoms or molecules was made by Bethe in [41, 42] by considering a plane-wave using the Born approximation. This theory was later extended by Fano for inelastic scattering of electrons in condensed matter [43]. The impact on the incident electron can be accurately described by the energy loss, W, and the polar and azimuthal scattering angles, ϕ and θ.

A cartoon of electron scattering can be seen in Figure 2.3. The incident energetic electron interacts with an atomic system resulting in energy transfer, W. Most interactions with atomic electrons result in the generation of e-h pairs in semiconductors. If the energy loss by the incident electron is in excess of the shell binding energy, E_b, the interaction results in the emission of an energetic electron that is free of the material band structure, also called a δ-ray. The energy of the generated secondary electron is equal to the difference between the energy lost by the incicident electron

and the binding energy of its original shell, $W - E_b$. The relaxation of the excited atomic state, the vacancy of the ith shell state, involves the emission of fluorescent radiation in the form of soft X-rays with energy equal to the ith shell binding energy or the emission of Auger electrons. The equal masses involved in inelastic scattering, which are electron–electron interactions, result in angular deflections of the incident electron. Angular deflections of energetic electrons transporting through material are important parameters that make determining the range of low energy electrons, lower than a few tens of keV, difficult.

The second important interaction mechanism for electrons in this work is the elastic scattering of incident electrons with atomic nuclei. Here the elastic scattering event is defined to be an interaction between an energetic electron and a target nuclei where the initial and final quantum states of the target atom are the same, usually this is the ground state. The elastic scattering with target nuclei result in large angle deflections of incident energetic electrons.

A cartoon of an elastic scattering event is shown on the left hand side of Figure 2.3. For elastic scattering events, there is a small transfer of energy from the incident electron to the target nuclei, potentially resulting in the emission of a recoil atom. Because of the large mass of the target nuclei relative to the electron mass, the average energy lost by an incident electron in elastic scattering events is a *small* fraction of its initial energy. For electrons with energy of 30 keV, the energy lost in elastic scattering events is on the order of a few meV [44]. Scattering events, of the elastic and inelastic variety, both contribute to large angle deflections of energetic electrons. These large angle deflections make approximating the range of electrons in matter through methods like the CSDA range difficult at low energies (less than a few 10s of keV).

Because of their small mass, electrons undergo Bremsstrahlung and Cerenkov

radiative processes. The total stopping power of electrons is represented as the superposition of the collision and radiative stopping power processes.

$$-\left(\frac{dE}{dx}\right)_{total} = S_{coll}(E) + S_{rad}(E) \tag{2.4}$$

In Equation 2.4, $S_{coll}(E)$ and $S_{rad}(E)$ are the stopping power contributions from collisions and radiative processes respectively. The total stopping power of electrons in silicon is plotted as a function of energy on the left axis in Figure 2.4. Radiative energy loss processes do not occur for heavier particles (at least until *extremely* high energies) and are important for understanding electron transport. Generation of Bremstrahhlung and other radiative processes and have consequences for electrons with energies in excess of 10 MeV in silicon. Radiative energy loss processes are an important considerations when evaluating the consequences of electrons in the space-radiation environment. This dissertation considers the contribution of electron scattering interactions between the incident electron and the target material. With appropriate modifications to the Bethe-Bloch formula of Equation 2.2 it can be shown that the maximum single electron–electron scattering event energy loss is one half of the initial electron energy, $E_i/2$ [44–46]. Electrons are therefore capable of depositing large amounts of energy within small spatial regions.

The range of energetic electrons in a target material can be approximated using Equation 2.3. The approximate CSDA range of electrons is shown in Figure 2.4. Below energies of approximately 1 MeV, electrons follow a similar trend as the heavy ions shown in Figure 2.2, where the incident particle range increases with increasing energy. Electrons exhibit a decrease in range with increasing energy above energies of 10 MeV due to the radiative energy loss processes (Bremsstrahlung and Cerenkov).

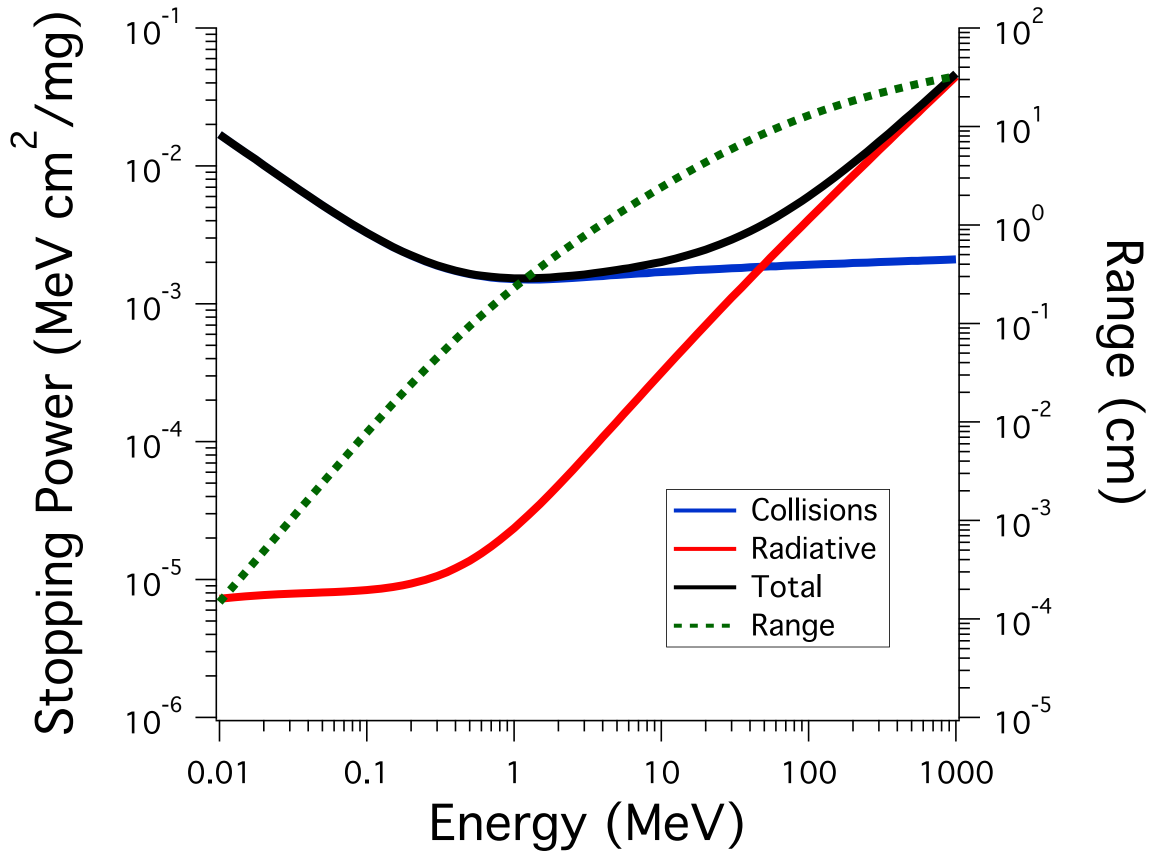

Figure 2.4 Total stopping power, $-\left(\frac{dE}{dx}\right)_{total}$, and CSDA range are plotted as a function of energy in silicon. Collisions dominate energy loss at electron energies less than 1 MeV. Radiative processes are more prevalent at higher electron energies.

2.1.3 Photon Transport

Photons are elementary particles, the quantum of light, and the force carrier of the electronmagnetic force. Three physical processes dominate energy loss by incident photons in matter, the photoelectric effect, Compton scattering, and pair production. While pair production is an important interaction mechanism, this discussion focuses on the photoelectric and Compton scattering effects, which are most relevant to the work presented in Chapters 3 and 4. Figure 2.5 shows the energy dependence of the three dominant physical processes for photons incident in material.

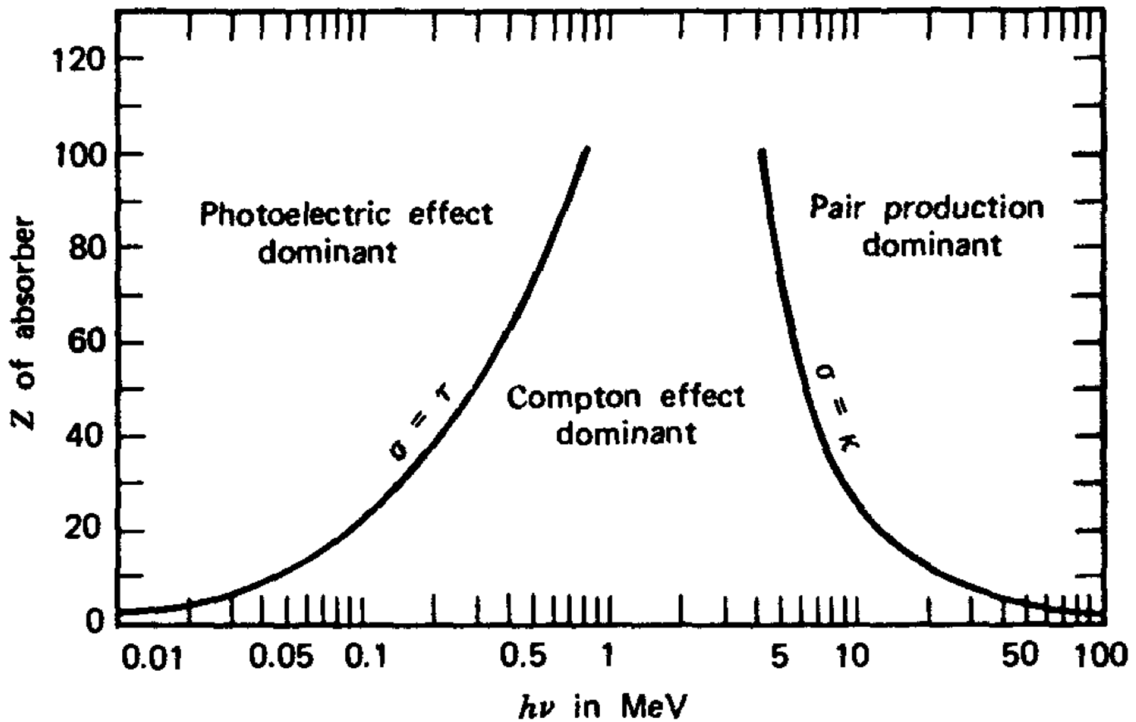

Figure 2.5 The energy dependence of the three major types of photon interactions are shown. The lines shows the values of material Z and photon energy $\hbar\omega$ for which the two neighboring effects are approximately equal [47].

In silicon, the dominant interaction of photons with energy less than 70 keV is the photoelectric effect. The photoelectric effect is a point interaction where the incident photon is absorbed by a target atom, leaving the atom in an excited state. Figure 2.6 shows a cartoon description of a photoabsorption event from [48]. An energetic photo-electron is ejected from the material band structure as a result of the excited atomic state. Subsequently, an X-ray is emitted with energy equal to the binding energy, E_b, of the generated photo-electron due to the relaxation of an electron from an L or M–shell into the lower energy state. Generated photo-electrons are emitted omnidirectionally from a tightly bound state, such as the K–shell, assuming the incident photon has energy greater than the binding energy of the K–shell. The

energy transferred to the photo-electron can be described as

$$E_{e^-} = \hbar\omega - E_b \tag{2.5}$$

where $\hbar\omega$ is the energy of the photon and E_b is the binding energy of the photo-electron in its initial shell. For high energetic photons (where $\hbar\omega \gg E_b$) most of the absorbed photon energy is transferred to the photo-electron.

Photons with energy in the range of 70 keV to 12 MeV interact primarily through the Compton scattering process in silicon. The Compton effect involves the incoherent scattering of a photon by a bound electron. The scattering event results in energy loss by the incident photon, corresponding to a reduction in frequency, and the generation of a *recoil* electron. A diagram of a Compton scattering event is shown in Figure 2.7. Since the collision must obey both conservation of energy and momentum it can be shown that the transfer of energy from the photon can be described by

$$E_e = \hbar\omega \frac{\frac{\hbar\omega}{m_e c^2}(1 - \cos\theta)}{1 + \frac{\hbar\omega}{m_e c^2}(1 - \cos\theta)} \tag{2.6}$$

where $\hbar\omega$ is the energy of the incident photon, $m_e c^2$ is the electron rest energy, and θ is the scattering angle of the photon as seen in Figure 2.7.

Equation 2.6 shows thats for small scattering angles (where $\theta \approx 0$) little energy is transferred to the generated recoil electron. The maximum energy transfer occurs when the incident photon is back-scattered (where $\theta \approx \pi$) and the recoil electron has initial momentum along the incident photons original trajectory. The initial energy of all recoil electrons generated in Compton scattering events fall within the Compton continuum, an energy range bounded by the minimum and maximum energy transferred in a scattering event.

The total attenuation cross-section, μ, can be expressed as the superposition of the attenuation cross-section for each physical process shown in Figure 2.5. The

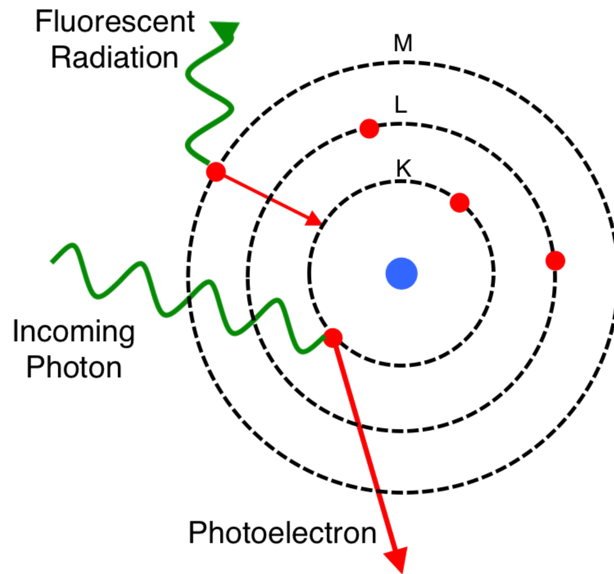

(a)

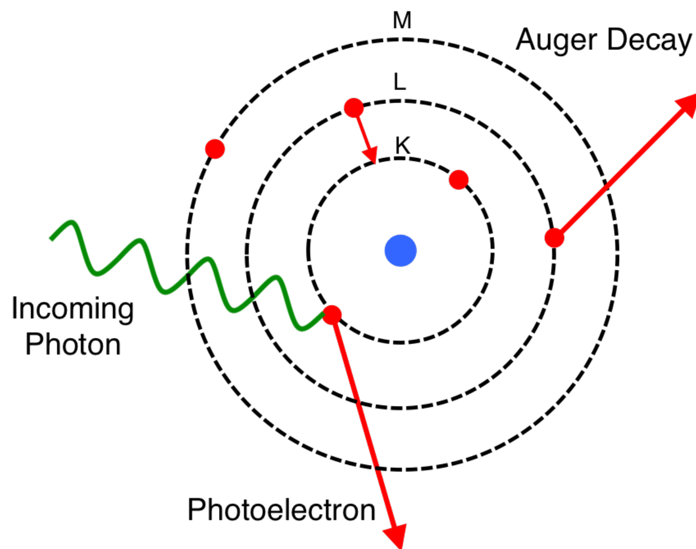

(b)

Figure 2.6 Absorption of an incident photon with energy $\hbar\omega$ resulting in the generation of an energetic photo-electron. Relaxation occurs through the emission of (a) fluorescent radiation or (b) Auger processes that result emission of a low energy electron or electrons.

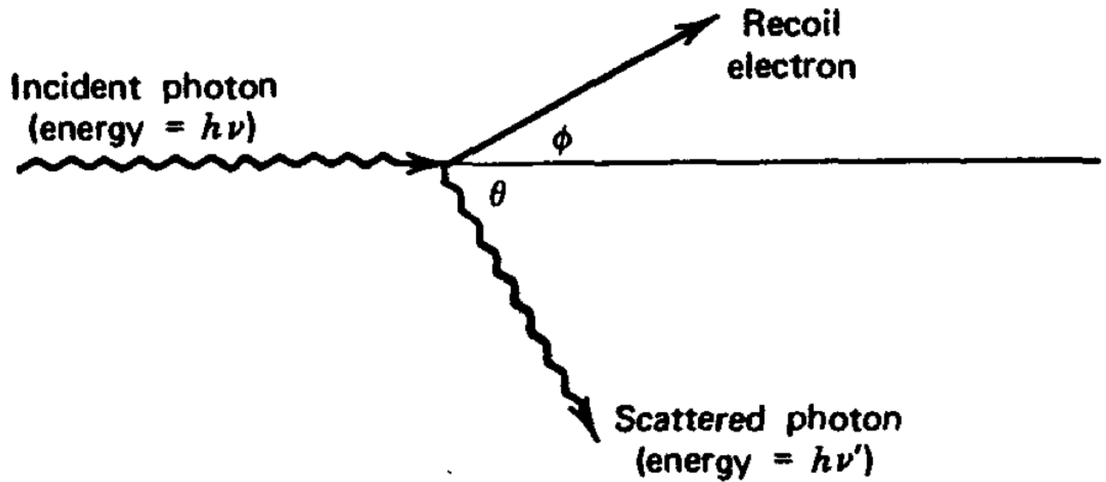

Figure 2.7 Diagram of a Compton scattering event between an incident photon with energy $\hbar\omega$ and an electron.

expression for total attenuation cross-section can be expressed as

$$\mu = \tau + \sigma + \kappa \tag{2.7}$$

where τ, σ, and κ are the photoelectric, Compton, and pair production cross-sections, respectively. The total attenuation cross section, μ, (in units of cm^2/g) versus incident photon energy in silicon is shown in Figure 2.8. The discontinuity seen at 1.839 keV corresponds to the silicon K–shell edge, this corresponds to the minimum energy required to emit an electron from the K–shell [49]. For incident photons with energy less than 1.839 keV, interactions involve the emission of photo-electrons from the L– or M–shells. The absorption edge corresponding to the L_1, L_2, and L_3-shells in silicon occur at 149.7, 99.8, and 99.2 eV, respectively.

The attenuation of energetic photons transporting through material can be calculated using the Beer–Lambert law [50], which is given as

$$N = N_0(E)e^{-(\mu(E)/\rho)(\rho x)} \tag{2.8}$$

where $N_0(E)$ is the initial number of photons with energy E, $\mu(E)/\rho$ is the energy-

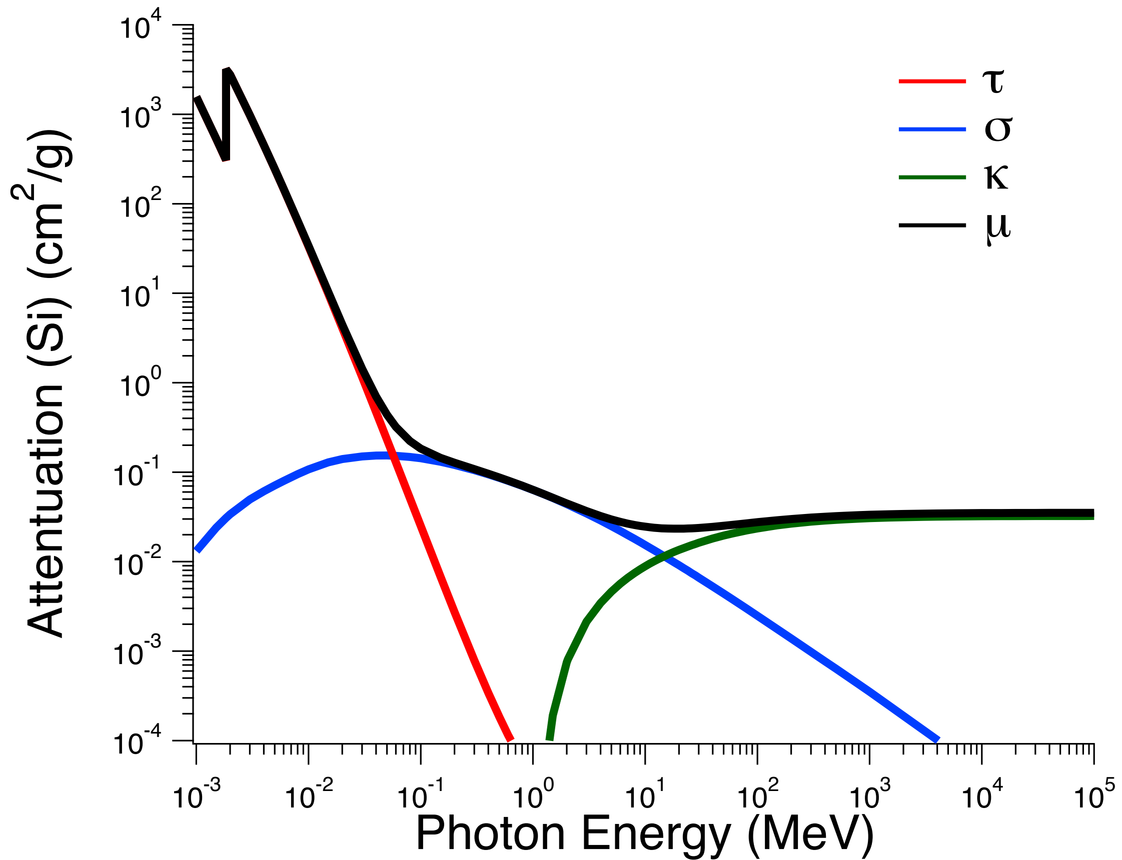

Figure 2.8 The attenuation cross-section, μ, versus incident photon energy in silicon.

dependent mass attenuation coefficient (obtained from Figure 2.8), and ρx is the mass thickness of the target material. Equation 2.8 provides a straight-forward method for calculating the attenuation of photons and can be used to determine the energy absorbed within a specific range of the target material.

2.2 Basic SRAM Topology and Operation

As CMOS feature sizes have decreased, a corresponding reduction in areal density of individual memory cells has lowered the cost per bit. This has enabled access to low-cost, high-speed memory for many applications. These attributes have made SRAMs

and DRAMs ideal for use in microprocessor cache memory, general-use registers, FPGAs, and high-performance applications.

While SRAM implementations can be expensive, in terms of area, they have higher speed read and write speed, do not require the periodic refreshing of data, exhibit a non-destructive read operation, and have lower power consumption than conventional dynamic random access memory (DRAM). Since an SRAM cell takes up more area than DRAM cells in the same technology node, these benefits come at the expense of increased area and cost. Both SRAM and DRAM are in a class of semiconductor memories known as volatile memories because data persists while the memory is powered. Basic SRAM implementations offer significant advantages over DRAM in terms of power consumption because they do not require the refreshing of data while powered. SRAMs are ideal where bandwidth, power, or both are a primary design consideration.

The basic topology of a standard six-transistor (6T) SRAM can be seen in Figure 2.9. While other SRAM implementations are possible, including non-volatile topologies, this dissertation only considers the standard 6T-SRAM cell. The basic SRAM cell stores information on two cross-coupled inverters, consisting of four transistors (M1–M4) that form a basic latch, enabling stable states of either *0* or *1*. Two additional access transistors (M5 and M6) allow access operations to the SRAM cell.

An SRAM cell has three standard modes of operation: write, read, and standby. A write operation occurs by applying a voltage to the bit line and its complement (BL and $\overline{BL}$) and asserting the word line. The voltage applied to the bit lines should have a large potential difference such that the state is quickly reinforced by the two inverters. A potential difference close to the supply voltage (V_{DD}) is quite common in standard technology implementations. A read operation occurs when the bit lines are left floating while the word line is asserted. Using peripheral circuitry (not shown),

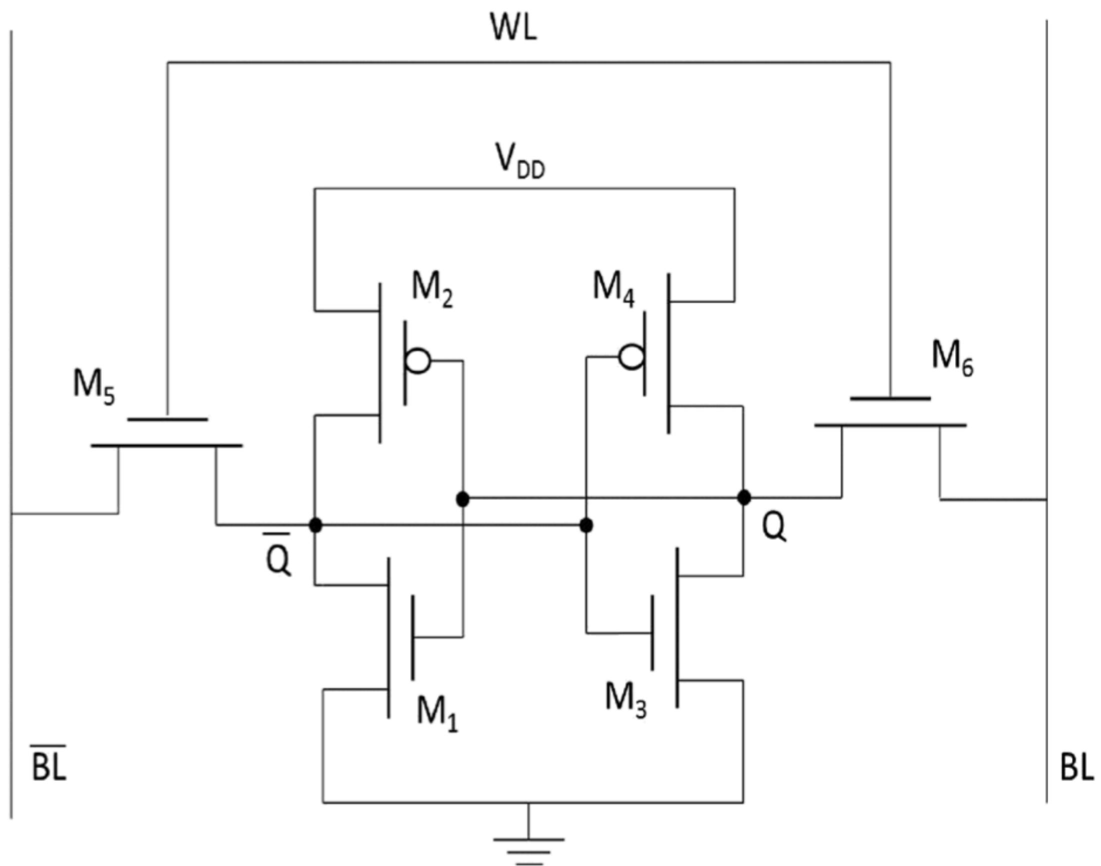

Figure 2.9 Basic SRAM circuit topology consists of two cross-coupled inverters and two access transistors.

a high-speed sense amplifier compares the voltage difference between the bit line and its complement, outputs the state of the cell to subsequent buffers, and is then passed to the output bus. Standby mode occurs when the word line is left floating, during which time the access transistors are "off" and the inverters continually reinforce the present state of the SRAM cell. Standby mode is the "idle state" of an SRAM cell and results in the lowest power consumption of all standard SRAM operating modes.

Design constraints often place restrictions on device operating frequency and power, forcing designers to vary the supply voltage as a means of meeting design specifications. A common practice to reduce power consumption while operating in

standby mode is to lower the supply voltage to the SRAM below the nominal supply voltage. This is a method known as dynamic voltage, frequency scaling at the systems level and is used to reduce power consumption when operating frequency is a secondary priority [51, 52]. The trade-off is made in applications where low-power is a primary operating parameter, such as medical implant devices, mobile communications, and mobile computing. For these applications, SRAMs are designed to remain stable and completely functional at 70–80% of the nominal supply voltage while maintaining valid information. While both bit lines are not required for proper SRAM cell operation, utilizing both the bit line and its complement increases the circuits noise margin and results in increased read and write speed.

Figure 2.10 shows the transfer characteristics, also known as butterfly curves, for a functional 22 nm SOI SRAM from [53]. The transfer characteristics represent the input/output states of the two cross-coupled inverters that comprise an SRAM cell. Here V_{in} is arbitrarily chosen to be the data state of Q in Figure 2.9 and V_{out} represents the output value $\overline{Q}$. When V_{in} is high, the transistors M_1 and M_2 are in the off and on states, respectively, and the corresponding value of V_{out} is low. The value of V_{out} is the input state of the inverter comprised of transistors M_3 and M_4. When V_{out} is low, transistors M_3 and M_4 are in the on and off states, respectively, which reinforce a high state of V_{in}. By sweeping V_{in} from high to low the transistors M_1 and M_2 change to the on/off configuration, sending V_{out} high which in turn forces the transistors M_3 and M_4 into the off/on configuration.

The stability of an SRAM cell is generally described in terms of the static noise margin (SNM), which is the DC noise an SRAM cell can tolerate while maintaining its intended state. The SNM of an SRAM cell is the side-length, given in millivolts, of the largest inscribed square that fits between the V_{in}/V_{out} transfer characteristics of Figure 2.10. Exceeding the SNM for an SRAM cell results in a change of information

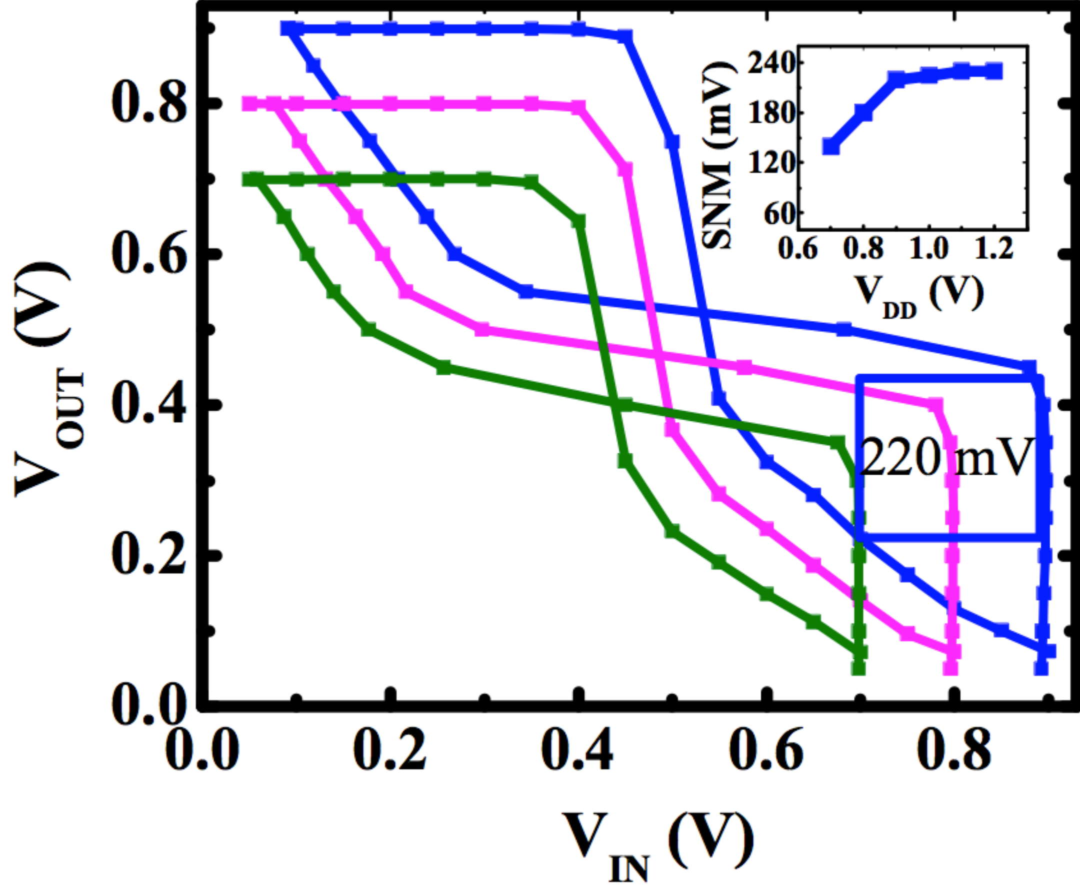

Figure 2.10 Butterfly curves for 0.1 μm^2 6T-SRAM cell showing SNM of 220 mV, 180 mV and 148 mV at V_{dd}=0.9, 0.8 and 0.7 V respectively [53].

state. Three sets of transfer characteristics are shown in Figure 2.10, corresponding to supply voltages of 0.9 V (blue curves), 0.8 V (pink curves), and 0.7 V (green curves). Figure 2.10 shows the SNM of an SRAM cell depends on the supply voltage, with lower V_{DD} corresponding to a smaller SNM. Similarly, the switching voltage, the input voltage where the state of the SRAM cell changes from a *1* to *0*, or vice versa, also depends on the supply voltage. The decrease in switching voltage and SNM under reduced supply voltage conditions increases the sensitivity of SRAM cells to errors from dynamic disturbances caused by ionizing radiation, crosstalk, supply voltage ripple, and thermal noise.

2.3 Radiation Effects on SRAMs

This section discusses the effects of radiation on SRAMs, much of it focused on the concept of SEUs with an emphasis on understanding the circuit-level response. The concept of critical charge is defined for the purpose of understanding the methods and analysis in Chapters 3 and 4. Recent studies describing the observation of low-energy proton- and muon-induced upsets and the impact of those results for microelectronics is discussed, emphasizing the trend towards increased sensitivity in modern devices. The effects of TID on SRAMs is introduced with the primary example being the "memory pattern imprinting" effect. Relevant issues related to transient radiation environments, so-called dose-rate effects, is also discussed.

2.3.1 Single-Event Upset in SRAMs

Energetic particles passing through material lose energy through electronic and nuclear processes as discussed in Sections 2.1.1 and 2.1.2. The electronic component consists of energy loss due to interaction with valence band electrons in the target material. Energy loss by the incident ion results in generation of mobile carriers in the conduction band and valence band, known as *e*-*h* pairs. Generated *e*-*h* pairs are collected through the drift carrier transport process, resulting in a transient on affected semiconductor junctions. Carriers generated in field free regions either recombine or diffuse to nearby regions where they are collected by electric fields, contributing to transients in nearby semiconductor nodes.

The physics of radiation-induced charge collection in semiconductor devices is a complicated topic and has been well-studied and reviewed in [54–65]. Collection of *e*-*h* pairs due to the presence of electric fields, known as drift current, diffusion of carriers in high-level injection regions into nearby junctions, and modulation of local

potentials due to the resulting transients all play significant roles in the response of semicondcutor devices to single ionizing particle events. By their nature, ionizing particle events generate dense regions of charge in the spatial locations where they interact making it difficult to represent the device and circuit response without the aid of computer tools, such as TCAD [57, 66, 67] and SPICE [67–69].

The amount of charge generated by the passage of a incident ion through a sensitive region of a semiconductor memory is related to the average energy required to generate a single *e*-*h* pair; in silicon this energy is 3.6 eV. In this sense, the energy lost by an incident particle is correlated with the amount of charge generated within the semiconductor device material. The SEU cross-section is an effective area defining the probability of an upset occurring. The cross-section represents a region where ionizing particles that interact with the target material may perturb circuit-level operation and potentially cause an error in memory. Upset cross-sections are represented by the symbol σ and given in units of cm^2/bit or cm^2/Mbit. SEU cross-sections have typically been analyzed as a function of incident ion LET based on the assumption that knowledge of the average interaction is sufficient to predict the event response, and subsequently, the error rate in the environment of interest.

As an example, Figure 2.11 demonstrates the concept of critical charge, which is defined as the charge required to induce an upset in an SRAM cell [67]. Two transients are shown in Figure 2.11 with different amounts of total charge being collected and the resulting transient on the output of the off-state transistor in an SRAM cell. The top image of Figure 2.11 shows a transient corresponding to 0.23 pC of charge collection within the SRAM cell. The state of the cell is temporarily perturbed, however, the resulting transient is insufficient to cause the SRAM cell to latch into an erroneous information state.

In the bottom image of Figure 2.11, the transient shown corresponds to 0.25 pC of

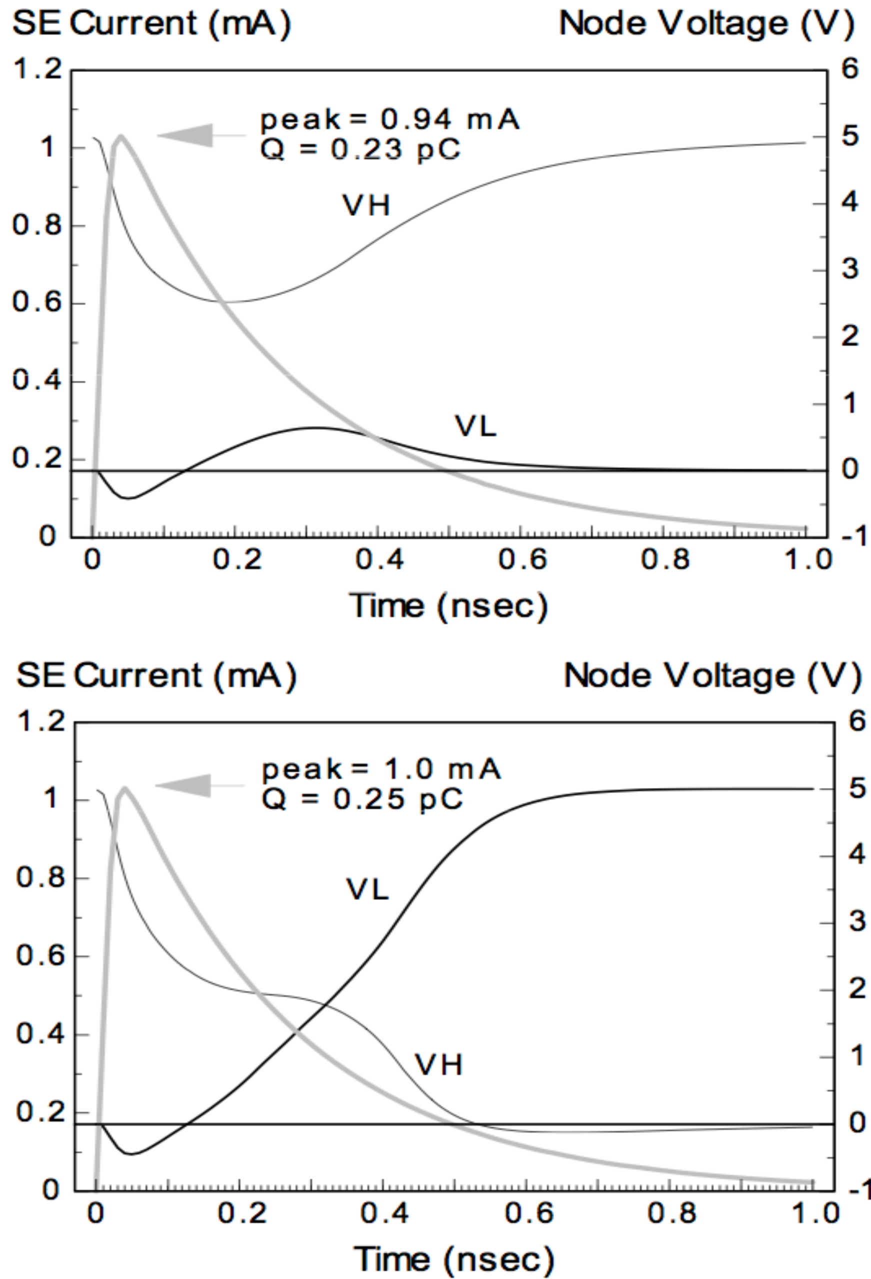

Figure 2.11 Current transients in an SRAM cell demonstrate the concept of critical charge. The transient corresponding to 0.23 pC of charge collection is insufficient to cause the SRAM cell to latch into an erroneous state. However, when the amount of collected charge is increased to 0.25 pC the resulting transient is latched into the SRAM cell, resulting in an error [67].

charge collected in the SRAM cell. While the magnitude of charge collection differs by only 0.02 pC, the resulting circuit response is dramatically different. The resulting transient is of sufficient magnitude and duration to latch an erroneous state into the SRAM cell, resulting in an externally visible error. The critical charge of this SRAM cell would therefore be defined to be 0.25 pC since a typical SRAM cell response for the corresponding technology node would result in an error.

There are many nuances and specific details that may impact the error margins for determining critical charge such as corner to corner variations, magnitude and duration of the transient pulse, and charge collection efficiency [40, 69–72]. However, Figure 2.11 is intended to convey the concept of critical charge, which is defined in this dissertation as a single valued metric for determining the energy deposition threshold for the onset of errors in an SRAM cell. The magnitude of charge collection shown in Figure 2.11 is large when compared to the critical charge for sub-65 nm technology nodes as discussed in Chapters 3 and 4.

The first attempts to quantify the critical charge of SRAMs developed circuit models from known topologies and process information to be used in SPICE simulations [73, 74]. SPICE simulations were performed using double exponential current pulses to emulate the current transient response of an SRAM cell and evaluate whether cells were susceptible to upset. This methodology has proven robust over the years and is still commonly used. In a similar fashion, Buehler *et al.* used this SPICE simulation technique and analysis to show the SRAM cell critical charge dependence on supply voltage, those results are shown in Figure 2.12 [73]. Small decreases in supply voltage are shown to result in linear modulation of the SRAM cell critical charge. This trend continues until a large discrepancy between applied and nominal supply voltage results in SRAM cell instability, causing spontaneous errors in the memory array as shown by the change in slope of Figure 2.12 around 1.9 V. Understanding the lower

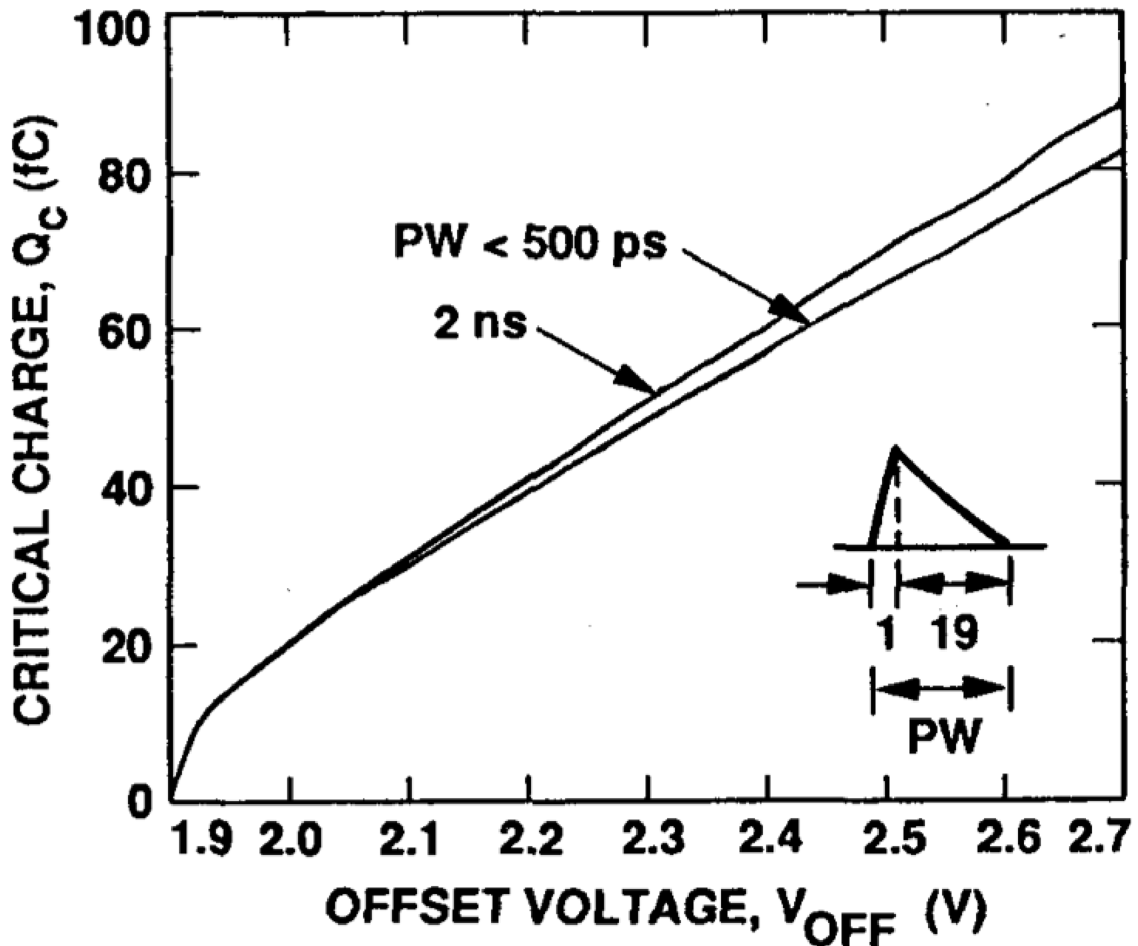

Figure 2.12 SPICE analysis an SRAM cell critical charge dependence on supply voltage from [73].

limit of critical charge also informs regions of stable operation for an SRAM as the memory is functional and maintains valid data for supply voltage conditions above this threshold. While the magnitude of critical charge in Figure 2.12 is large compared to SRAMs fabricated in sub-65 nm technology nodes, the conceptual discussion above is still valid and serves as an informative case study.

The critical charge dependence of SRAMs on supply voltage is only one part of a complicated story. In addition to the supply voltage, the SEU response also depends on the LET of the incident particle. The SEU bias and LET dependence of

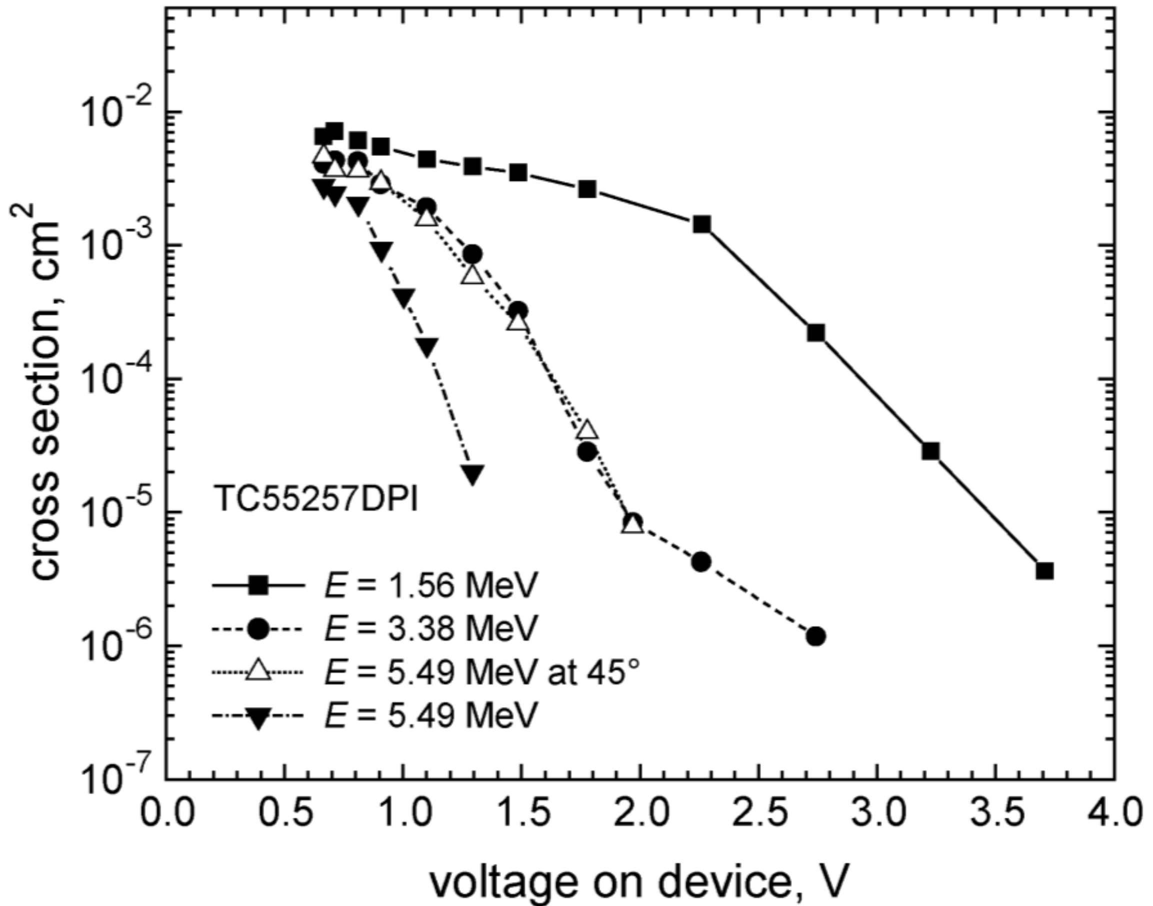

Figure 2.13 SEU cross-section bias dependence of an SRAM for alphas with energies 1.56, 3.38, and 5.49 MeV, with LETs (in the sensitive volume) of 1.52, 0.87, and 0.64 MeV-cm^2/mg, respectively. After [76].

SRAMs has been discussed previously in [73, 75, 76]. In [76], Barak *et al.* used alpha particles to show the SEU cross-section bias dependence on supply voltage, those results can be seen in Figure 2.13. The SEU cross-sections shown in Figure 2.13 exhibit a complicated dependence on applied bias. In some supply voltage regions, the SEU bias dependence shows a clear exponential trend, while in others it appears more linear. It is clear, however, that for decreasing supply voltage the SEU cross-section is a monotonically increasing function.

Additionally, Figure 2.13 shows a dependence on the incident ion LET. Higher

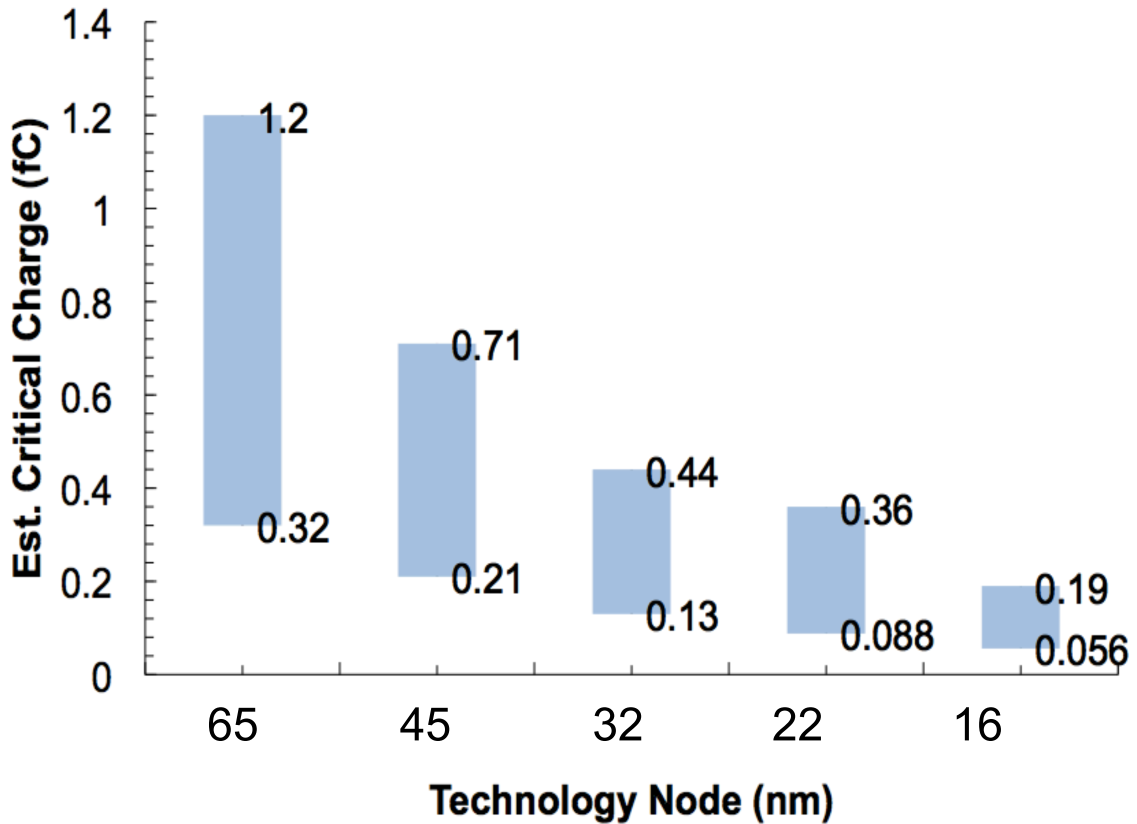

Figure 2.14 Estimation of critical charge as a function of technology node feature size [21].

LET alpha particles are observed to have a higher cross-section under large applied bias conditions as compared to lower LET alpha particles. Higher LET alpha particles also exhibit a non-uniform slope in corresponding SEU cross-sections. This is because continued reduction in supply voltage modulates the critical charge below the average charge generated within the sensitive volume by the incident alpha particles, which in turn results in only a moderate increase in the measured cross-section. Due to the low onset voltage for more lightly ionizing particles, this feature may be reduced or absent from the SEU cross-section versus supply voltage figures as shown by the lower LET alphas (5.49 MeV) in Figure 2.13. These trends have also been shown in other works for heavy-ions, alphas particles, and low-energy protons in [1, 13, 73, 75, 76].

In [21], Sierawski attempted to estimate the critical charge for several current- and next-generation technology nodes. The resulting calculations can be seen in Figure 2.14. Using SPICE simulations and injecting current pulses of varying magnitude and duration Sierawski was able to obtain an upper bound for critical charge. The lower bounds were obtained by extracting process details from the ITRS road map [77] and applying the following relation,

$$Q_{crit} = \frac{V_{DD}}{2}\frac{\epsilon_{SiO_2}\epsilon_0 A_{cell}}{t_{ox}} \tag{2.9}$$

where V_{DD} is the supply voltage for the technology node, ϵ_0 is the permittivity of free space, ϵ_{SiO_2} is the relative permittivity of SiO_2, A_{cell} is the cell area, and t_{ox} is the equivalent SiO_2 oxide thickness for the technology node. Figure 2.14 shows an overall decrease in critical charge with decreasing technology node feature size. These conclusions are consistent with publications that indicate the critical charge of 65 nm silicon-on-insulator SRAMs is between 0.21 and 0.27 fC [1].

While much of the energy lost by the incident ion results in the generation of *e*-*h* pairs by direct ionization, secondary particles also deposit energy in regions surrounding the incident ion path and have been reported to contribute to the SEU response. The secondary particles of concern are generated by incident particles through nuclear elastic, inelastic or spallation reactions, or Coulomb scatters, known as "knock-ons," which are atoms displaced from the crystal lattice. Several studies have also investigated the potential contribution of energetic electron, or δ-ray, induced SEUs with mixed conclusions. Some reports indicate that δ-rays may contribute to the overall single- and multiple-bit upset cross-section in a heavy-ion environment [9,10]. Others have found that δ-rays in such an environment do not contribute significantly to a measureable upset cross-section [7,8,11]. The generation and interactions of δ-rays in a heavy-ion environment is discussed in Section 2.5.

This dissertation demonstrates SEUs for SRAMs exposed to a source of electrons and investigate the significance and contribution of electron-induced SEUs to error-rates in the space radiation environment.

2.3.2 Low-Energy Proton-Induced SEUs

The primary effects due to incident protons on microelectronics in the space radiation environment have historically been DD, TID, and SEUs caused by nuclear spallation reactions [39, 78–80]. The contribution of protons to upset cross-sections due to direct ionization has traditionally been ignored since the electronic stopping power of protons is quite small. However, a series of papers demonstrated protons near their end of range were capable of generating sufficient charge to upset SRAMs and latches fabricated in a 65 nm node [1, 13–15, 81].

The Bragg peak for protons occurs near their end of range, implying that protons near stopping have a maximum LET. By exposing SRAM and latches to a source of low-energy protons, in the energy range of 1-2 MeV, Heidel and Rodbell were able to show that proton-induced direct ionization can cause upsets in SRAMs fabricated in 45 nm and 65 nm technology nodes [1, 14, 81]. Because SOI technology has a large angular dependence [36], direct ionization effects due to protons were confirmed by performing experiments at large angle of incidence. Rotating parts using a goniometer in order to test parts at large angle of incidence, where a beam normally incident on the device under test is considered to be 0°, resulted in an increased upset rate. This is due to an increased path length for incident protons through the active region of the test chip, corresponding to more energy deposited within the sensitive region of the SRAM [81].

Figure 2.16 shows the proton SEU cross-section as a function of incident proton energy for 45 nm and 65 nm SRAMs. For very energetic incident protons (>10 MeV)

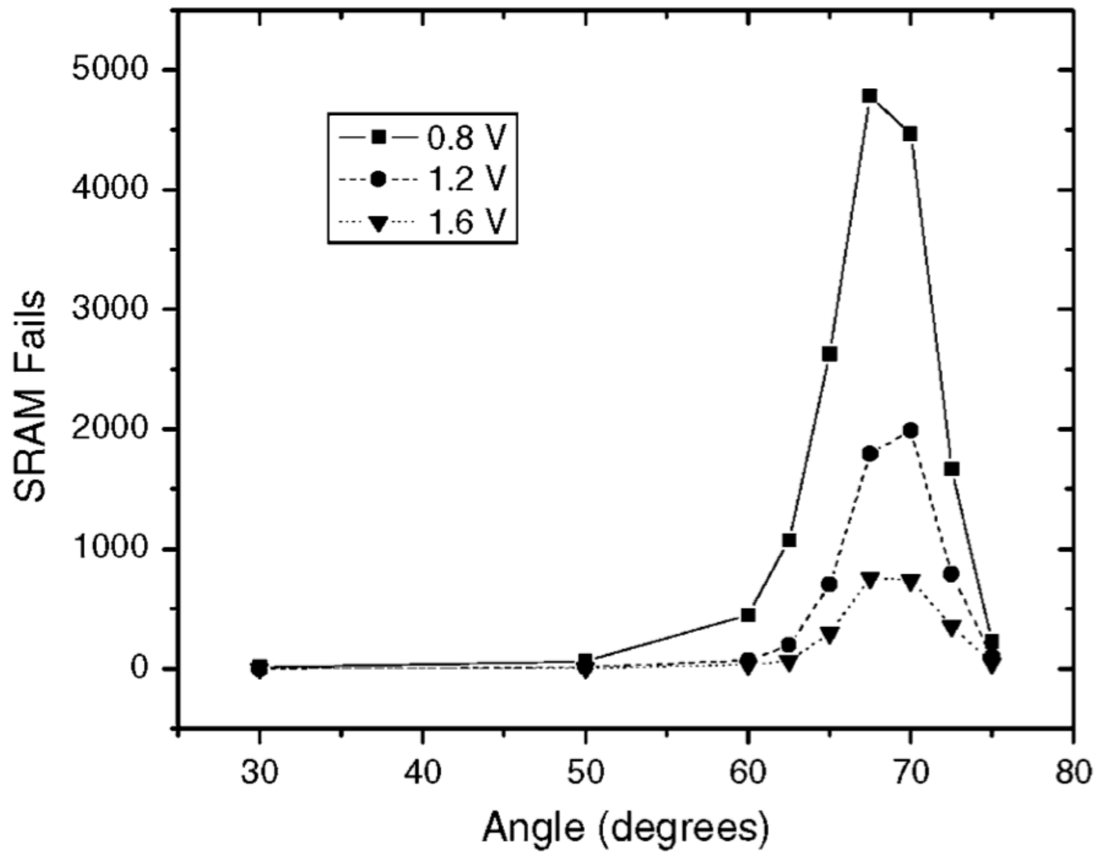

Figure 2.15 SRAM fails (an average of write *1* and write *0*) as a function of the incident angle for an SRAM array at 0.8 V, 1.2 V and 1.6 V using 1.5 MeV protons [1].

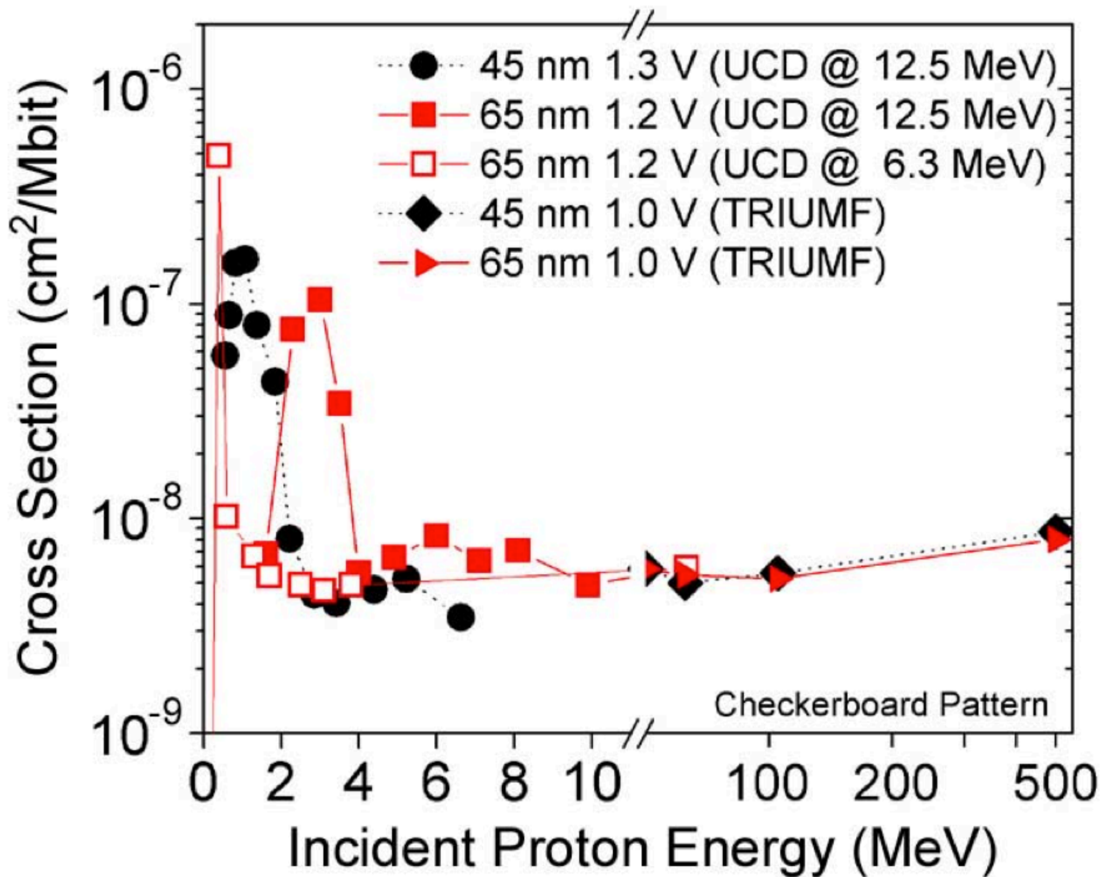

Figure 2.16 The SBU cross-section versus proton energy for both 45 nm and 65 nm SOI SRAMs [14].

upsets can be attributed to nuclear reaction events. In this energy range, the SEU cross-section remains relatively constant. As the incident proton energy is reduced (<5 MeV) the measured upset cross-section begins to increase, corresponding to protons with sufficient LET to upset the device under test. Incident proton energies between 1–4 MeV correspond to a "plateau" in the measured upset cross-section. In this region, the upset cross-section is two orders of magnitude higher than the high-energy proton cross-section and corresponds to a region where most of the incident protons are near their end of range. Decreasing the incident proton energy further results in a reduced SEU cross section. This is due to a corresponding reduction in

the range of incident protons and prevents them from transporting into the sensitive region of the device with sufficient energy to impact the SRAM cells' nominal operation.

Multiple supply voltage conditions were used for SRAMs fabricated in the 45 nm and 65 nm technology node and are shown in Figure 2.16. The sensitivity of SRAMs to low-energy protons was first observed under reduced bias conditions at high angle of incidence [81]. Further study showed sensitivity of 45 nm SRAMs at normal incidence and under nominal bias conditions [1, 14]. A plot showing the SEU cross-section dependence on applied bias, in arbitrary units, can be seen in Figure 2.17 for 1 and 1.5 MeV protons (also more energetic alpha particles are shown). A gentle gradient can be observed in the SEU cross-section for low-energy protons (the curve corresponding to 1 MeV protons) as a function of applied bias. Recalling the discussion regarding Equation 2.9, the critical charge of elementary 6T-SRAM cell should depend on the supply voltage [73–75]. In Figure 2.17, the bias dependence manifests as a increase in the normalized failure rate for decreasing supply voltage on the device. The SEU cross-section bias dependence is consistent with previous studies by Buehler [73] and Barak [75, 76] that show a dependence on both incident ion LET and supply voltage for SRAMs in several different technology generations. Heidel and Rodbell both reported the critical charge for SRAMs fabricated in the 65 nm SOI technology node to have a critical charge between 0.21 fC and 0.27 fC [1,81]. The values of critical charge from [1,81] are consistent with the estimations for SRAMs in the 65 nm technology node made by Sierawski and shown in Figure 2.14. Interestingly, the reported values of critical charge correspond to 1300-1700 collected electrons. The observation of effects from low-energy protons signifies a noteworthy shift in the sensitivity SRAMs fabricated in sub-65 nm technology nodes.

The primary impact of these results is the device response to the space radiation

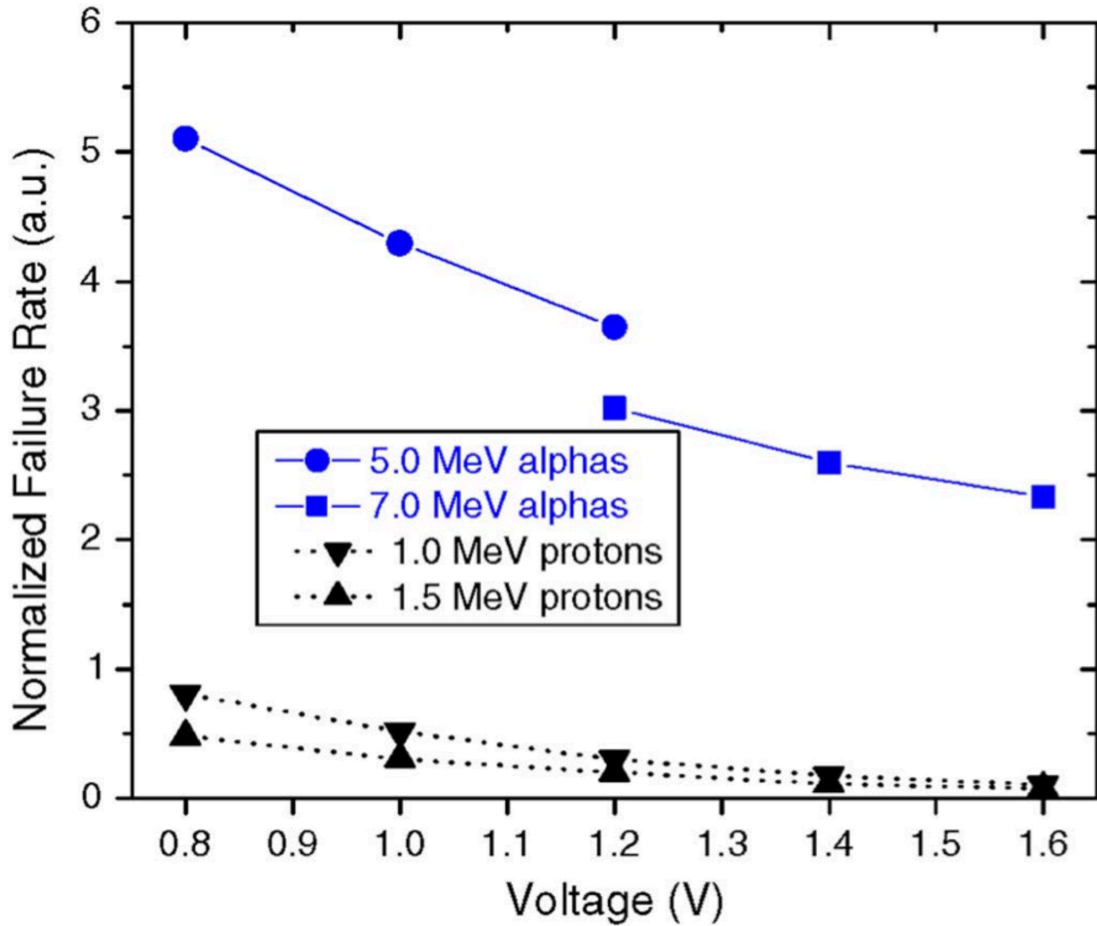

Figure 2.17 Plot of the SRAM SEU cross-section (in arbitrary units) as a function of voltage for 5.0 MeV and 7.0 MeV alpha particles and for 1.0 MeV and 1.5 MeV protons [1].

environment, where energy loss through spacecraft shielding can shift the differential flux spectrum of protons towards lower energies, so that direct ionization effects begin to contribute to the SEU cross-section and error rates [15]. Nuclear reactions involving more energetic protons and/or the heavy ions from the galactic cosmic ray environment also result in the generation of large numbers of protons [1]. The contribution of low-energy protons also extends to the terrestrial environment where neutron-induced spallation reactions produce a substantial number of low energy protons [1].

2.3.3 Muon-Induced SEUs

Wallmark and Marcus performed a preliminary analysis of the fundamental limitations of microelectronics and highlighted ionizing radiation particles, chief amongst these were muons and electrons in the terrestrial environment, as the principal factors that would impact the continued reliable scaling of semiconductor devices and technology [22]. Additional analysis regarding error rates and the sensitivity of SRAMs was performed by Ziegler *et al.* The results of that work suggested that the continued scaling of CMOS memory would result in a substantial increase in the sensitivity of SRAMs to ionizing radiation with continued device scaling and result in a large soft-error rate for the space and terrestrial radiation environments [82].

As described in the previous section, research has shown commercial SRAMs are vulnerable to low-energy proton-induced SEUs due to the relatively small critical charge required to cause an error in modern SRAMs. This revelation has changed the way the radiation effects and reliability community view lightly ionizing radiation. Contributions of low-energy protons to upset cross-sections, as discussed previously, were traditionally ignored. They are now being considered as a real and significant reliability concern. For many years, the presence of atmospheric neutrons and alpha particles (the result of packaging impurities) represented the primary sources of soft errors at the terrestrial level. Muons, the most abundant species at the terrestrial level, have recently been shown to induce SEU in sub-65 nm SRAMs [2, 16, 21].

Like protons, muons are singly-charged particles with a mass roughly 200 times that of the electron mass. Figure 2.18 shows the stopping power, or mass stopping power, the rate of energy loss per unit path length, for a variety of particle species. The curves for protons and muons are similar having a comparable magnitude. The difference in the stopping power curves is due to the lower mass of the muon when

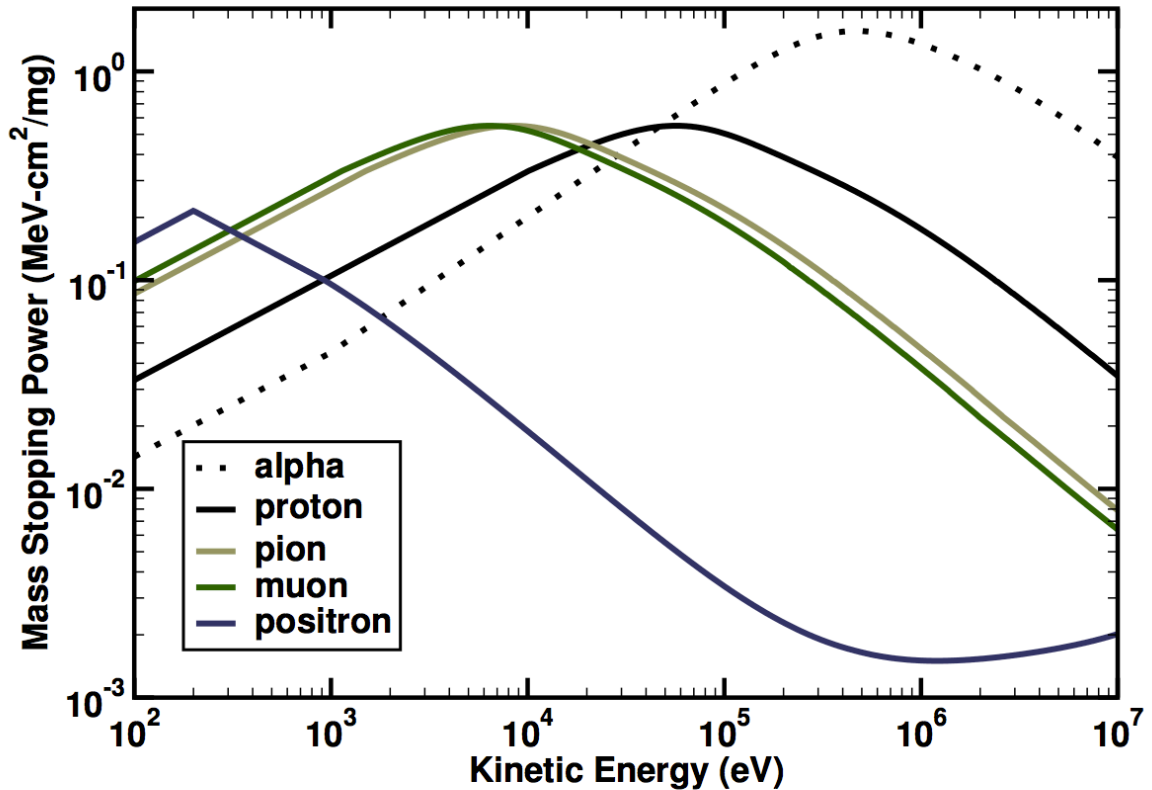

Figure 2.18 Mass stopping power extracted from Geant4 for protons, pions, muons, and positrons in silicon. Alpha particle stopping power shown for reference [16].

compared to that of protons. This parallel indicates that the energy deposition from stopping muons would be comparable to that of low-energy protons. By induction, muons could therefore contribute to the soft error rate, particularly in the terrestrial environment, of SRAMs that exhibit sensitivity to low-energy protons.

Sierawski *et al.* demonstrated that stopping muons were indeed capable of upsetting SRAMs fabricated in the 65 nm technology under reduced bias conditions [2]. Figure 2.19 plots the muon-induced upset cross-section as a function of incident muon energy. The characteristics of Figure 2.19 are quite similar to low-energy proton SEU cross-sections. There is a flat region corresponding to higher energy muons and as the incident muon energy is reduced there is an abrupt increase in the SEU cross-section.

Further reductions in incident muon energy result in particles with insufficient range to reach the sensitive region of the SRAM. Consequently, the lowest energy muons do not contribute to the upset cross-section.

Figure 2.20 shows the SEU response of a 65 nm SRAM as a function of supply voltage for incident muons with average energy of approximately 400 keV. For a nominal supply voltage of 1.2 V, few errors are observed. As the applied bias is reduced, there is a corresponding increase in the number of muon-induced upsets. As discussed regarding Equation 2.9 and the bias dependence of low-energy protons in Section 2.3.2, reduction in supply voltage results in a corresponding reduction in critical charge. Consequently, reduction in critical charge with decreasing supply voltage makes the SRAM test chip vulnerable to a wider range of incident muon energies, which explains the bias dependence shown in Figure 2.20.

The impact of muon-induced SEUs parallels that of effects due to low-energy protons. The contribution of each has traditionally been considered negligible to the overall SEU cross-section and/or SER of modern SRAMs and has only recently been observed to contribute to error rates. Ultimately, the observation of upsets due to low-energy protons and muons signal that commercial SRAM components are becoming increasingly sensitive to effects from a wider range of ionizing particle species. The main goal of this dissertation is to expand on the observation of upsets due to lightly ionizing, singly-charged particles (low-energy protons and muons) and investigate whether SRAMs fabricated in modern, sub-65 nm technology nodes exhibit SEU sensitivity to ionization from energetic electrons.

2.3.4 SRAM Cell Imprinting

CMOS devices exposed to ionizing radiation can experience threshold voltage shifts and decreased carrier mobility as a result of accumulated dose in oxides and the

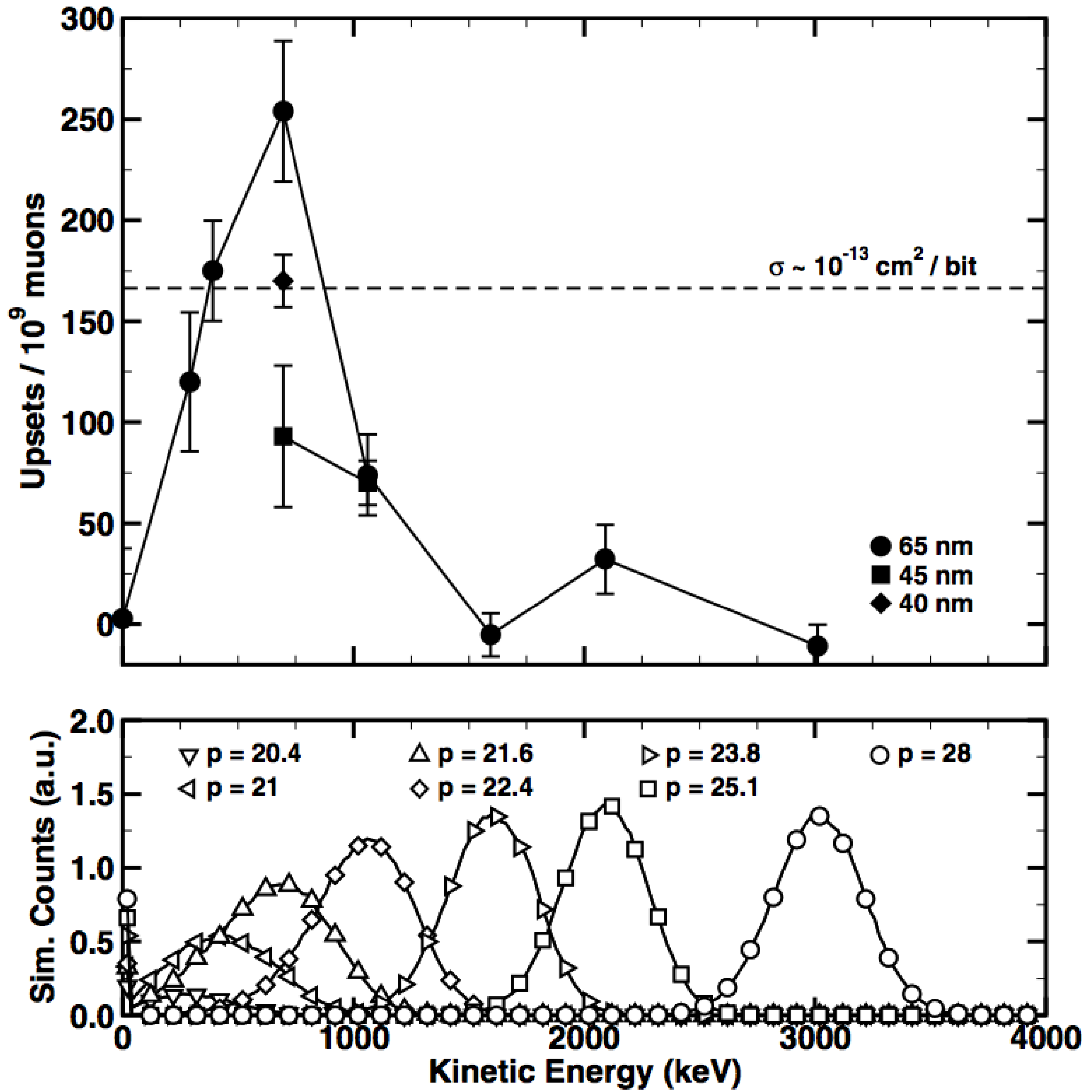

Figure 2.19 Simulated muon kinetic energy distributions, as seen at the front of the part, corresponding to experimental momenta including upstream energy losses and straggling (bottom). Error counts for 65 nm, 45 nm, and 40 nm SRAMs versus estimated muon kinetic energy at 1.0 V bias (top). Dashed horizontal line represents an approximate muon-induced SEU cross section for reference [2].

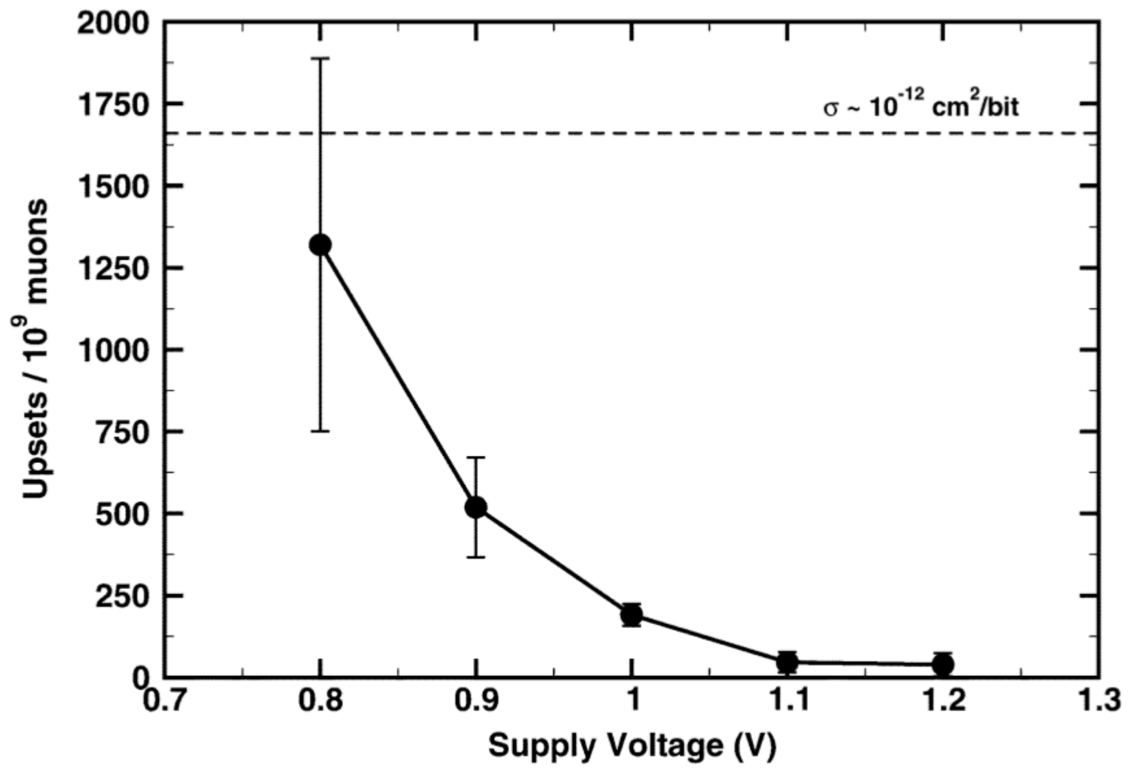

Figure 2.20 Error counts for 65 nm SRAM versus supply voltage for approximately 400 keV muons produced by 21 MeV/c momentum selection. Dashed horizontal line represents an approximate muon-induced SEU cross section for reference [2].

formation of interface traps [83–86]. The severity of radiation-induced degradation in devices is a complicated interaction dependent on the bias conditions during and after exposure. Because the drive strength of n-channel MOSFETs is much higher than p-channel devices, the total-ionizing dose (TID) response of CMOS SRAMs depends strongly on parametric shifts in the nMOSFET device elements [87, 88]. While process hardening efforts may improve the circuits tolerance to TID, designs may still experience functional failure due to speed and timing degradation [88, 89].

Radiation-induced threshold voltage shifts in the nMOSFET elements of CMOS SRAMs were initially reported to cause an imbalance in device turn-on voltages [90]. The data state of an SRAM establishes bias conditions for the transistor elements of the cross-coupled inverter when exposed to a source of ionizing radiation. The resulting cell imbalance of nMOSFET threshold voltages causes in an asymmetry in switching voltage and SNM that is dependent on the stored data state of the cell. Fleetwood *et al.* published a study seeking to quantify the "worst-case" SRAM radiation response by evaluating common bias combinations for the transistors comprising an SRAM cell. In [88], the bias conditions are evaluated to a total dose of 1 Mrad(Si) and the results can be seen in Figure 2.21. During irradiation the initial threshold voltage shift, for both the "on" and "off" conditions, is negative, consistent with the build-up of charge in the gate oxide region [83, 84]. For consistency, the *1* state of the SRAM cell is defined to be when Q is low, that is when the transistor M3 of Figure 2.9 is "on". Figure 2.21 indicates that the devices irradiated in the "off" state experience a larger threshold voltage shift than those irradiated in the "on" state. Additional exposure of the n-channel devices shows a rebound effect, which is attributed to the accumulation of interface traps that begin to dominate the device response [84,85]. Figure 2.21 shows that the accumulation of interface traps continues even after irradiation, resulting in large, positive threshold voltage shifts for each bias

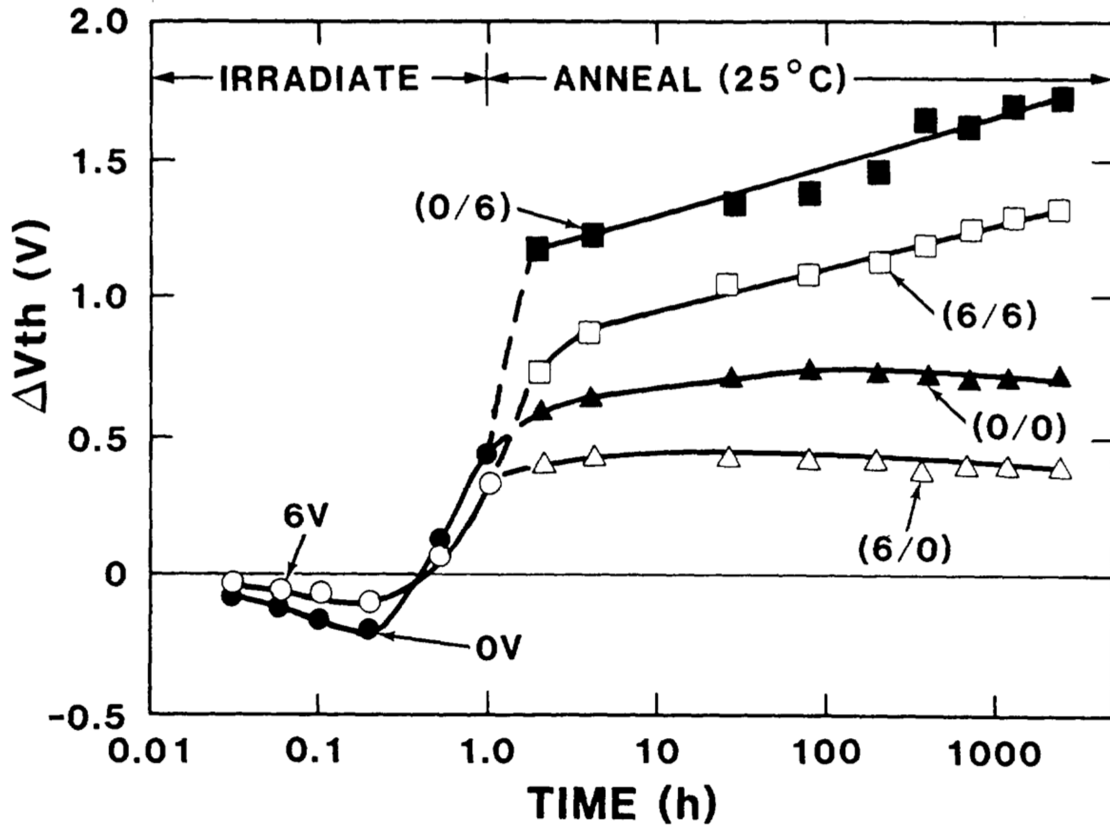

Figure 2.21 ΔV_{th} versus time, for n-channel transistors irradiated to 1.0 Mrad(Si) and annealed at 25°C [88].

condition.

The threshold voltage imbalance, V_{imb}, induced by bias conditions during irradiation can be quantified as

$$V_{imb} = V_{TM1} - V_{TM3} \tag{2.10}$$

where V_{TM1} is the nMOSFET transistor with the largest threshold voltage after irradiation and V_{TM3} has the less positive threshold voltage. As defined in Equation 2.10, a positive value of V_{imb} implies a preferred *1* state for the SRAM cell. Conversely, a negative value of V_{imb} implies a preferred *0* state for the cell.

A plot of threshold voltage imbalance versus irradiation and annealing time from [88] can be seen in Figure 2.22 for conditions where the cell is initially in a *1* state

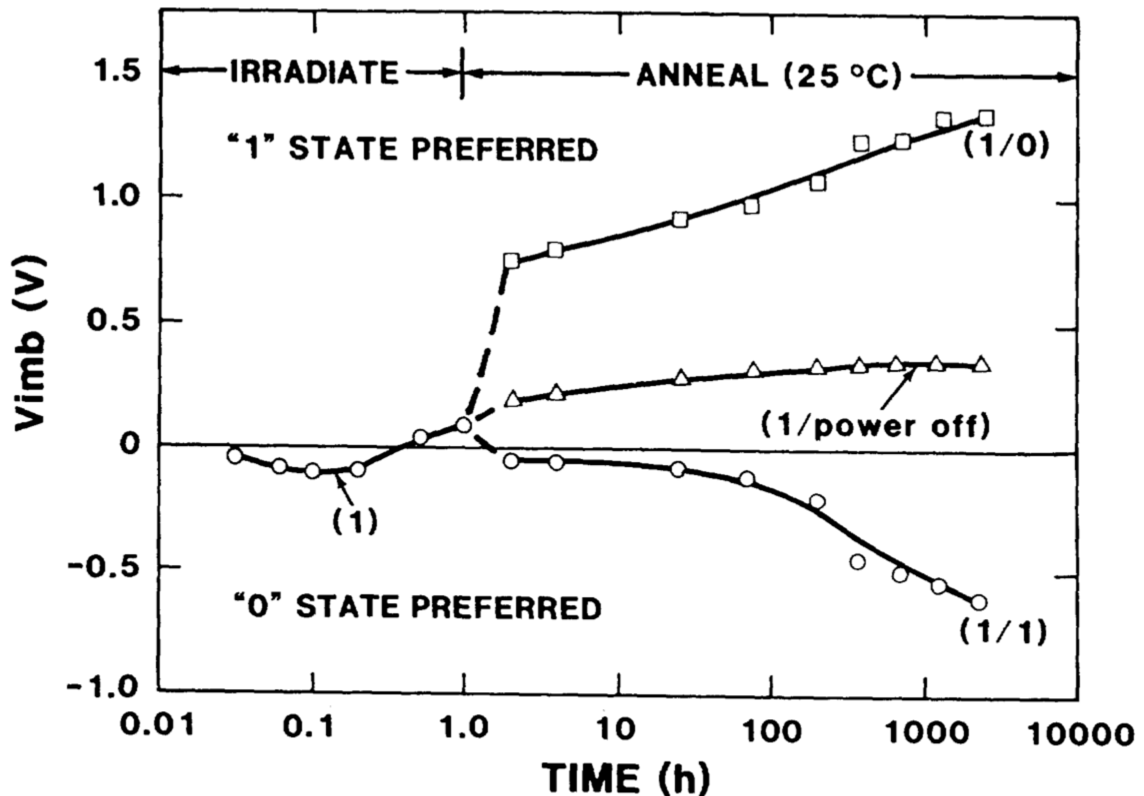

Figure 2.22 SRAM cell imbalance versus radiation and anneal time, based on the data of Figure 2.21.

during irradiation and the cell state is either retained, rewritten, or power is removed from the cell during annealing. Initial reports indicated that the SRAM cell was "imprinted" and the preferred state exclusively became that which it was irradiated under, however, Figure 2.22 shows an initial preference for the *0* state when the programmed pattern was the *1* state. The preferred state of the SRAM therefore depends on bias conditions during irradiation and total dose accumulated [88]. Cells irradiated in the *1* state and annealed in the *0* state show the strongest preference for the *1* device state. These bias conditions correspond to the largest positive threshold voltage shift in M1 and the least positive threshold voltage shift in M3, as shown in Figure 2.21. These conditions result in the largest speed and timing penalty, as well

as the largest SRAM cell imbalance and are considered the "worst-case" conditions for TID in SRAMs.

The speed, timing degradation, and SRAM cell imbalances described above contribute to increased leakage current and functional failure of the SRAM cell. Aggressive scaling of CMOS features size has resulted in a decrease in gate oxide thickness. The magnitude of threshold voltage shifts observed in more modern technology nodes has reduced relative to nominal supply voltage. For a highly optimized process, even small changes in operating points can be a significant issue. In this case however, scaling has improved commercial CMOS tolerance to TID [89, 91]. Investigations by Felix and Yao have studied TID effects on more recent commercial CMOS SRAMs and conclude that below 90 nm SRAMs are resistant to "pattern imprinting" effects [89, 92, 93]. Along those lines, functional device failure at the 130 nm node did not typically occur until 200-400 krad(SiO_2) of dose accumulated within the device. The failure mechanism was no longer reported to be threshold voltage shifts and mobility degradation, but increased sidewall leakage at the shallow trench isolation (STI)–silicon interface, an issue that has become increasingly problematic for current-generation technology nodes [89, 91]. Accumulation of charge in the STI activates a parasitic sidewall transistor along the edge of the device acting as a constant bias condition that may deplete or, given sufficient dose, invert nearby active silicon resulting in a static increase in leakage current. The impact of charge build up in STI on transistor I-V characteristics is shown in Figure 2.23. It is important to note the lack of threshold voltage shift in Figure 2.23, instead a semi-static leakage increase is seen in the "off" region of the n-channel device, swamping the device response at high dose and reducing the on/off current ratio by many orders of magnitude. This is problematic for present-generation technology nodes because increased leakage currents can interfere with proper pre-charging and signal development on bit-lines [92].

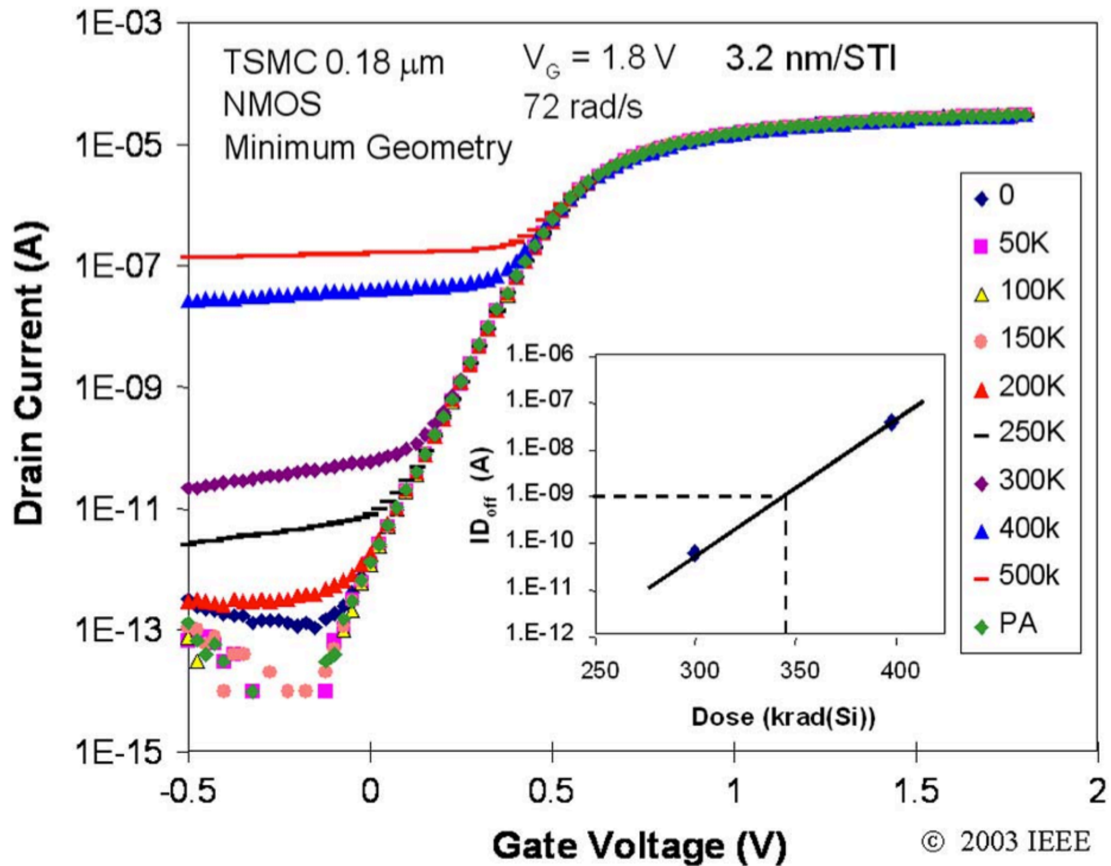

Figure 2.23 Impact of STI radiation damage on the current-voltage characteristics of nMOSFET fabricated in TSMC 0.18 μm CMOS [91]

As a consequence of degraded speed, timing, threshold voltage imbalances, and increased leakage, irradiated SRAMs exhibit reduced SNMs and have been reported to have increased sensitivity to SEU from heavy-ion and transient irradiation [88, 89, 92, 94, 95]. In [92], the 90 nm technology node did not exhibit a significant increase in supply current until approximately 300 krad(Si). This is also the point at which "imprinting" began to become significant across the entire test chip. Despite a dramatic increase in supply current, the devices were reported to remain functional while maintaining the programmed state to a total dose of 1 Mrad(Si).

Yao *et al.* used Monte Carlo simulations to infer the change in inverter transfer

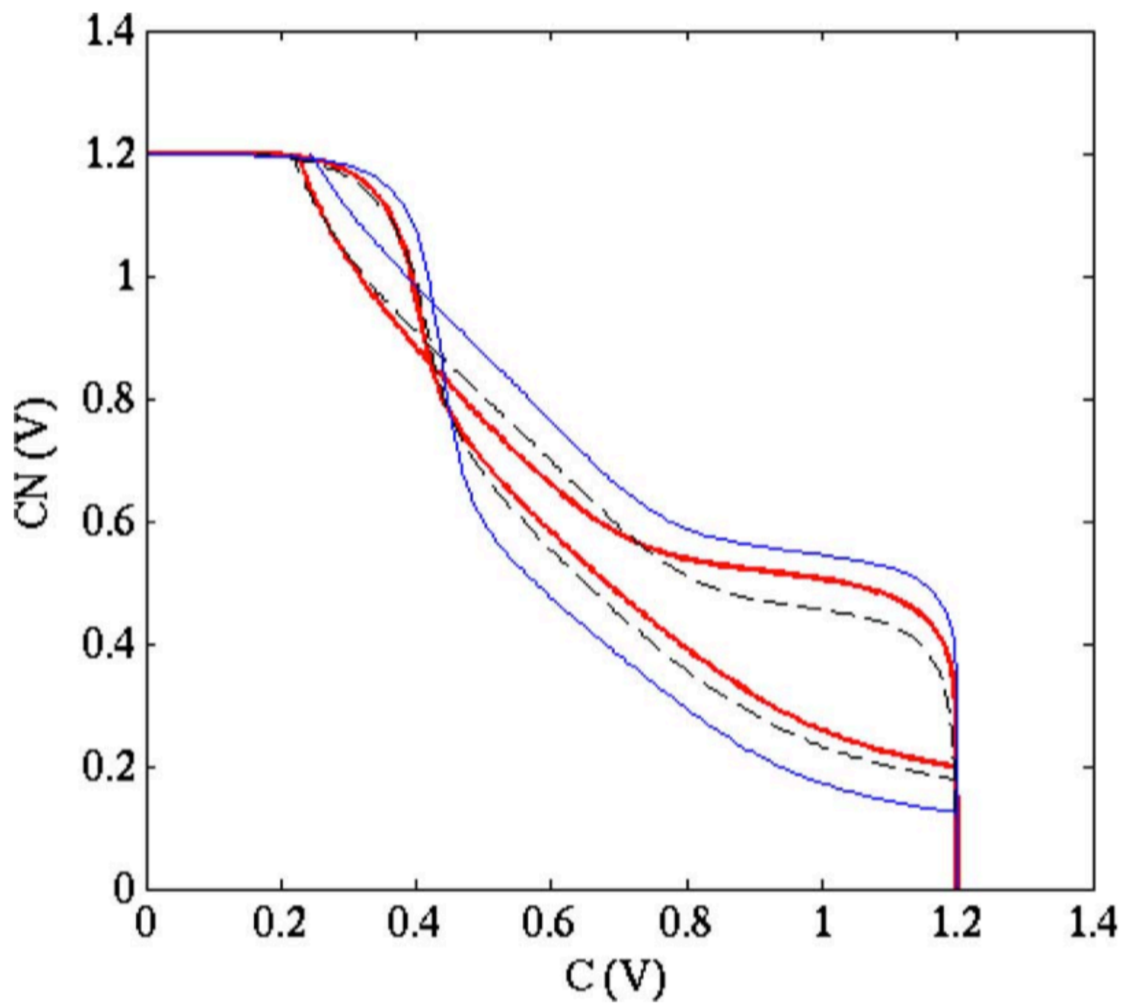

Figure 2.24 Worst-case Monte Carlo derived read SNM pre- and post-irradiation. The thin blue and dashed green lines show the post-irradiation SNM, while the thick red lines show the pre-irradiation response. The worst-case, i.e., the smallest box that fits within the "eyes" is improved after irradiation [92].

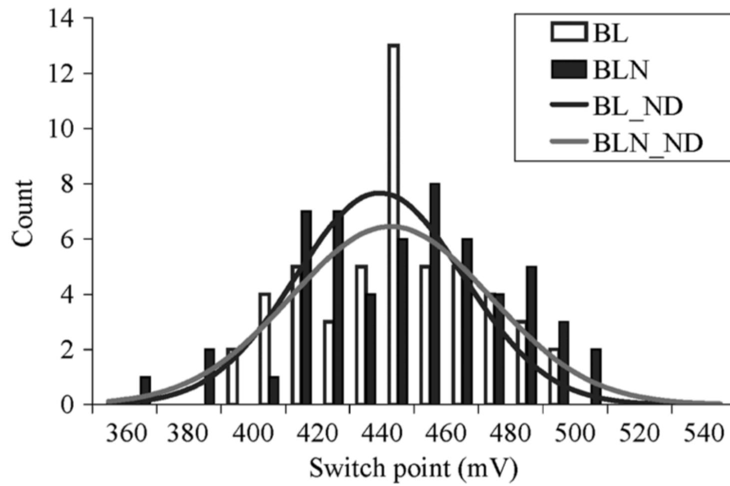

(a)

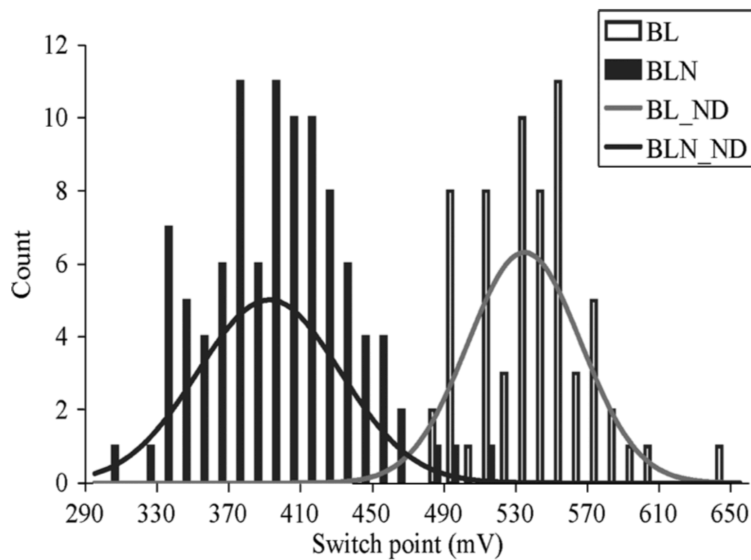

(b)

Figure 2.25 Pre-irradiation SRAM cell trip points measured driving the BL and $\overline{BL}$, shown in (a). BL_{ND} and $\overline{BL}_{ND}$ are normal distribution curves for the SRAM DC switch point. In (b), measured SRAM cell node trip points after irradiation to 1.5 Mrad(Si). The BL trip points are shifted up, i.e., the write margin is increased (easier write) and the $\overline{BL}$ write margin is reduced (it becomes more difficult to write). After [92].

characteristics as a result of TID in a 90 nm technology node, which can be seen in Figure 2.24. The thin blue and dashed green lines show the post-irradiation SNM, while the thick red lines show the pre-irradiation response. The worst-case, i.e., the smallest box that fits within the "eyes" is improved after irradiation. The transfer characteristics shown in Figure 2.24 are drastically different from the symmetric response discussed previously regarding the 22 nm node and shown in Figure 2.10. Figure 2.25 shows the pre- and post-irradiation SRAM cell switching points for the bit-line and bit-line complement. The pre-irradiation data show a symmetric, balanced cell response, indicating that neither cell state is preferred by the SRAM cell. After exposure to 1.5 Mrad(Si) the characteristics shift forcing the cell into an asymmetric state where the BL is easier to write than the $\overline{BL}$. Within some margin this constitutes functional SRAM cell failure, where it becomes nearly impossible, or at least exceedingly difficult, to read or write an SRAM cell and maintain valid data in the standby mode.

2.3.5 Impact of Transient Radiation on SRAMs

When semiconductor materials are exposed to high-intensity, penetrating radiation, such as X-rays or γ-rays, e-h pairs are generated that may be collected and contribute to the cumulative photocurrent. Photocurrents arise from high-flux irradiation conditions, such as those obtained from flash X-ray and pulsed reactor sources, and are "global" currents resulting from irradiation across an entire chip. Because generated photocurrents are "global", every device on a common substrate contributes to the collection of generated e-h pairs during irradiation.

In 1964, Wirth and Rogers developed a mathematical model based on the continuity and diffusion equations that describes the transient currents generated as a result of high-intensity irradiation [96]. The model presented by Wirth and Rogers

was refined and applied to the case of bipolar transistors by Long *et al.* in [97], which accounted for differences in diffusion length and carrier lifetimes associated with an epitaxial layer on a highly doped substrate. The conditions evaluated in [97] are analogous to the case of SRAM cell well junction photocurrents when exposed to a transient radiation environment.

Massengill *et al.* applied the models and analysis presented in [97] to the case of transient radiation upsets in CMOS SRAMs in [98–100]. Figure 2.26 plots the photocurrent produced at the drain nodes and p-well within an SRAM cell resulting from transient irradiation corresponding to a dose-rate of 5 Grad(Si)/sec. The largest photocurrents correspond to the p-well contact in both the bulk (2.26(a)) and epitaxial (2.26(b)) cases. These photocurrents, which occur in every device across the entire chip, contribute to a non-negligible increase in power supply current.

Figure 2.26 shows that errors occuring in a single SRAM cell are unlikely to be a local effect, since the magnitude of transients corresponding to the drain nodes within the SRAM cell are smaller than the well photocurrent. Instead, the onset of upsets resulting from transient irradiation of an SRAM test chip are related to the collective photocurrent of each well contact on the test chip [98]. This is due to the finite resistance of metal interconnects, the resulting photocurrents cause a voltage drop in V_{DD} and an increase in V_{SS} across the entire test chip. The resulting decrease in rail voltage (V_{DD}-V_{SS}) results in a higher than expected SRAM sensitivity to errors during transient irradiation [98]. An example of the equivalent circuit diagram of an SRAM cell including interconnect resistances for V_{DD} and V_{SS} is shown in Figure 2.27. The resistances shown in parallel are labeled R_{DDV} and R_{SSV} corresponding to the finite resistance drop between individual SRAM cells on the high and low voltage rails, respectively. Because the highest photocurrents are associated with charge collection on the p-well node of an SRAM cell, the largest change in supply voltage occurs for

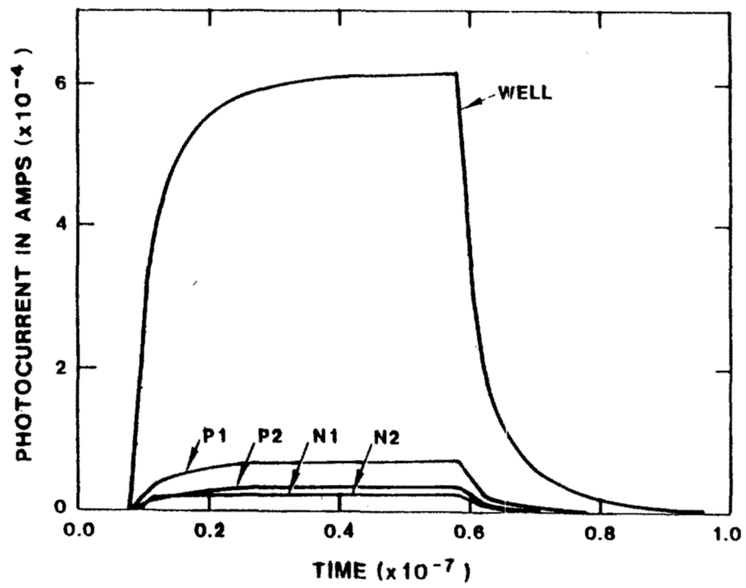

(a)

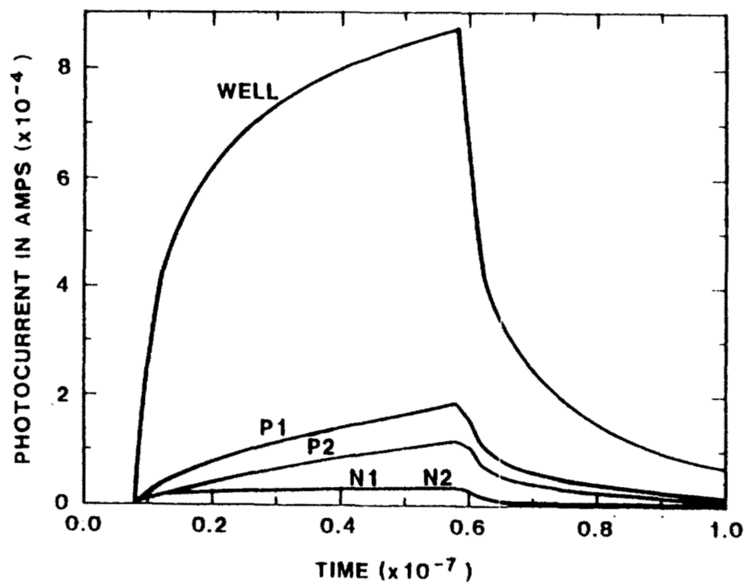

(b)

Figure 2.26 Photocurrent waveforms, at a dose rate of $5{\times}10^9$ rad(Si)/sec for the (a) bulk and (b) epi cases [98].

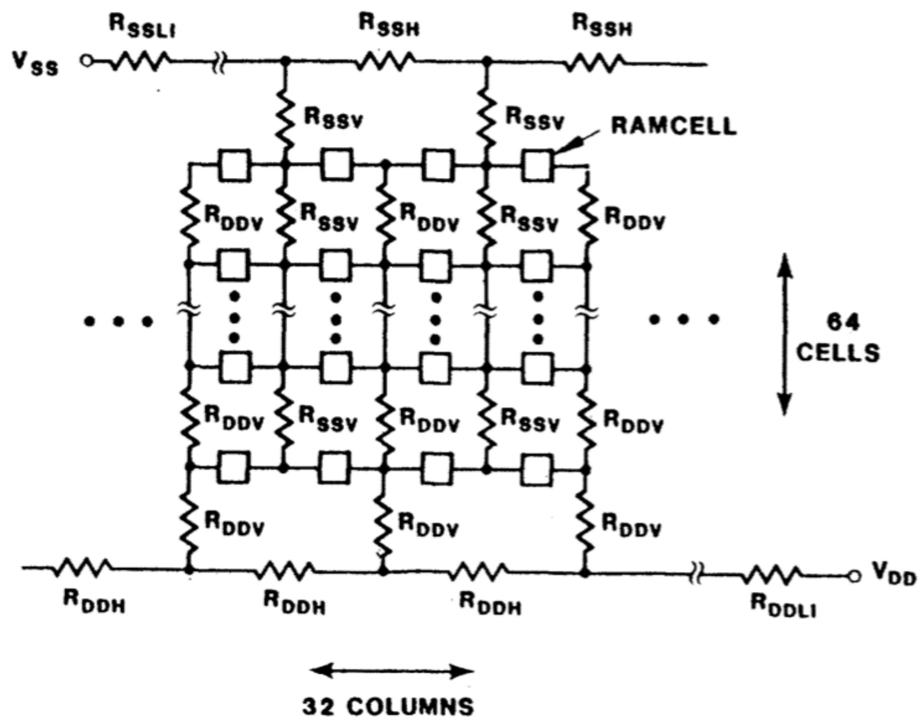

Figure 2.27 Schematic representation of the power distribution with the SRAM cells shown as "black boxes" [98].

SRAM cells furthest from the V_{SS} supply lines [98–100].

Ultimately, it is the SRAM cells furthest from the V_{SS} supply lines that are most sensitive under transient irradiation conditions. This can be seen in Figure 2.28 where the lower left corner of the presented bit-map corresponds to SRAM bit locations furtherest from the the V_{SS} supply line. The SRAM test chips were exposed to dose-rates of 1.02×10^9, 1.08×10^9, and 1.16×10^9 rad(Si)/sec. The increased density of bit-errors near the lower-left corner of the test chip indicates that railspan collapse is the dominant mechanism contributing to upsets under these experimental conditions. It is important to note that the dose-rates used in transient radiation experiments (on the order of Grad(Si)/sec) are *extremely* high and do not represent typical dose-rates in either the space radiation or terrestrial environments (outside of the specific environments mentioned previously). The signature of errors corresponding to railspan collapse, clusters of errors far from the V_{SS} supply line, is useful for identifying the physical mechanism contributing to errors in SRAM experiments.

2.4 Radiation Environments

Understanding the sources of ionizing radiation and modeling fluctuations in the concentration and flux of particle species is essential for accurately predicting error rates in modern electronics in the space radiation environment. Table 2.1 shows some important characteristics for the predominant particle species present in some of the common space radiation environments. Each of these environments has unique signature in terms of the species, the energy, and the flux of those particles present. Consequently, the presence of radiation in each environment has specific implications for electronics unique to those environments. The CREME96 [101] and CRÈME-MC [102,103] codes exist as a means to provide critical information regarding the effects of the environment shown in Table 2.1 on the electronics. The use of these codes provides

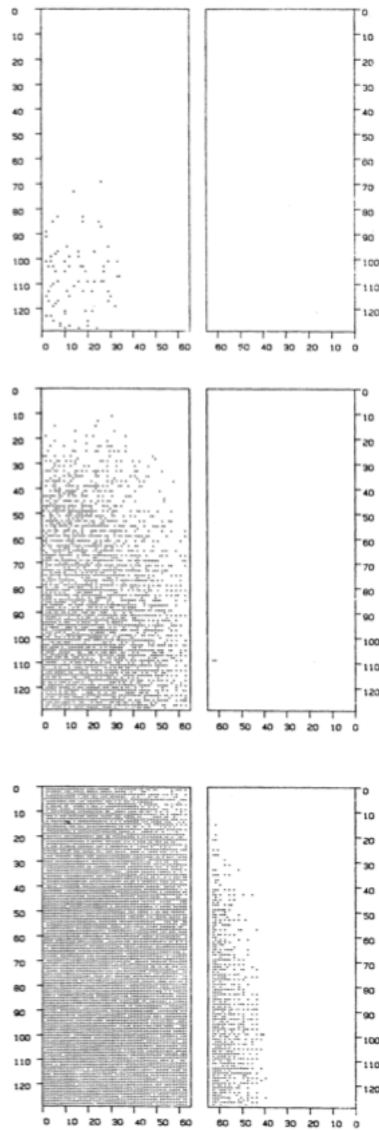

Figure 2.28 Upset bit-map with no pre-test total dose for (a) 1.02×10^9,(b)1.08×10^9 and (c)1.16×10^9 rad(Si)/sec.

a rudimentary framework for evaluating the potential risk of flying certain types of microelectronics in the different environments. The following section addresses the particle species present in each environment and their impact on electronic systems.

Table 2.1 Particle Radiations in Near-Earth Orbit and Some Properties [4]

Radiation	Maximum Energy	Maximum Flux	Radiation Effects	Shielding Effectiveness
Earth Trapped Protons	500 MeV	10^5 cm^{-2} s^{-1}	TID, DD, SEE	Moderate
Earth Trapped Electrons	10 MeV	10^6 cm^{-2} s^{-1}	TID, DD, ESD	High
Jovian Trapped Electrons	100 MeV	10^9 cm^{-2} s^{-1}	TID, DD, ESD	High
Galactic Cosmic Rays	10^{11} GeV	10 cm^{-2} s^{-1}	SEE	Low
Solar Particle Events	10 GeV/n	10^5 cm^{-2} s^{-1}	TID, DD, SEE	Moderate

2.4.1 Solar Particle Environment

Solar-particle events result in the ejection of large quantity of relatively low energy charged emitted from the sun into interplanetary space. There are two types of

solar particle events: solar flares and coronal mass ejections (CME), each of which have distinct signatures and release energetic particles. Solar flares occur when the localized energy storage in the coronal magnetic field becomes too great and causes a burst of energy to be released [4]. The release of energy accelerates charged particles away from the sun into space. Such events tend to last for hours and emit a large measure of charged particles. The particle species present are electron rich, though protons and helium ions are also present in solar flares [104]. A CME is a release of plasma, consisting of free electrons and ions, the shock wave accelerates particles outward into interplanetary space. CMEs tend to be proton rich and last for several days. The dominant interaction mechanisms of electronics with particles in the solar particle environment are TID, displacement damage, and SEEs. Of the two types of solar particle events, CMEs are responsible for major disruptions in interplanetary space and large scale geomagnetic disturbances on earth that can in turn result in disruption of communications and electronics.

All naturally-occuring elements are present in solar particle events at some detectable level of concentration, although they consist primarily ($> 99.9\%$) of solar protons, helium, and electrons. Despite the small composition the presence of heavy ions in the solar particle environment is a non-negligible population of particle species, particularly when evaluating the impact of radiation on electronics. Solar particle events have been observed to vary over time with predictable intervals where activity levels are at a minimum and maximum. A plot of daily solar proton fluence can be seen in Figure 2.29. The CREME96 models were adapted to account for variations in solar activity and provide accurate representation of particle fluxes present in the near-earth environment. Figure 2.30 shows the particle flux spectra from CREME96 for a geosynchronous orbit during “worst-day” conditions with 100 mils of aluminum shielding [101]. Particle energies in solar flares and CME events may

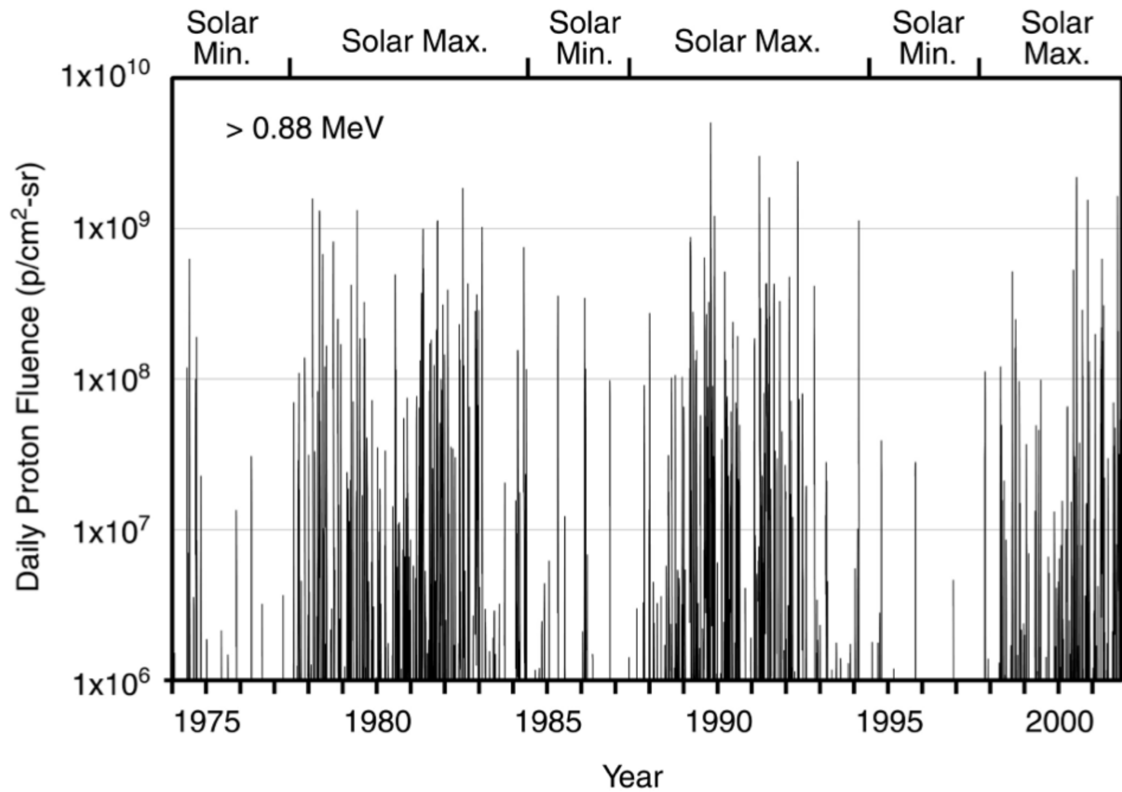

Figure 2.29 Daily fluences of > 0.88 MeV protons due to solar particle events between approximately 1974 and 2002 [104].

approach 1 GeV/u with peak fluxes higher than 10^5 cm^{-2} s^{-1}.

2.4.2 Galactic Cosmic Rays

Galactic cosmic rays (GCR) are high-energy particles, primarily hadrons, that originate from outside our solar system. These energetic, charged particles are stripped of electrons by the interstellar medium and accelerated to high energies. The primary concern for microelectronic systems exposed to the GCR environment are SEEs.

A basic description of the GCR environment is given in Table 2.1. All naturally occurring elements are present in the GCR environment up to uranium. The particle spectrum is represented by approximately 90% protons, 9% helium, while heavier elements from lithium through iron and nickel make up the remaining 1% of particle

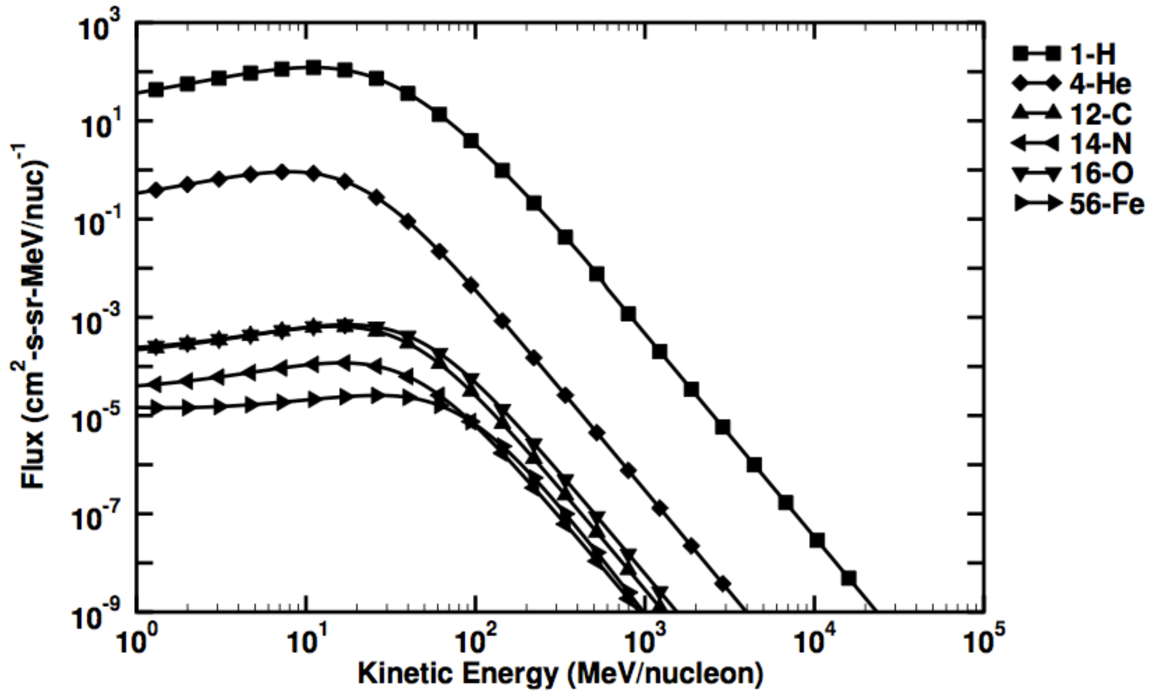

Figure 2.30 The particle flux spectra computed by CREME96 for a Near-Earth Interplanetary or Geosynchronous orbit during the worst day scenario with 100 mils of aluminum shielding. Common species shown, all others omitted [21].

species. A large decrease in abundance occurs for atomic numbers higher than iron, this feature of the GCR spectrum is known as the "iron knee". The relative abundance of elements through Z=28 is shown in Figure 2.31.

The local interstellar medium is a relativity constant, isotropic flux at the helio-sphere boundary. The presence of a magnetic field from the sun impedes the flux of low-energy (<20 MeV/u) particles in the GCR spectrum entering the solar system. Additionally, the solar wind modulates the flux of particles from the GCR in regions of interplanetary space. Consequently, increased solar activity levels result in a lower flux of particles emanating from the GCR environment and lower solar activity levels result in an increase in the GCR flux in interplanetary space [105,106]. The impact of solar activity on the differential energy spectra of common elements in the GCR envi-

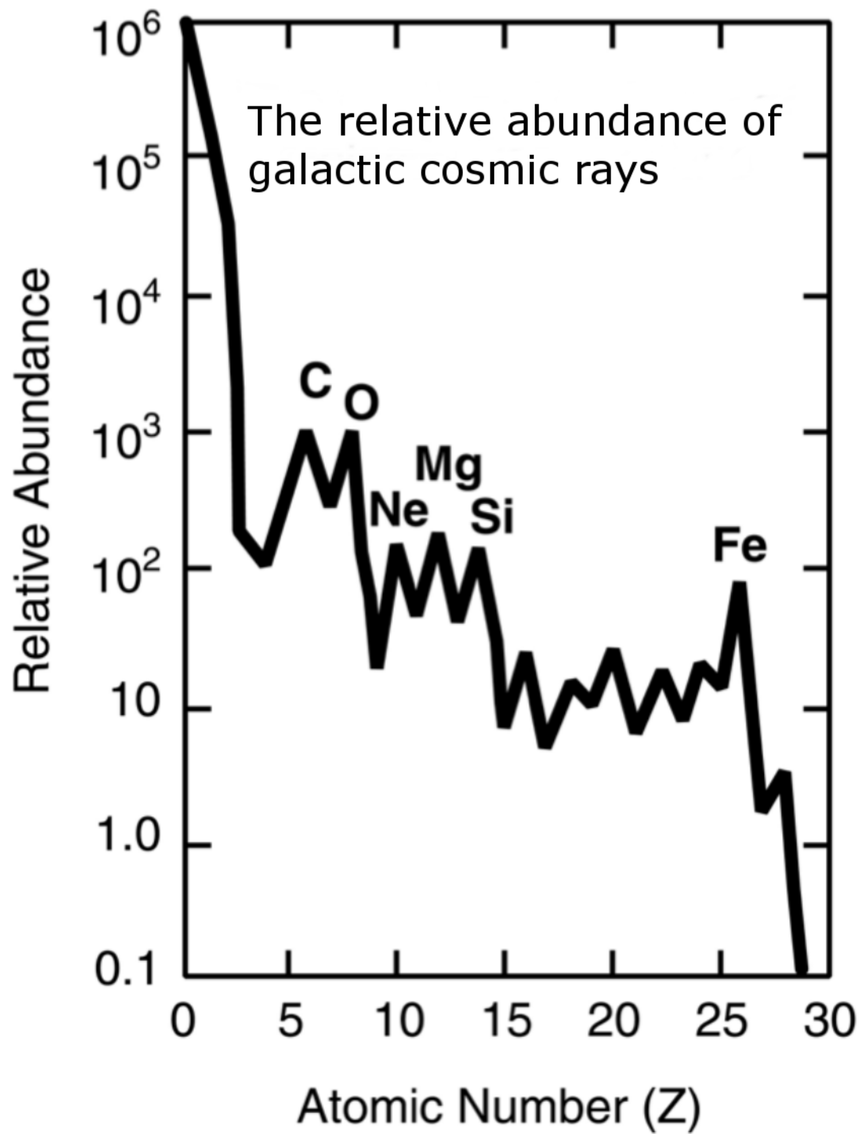

Figure 2.31 Abundances of particles species in the GCR spectrum up through Z = 28 [104].

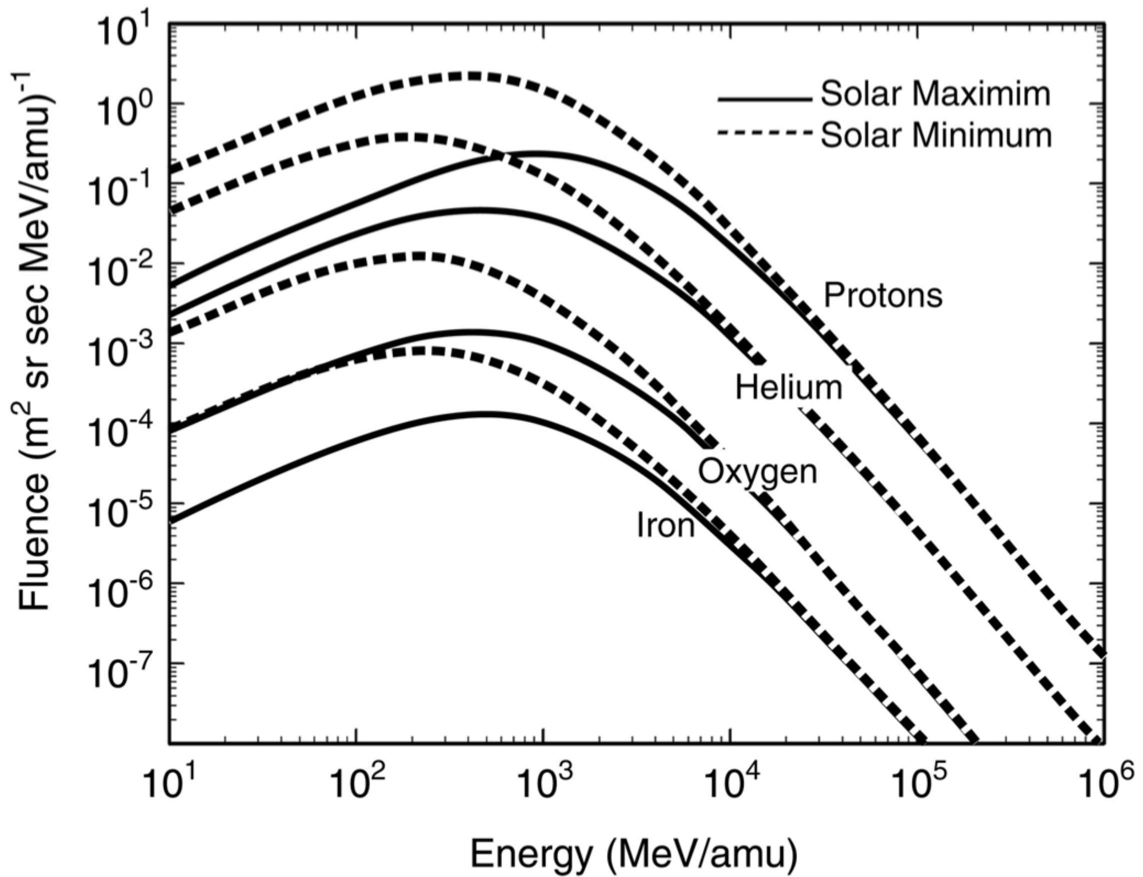

Figure 2.32 GCR energy spectra for protons, helium, oxygen and iron during solar maximum and solar minimum conditions [107].

ronment is shown in Figure 2.32. Together, the combination of solar particles and the GCR environment make up the interplanetary radiation environment. The region of consideration for particles originating from these sources ranges from geosynchronous orbits to the free space between planetary systems.

The CREME96 and CRÈME-MC tools represent efforts attempting to provide a reliable framework for analyzing the susceptibility of modern electronics to particles from the GCR environment. These codes provide a consistent metric for analyzing the flux and LET of particles exposed to the GCR environment and provide a means of analysis for estimating error/event rates.

2.4.3 Trapped Particle Environments

Energetic charged particles are captured by and present around planets with significant magnetic fields. Orbiting satellites, manned, and robotic space exploration missions encounter the trapped particle environment for the extent of the mission lifetime. The near-Earth radiation environment is of primary importance for orbiting communications, weather, GPS, defense, and scientific satellites. The near-Earth environment also has significance due to the presence of the international space station where mission criteria must also consider the biological and electronic impact of radiation on systems and the human presence on the ISS.

The Jovian environment is of interest to scientists and researchers interested in looking at geological processes on several of the moons. To date, NASA has planned several future missions that send remote sensing satellite probes to the Jovian environment to investigate its moons, Io and Europa, in addition to studies of Jupiter itself. The trapped particle environment around Jupiter is difficult from a mission reliability perspective due to the presence of high-flux, high-energy charged particles trapped in the planet's magnetosphere.

The following discussion focuses on the near-Earth environment and Jovian environment.

Earth Radiation Belts

The Earth's magnetic field acts as a barrier to electromagnetic radiation but also acts to trap charged particles in stable orbits around the planet. The regions where charged particles can be found around the planet are known as radiation belts. The particles populating the radiation fields surrounding the Earth originate from solar particle events and the GCR environment, although for some time a high altitude nuclear

weapons test referred to as operation Starfish Prime did introduce and modify the particle species and structure of the radiation belts. The discovery of the radiation belts surrounding Earth is credited to Van Allen who performed the initial analysis of data identifying the particle populations and mapping their intensities [108]. Since their discovery, additional studies of the trapped particle environments surrounding Earth have been performed, identifying the particle species present, flux, and variation in particle population based on solar and military activities [109,110]. The initial AE-8 and AP-8 models allowed designers to account for TID, SEE, DD, and ESD effects. As electronics have become increasingly sensitive to ionizing particle events employing the use of the AE-8 and AP-8 models has also increased in difficulty. Efforts continue to refine the trapped particle environment models to account for sources of error and uncertainty and much progress has been made for the AE-9 and AP-9 models [3,4,111].

A basic description of common particles found in the trapped particle environment can be seen in Table 2.1. Trapped electrons, protons, and alpha particles are the majority particle populations, making up greater than 99.9% of particle species [104]. These particles are separated into two regions, an inner and outer radiation belt, with a "lower" flux slot region between. Contour plots of the particle populations for electrons and protons can be seen in Figures 2.33 and 2.34, respectively.

Trapped electrons around the Earth vary in energy from 10 keV to 10 MeV and are associated with TID, DD, and ESD/charging effects in electronic systems. The differential flux of electrons as a function of time is shown in Figure 2.35. Figure 2.35 shows that for low-energy electrons (<1 MeV) electron flux at geostationary orbits have been relatively constant over time and do not vary significantly with solar activity. This is not the case for high-energy(>1 MeV) electrons, which vary as a function of time and solar activity. Trapped electrons and protons exhibit two high-flux re-

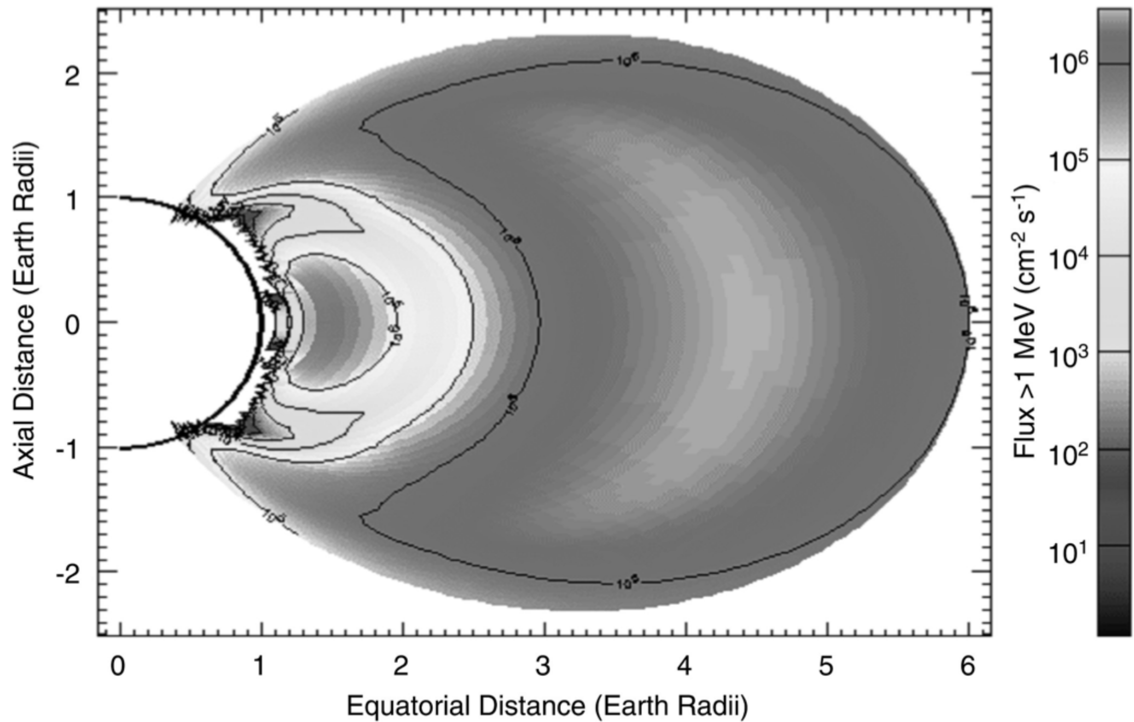

Figure 2.33 The electron population with energies > 1 MeV as predicted by the AE-8 model for solar maximum conditions [104].

gions, an inner and outer radiation belt, separated by a low flux slot region. The inner radiation belts, for both electrons and protons, remain relatively stable and do not vary with increased solar activity. These inner regions contain the low to intermediate energy spectrum of electrons and protons. This is not true for the slot regions, where variation in solar activity may modulate the flux of particles by several orders of magnitude hour to hour and day to day. The outer radiation belts exhibit a more significant dependence on solar activity varying in both energy and flux by several orders of magnitude day to day.

Shielding has been used to great effect for electron environments near earth and in interplanetary space. Only electrons with energy greater than 1 MeV are capable of transporting through 100 mils of aluminum and interacting with microelectronic

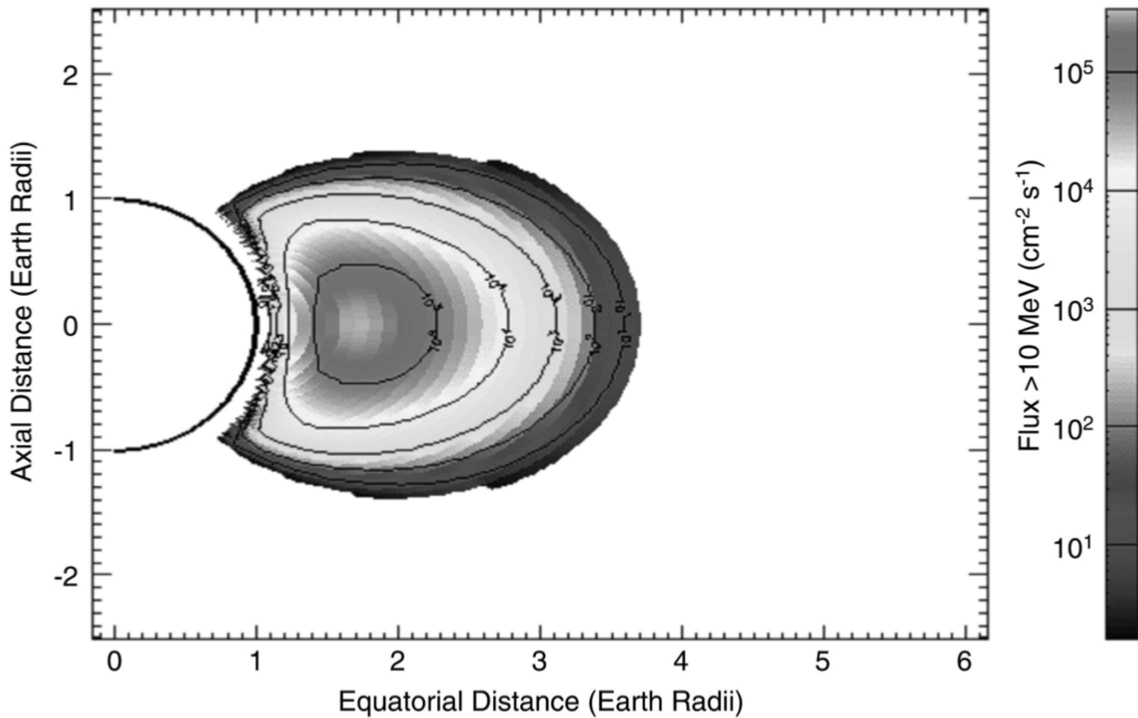

Figure 2.34 The trapped proton population with energies > 10 MeV as predicted by the AP-8 model for solar maximum conditions [104].

systems. In geostationary orbits, 100 mils of aluminum shielding provides complete protection for electronic systems against TID and DD as little of the trapped electron environment is capable of transporting through the shielding and impacting nominal system operation.

Jovian Electron Environment

Similar to that of Earth, Jupiter also exhibits a strong magnetic field surrounding the planet and has stable charged particle populations. The energy associated with trapped electrons surrounding Jupiter is much greater than that of Earth [113, 114]. The Jovian electron environment has been well studied by the galileo interim radiation electron (GIRE) model published by NASA–JPL [113]. Additional efforts have extended the original GIRE model to a maximum energy of several hundred

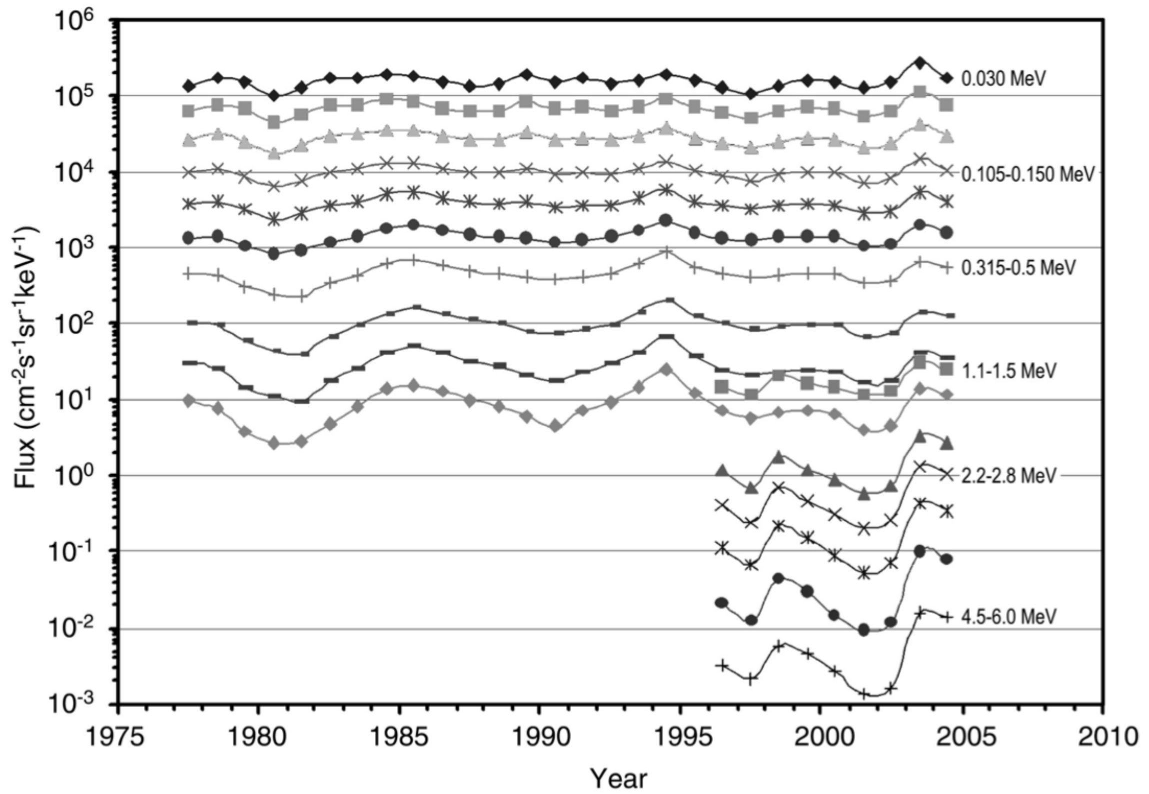

Figure 2.35 Time and energy dependence of the mean electron flux at geostationary altitudes over about 2.5 solar cycles [112].

MeV and a maximum radius of 50 Jovian radii [115, 116]. The current version of the model, denoted as GIRE2, describes the omnidirectional flux of energetic electrons in the Jovian equatorial plane at distances large enough to extrapolate information for planned NASA missions to study the Jovian moons.

The differential flux spectrum as a function of distance, given in Jovian radii, is shown in Figure 2.36 with line plots indicating the flux of electrons of a given energy. The energy spectrum of trapped electrons in the Jovian environment ranges from approximately 10 keV to 100 MeV. Similar to the trapped electron environment around Earth, there is significant variation in the estimated electron flux for high-energy (>10 MeV) with increasing distance. Differences in the inner and outer radiation

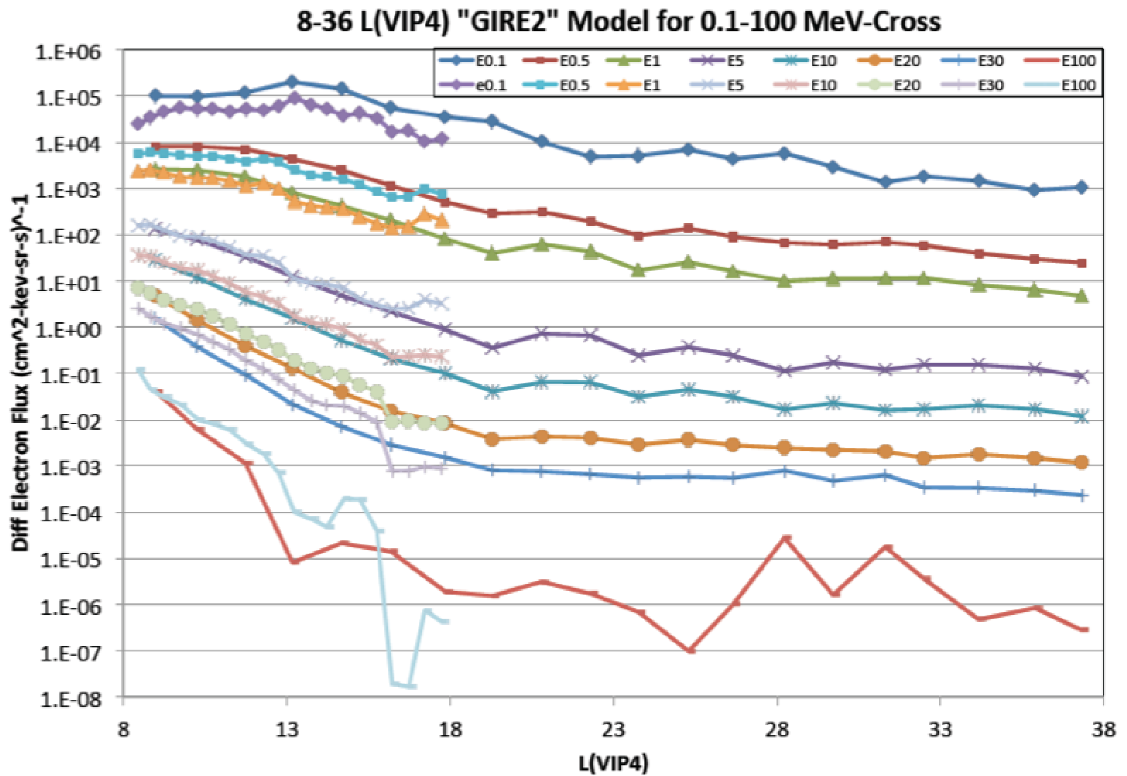

Figure 2.36 Line plots of the differential electron fluxes as predicted by the inner region GIRE and GIRE2 models [114].

belts are due to distinct characteristics of the magnetic field surrounding Jupiter and are influenced by fluctuations in solar activity [114]. Differential flux spectrum for electrons in the Jovian and Europa environment phase of the Juno spacecraft mission to the Jupiter planetary system can be seen in Figure 2.37. In the different phases of the Juno spacecraft tour of the Jupiter planetary system, onboard electronics are exposed to a range of highly-energetic, high-flux electrons. The 120 day tour of Europa alone results in a significant increase in the flux of electrons with energy higher than 20 MeV, which may have a significant impact on SEU event rates. The use of 100 mils of aluminum shielding may provide protection for spacecraft electronic systems for the high flux of electrons below 1 MeV. However, the flux of high-energy electrons is a potential serious threat for mission reliability.

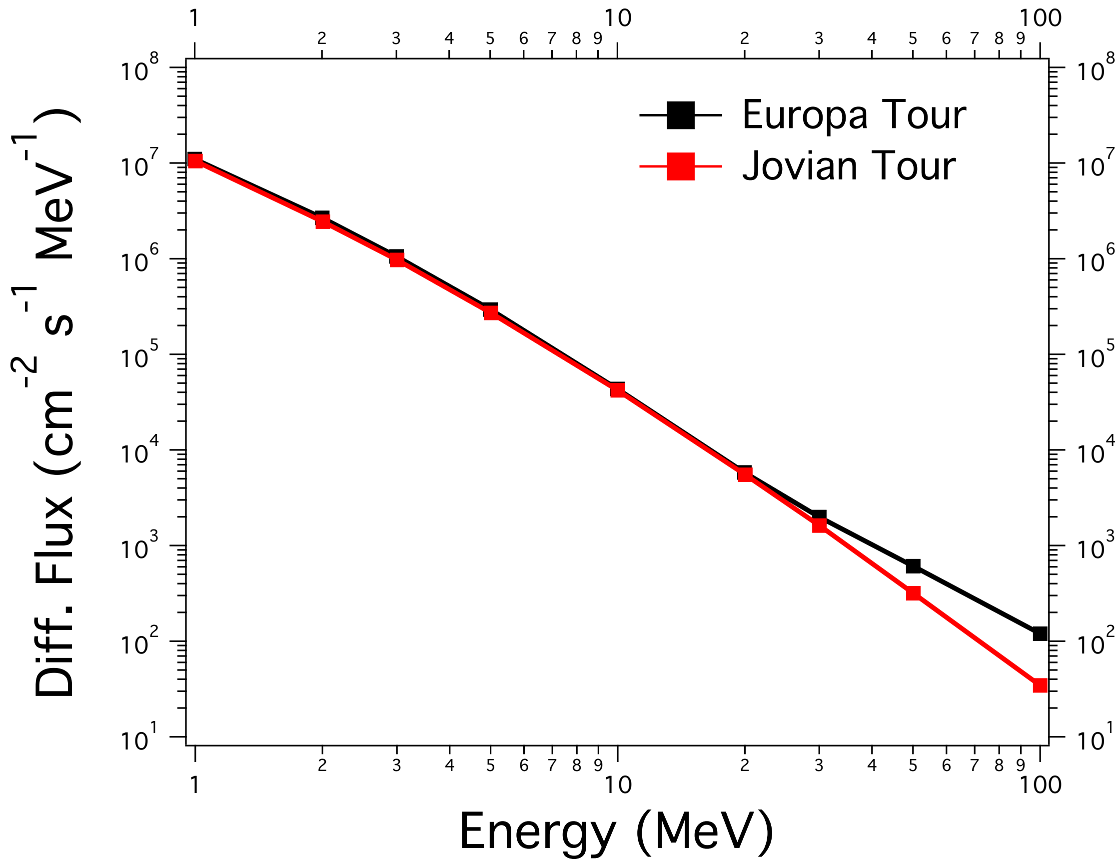

Figure 2.37 Differential flux spectrum for electrons in the Jovian and Europa environment phase of the Juno spacecraft mission to the Jupiter planetary system.

2.5 Ionizing Particle Track Structure

Work by Kobetich [117] and Katz [118] provided early understanding of ionization track structure in matter by modeling the range and stopping power of δ-rays. The Katz model represents the average energy deposited within a volume as a function of radial distance from an ion trajectory [117–120]. Energy deposition occurs in regions surrounding an incident ion trajectory due to the scattering of δ-rays, which results in spatially non-uniform, highly-localized energy deposition events.

In [119], Zhang formulates an analytical expression of the dose deposited in the

Katz model as a function of radial distance t,

$$D(t) = \frac{Ne^4 Z^{*2}}{\alpha m_e c^2 \beta^2 t} \frac{(1 - \frac{t-\theta}{T+\theta})^{1/\alpha}}{T + \theta} \tag{2.11}$$

where N is the electron density, e is elementary charge, m_e is the electron mass, Z^* is the effective charge state of the incident particle with relative velocity β, c is the speed of light in vacuum, T is the range of δ-rays with energy W, θ is the range of δ-rays with kinetic energy equal to the ionization potential I, and α is a fitting parameter as defined in [32, 119, 120].

Figure 2.38 shows the radial dose profile in emulsion for several incident ion energies [117, 118, 121]. The radial extension of the ionization track structure depends on the energy of the incident ion due to the kinematics of δ-ray generation and their range. For small values of incident ion energy, Figure 2.38 shows the radial dose deposited is larger near the core of the ion track. As β increases, Figure 2.38 shows that the dose near the ion track core decreases, while the corresponding maximum radial distance energy is deposited increases.

The kinematics of δ-ray generation limit the maximum energy transferable in a collision between an incident ion and a single electron. This limitation on energy transfer restricts a δ-ray's transport range within the target material. The expression for maximum energy transfer, W, is given by

$$W = 2m_e c^2 \gamma^2 \beta^2 \tag{2.12}$$

where m_e is the rest mass of an electron, c is the speed of light, β is the relative velocity of the incident ion, and γ is the Lorentz factor (defined as $(1 - \beta^2)^{-1/2}$). Equation (2.12) is valid for the case $\gamma m_e / M_{ion} \ll 1$, where M_{ion} is the mass of the incident ion. Equation (2.12) scales monotonically with incident ion energy; this implies that for high-energy particles, generated δ-rays may transport far from their

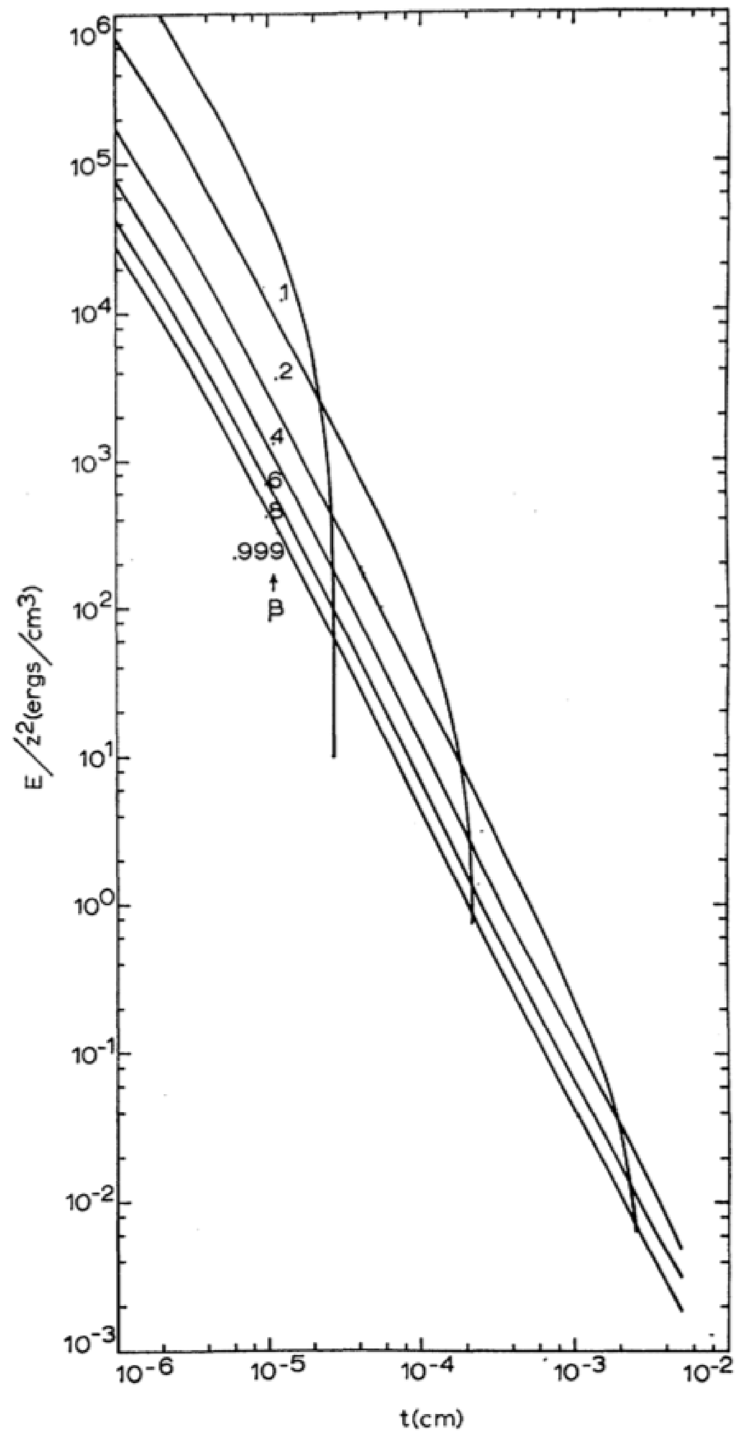

Figure 2.38 The spatial distribution of ionization energy in emulsion for incident particles with differing relative velocity [117, 118, 121]. These calculations, based on Katz theory, describe the average dose deposited as a function of radial distance, t, from the incident ion track.

point of generation. As the incident ion loses energy, the track radius decreases, forming a conical shape as a function of distance into the target material [30].

In 1988, Stapor *et al.* described how two particles with similar LETs would have differing charge generation profiles, and therefore the possibility for differing SEU responses [30]. In Figure 2.39, *e-h* pair density is plotted as a function of radial distance from the ion trajectory at a depth of 1 μm in silicon. Figure 2.39 illustrates the difference in the resulting charge generation profiles for two ions with similar LETs but differing energies [30]. While the LET of a 25 MeV and 395 MeV Cu ion is the same, the resulting charge generation profiles differ, with the less energetic particle having a dense charge generation region around the core of the ion trajectory, and the more energetic ion having a greater radial extension from the incident ion trajectory. As the incident particle loses energy, the maximum energy of generated δ-rays also decreases, causing the ion track radius to decrease with increasing penetration depth into the material.

In 1992, Xapsos [122] outlined a statistical framework for the application of LET to microelectronics that considered the track structure of an incident ion. This established a metric for determining the validity of LET for technology nodes with well-established sensitive volume geometries. Dodd *et al.* [33] published measurements six years later showing the LET metric was sufficient to characterize CMOS technology nodes larger than 250 nm. In [33], Dodd demonstrated that for older technology nodes that exhibit a critical charge greater than 10 fC the LET of the primary particle is sufficient to predict the device- and circuit-level response.

More recently, interest has reemerged in evaluating the potential contribution of electrons and δ-rays to the SEU response of modern technology nodes. Murat *et al.* evaluated technology nodes with feature sizes less than 0.5 μm, determining that the energy of the incident ion does contribute to the SEU response [123]. Later, King

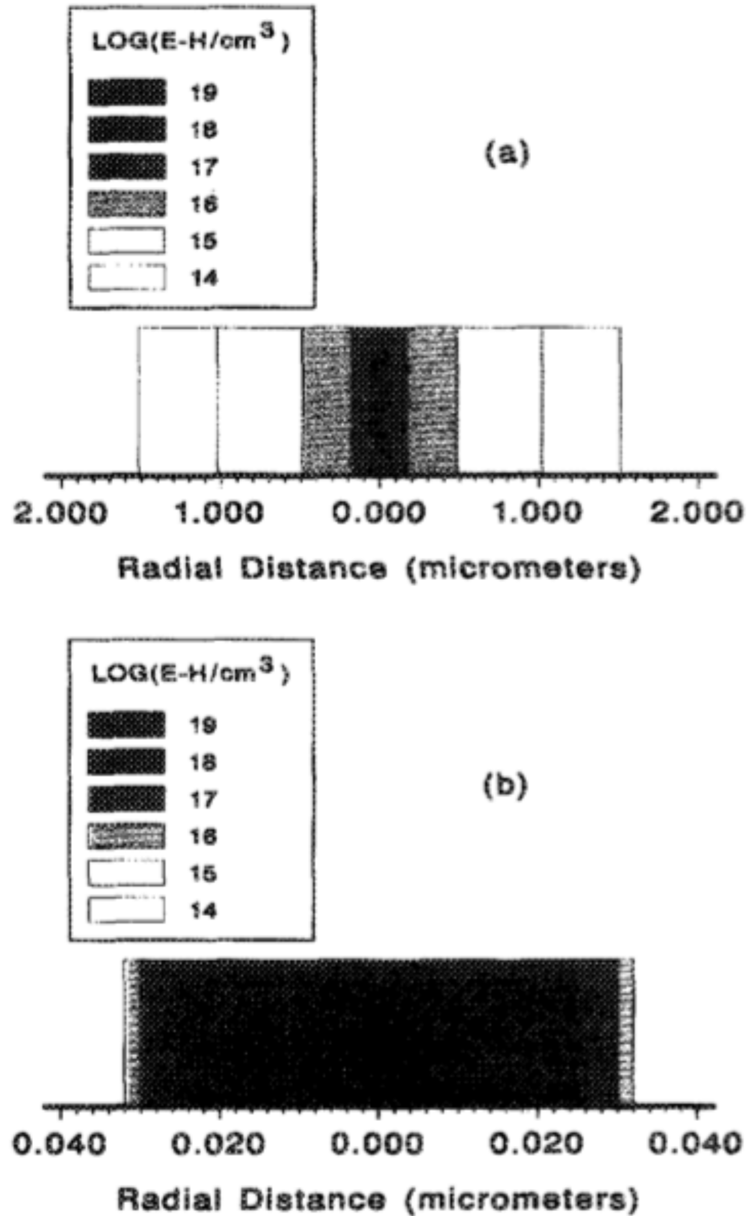

Figure 2.39 Calculated *e-h* pair density generation is shown as a function of radial distance from the ion track at a depth of 1 μm within a volume of silicon for (a) 395 MeV Cu and (b) 25 MeV Cu [30].

et al. demonstrated the potential for contributions to the SEU cross section from individual δ-rays depositing energy within the sensitive volume of a 22 nm SRAM [9]. Raine *et al.* published several papers utilizing the Katz model to evaluate energy deposition contributions from δ-rays in a single ionizing particle event to the SEU rate. These studies concluded that the ionization profile of heavy ions does not contribute to multiple-bit upsets in the 32 nm SOI technology node [7]. However, it has been shown that while the average energy deposition profile is modeled well by the Katz model, variation between the average and individual δ-ray energy deposition events can be quite significant [10].

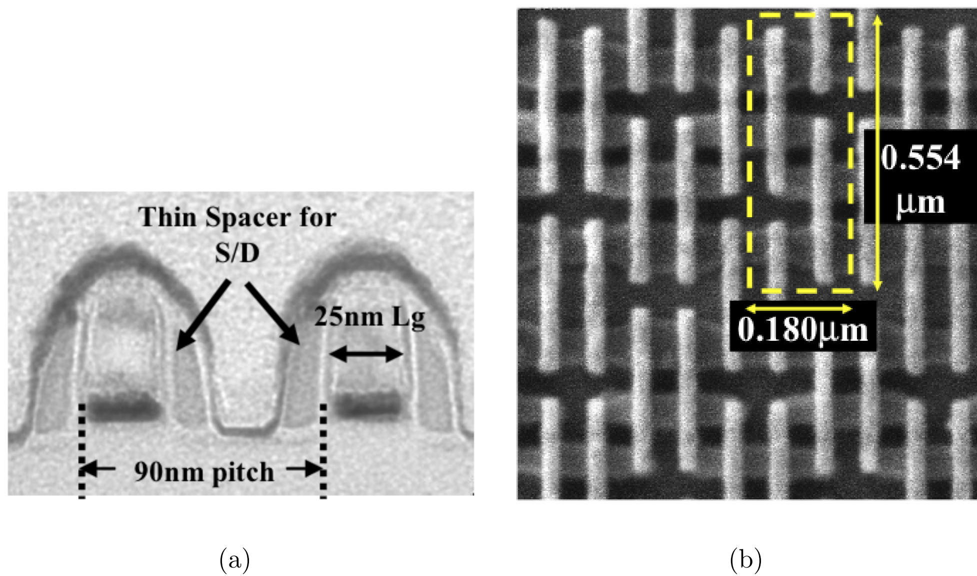

Figure 2.40 2.40(a) Cross-sectional TEM image showing thin composite oxide-nitride spacer on 25 nm wide gate at 90 nm pitch. 2.40(b) Top-down SEM image of the 0.1 μm^2 6T-SRAM cell after STI fill and gate-first metal gate patterning, with cell dimensions of 0.18 μm and 0.554 μm. After [53].

The track radius of ionizing radiation events is large compared to the spacing of adjacent transistors and pitch of neighboring SRAM cells in a 22 nm technology node, shown in Figure 2.40. This implies that modern technology nodes have scaled to a point where δ-ray energy deposition events may be of sufficient magnitude and

interact frequently enough to become a reliability concern. This leads to the potential for contributions to the single- and multiple-bit upset event rate from the primary ion and δ-rays generated in ionizing particle events. Consequently, for technologies that exhibit critical charges lower than 0.2 fC, the role of δ-rays must be reconsidered when evaluating the SEU response of SRAM fabricated in these technology nodes [9, 10]. It is therefore necessary to have a thorough understanding of the effects of δ-rays on these devices in order to understand the SEU response of SRAMs fabricated in technology nodes that exhibit small critical charge. These issues are discussed in detail in Chapter 4.3, which focuses on the impact of incident ion species, energy, mass, and the implications of δ-rays interactions on the SEU response of current- and next-generation technology nodes.

Chapter 3

Experimental Investigation of Electron-Induced SEUs

This chapter presents experimental methods for *in situ* X-ray irradiation and SEU measurements as a technique for investigating electron-induced SEUs in SRAMs. Extensive parametric and functionality testing of SRAM test chips fabricated in 28 nm and 45 nm bulk silicon technology was performed to determine the range of operational stability. SRAM test chips were shown to be stable and hold valid data over a wide range of supply voltage conditions. Test boards were designed and integrated to allow independent, simultaneous control of the SRAM test chips and power supply conditions during the experiment. Test chips were exposed to a source of energetic X-rays from an ARACOR 4100 X-ray irradiator. SRAMs were programmed into either an all zero (*0000*), all one (*1111*), checkerboard (*1010*), or reverse checkerboard (*0101*) pattern during irradiation. Once exposure of the SRAM test chip to X-rays was complete, the final state of the data pattern was read back and compared to the initial, programmed, state. The data pattern and address location of any errors was logged and recorded for further analysis. Section 3.1 discusses the relevant experimental setup and methods. Section 3.2 provides a full discussion of the experimental results and analyzes critical experimental parameters. Section 3.3 compares the supply voltage dependence of X-ray SEU probabilities to similar data obtained in muon and low-energy proton irradiations.

3.1 Experimental Setup and Methods

A diagram of the experimental setup used to investigate electron-induced SEUs using an X-ray source is shown in Figure 3.1. An automated test system was developed to allow independent control of two Keithley 2410 SourceMeters® for the SRAM test chip and SRAM test board through a GPIB/LAN gateway while sending control commands to the SRAM test board through a USB connection. This configuration allows remote control of the SRAM supply voltage and allows the power supply current to be monitored while performing parametric testing of the SRAM test chip.

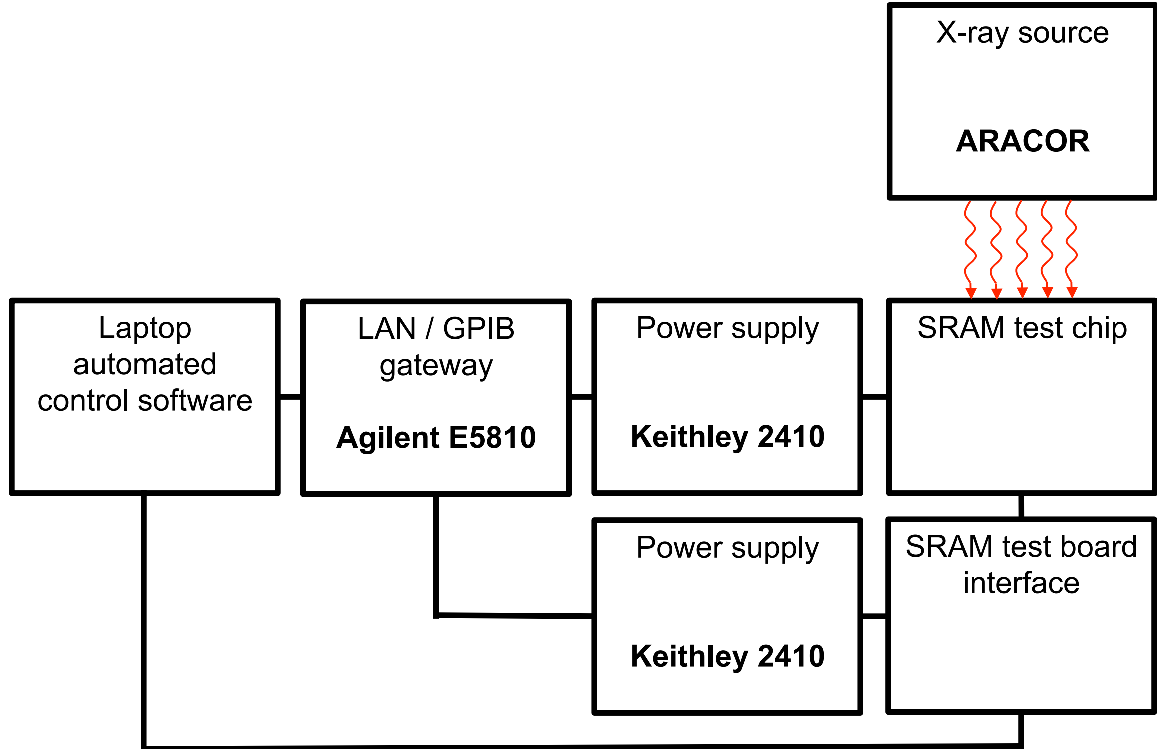

Figure 3.1 An automated test system allows independent control of two Keithley 2410 SourceMeters for the SRAM test chip and test board interface through a LAN/GPIB gateway. Control commands are transmitted to the SRAM test board through a USB connection from a laptop. This system allows the supply voltage of the SRAM to be modulated *in situ*. The device under test is exposed to energetic X-rays under varied supply voltage conditions.

Reduced supply voltage conditions are employed to determine the susceptibility of the SRAM to singly-charged particles and compare the bias dependence of electron-induced upset rates to that of upsets known to be caused by low-energy protons and muons [1, 2]. As discussed in Section 2.2, low-voltage operation has practical significance, since it is common for SRAMs in standby mode to operate at 70-80% of the nominal supply voltage to reduce power consumption [51, 52]. Low-power applications, mobile communications, mobile computing, and medical devices also frequently employ power-saving techniques that include reducing V_{DD} during standby and idle modes of operation, making this a relevant testing approach.

Figure 3.2 shows the applied bias as a function of time for a representative testing sequence employed in this study. An initial write and read, using either an all one, all zero, checkerboard or reverse checkerboard pattern, is performed at nominal bias conditions prior to X-ray exposure of the device under test (DUT). The supply voltage is then lowered while the DUT is irradiated. In the case of Figure 3.2, the total exposure time was 30 seconds. In other experiments the total exposure time was varied from 30 seconds to several minutes. Once the X-ray source was turned off, the supply voltage was returned to nominal conditions and the final state of the memory was read. The final and initial states of the memory were compared to identify any errors that may have occurred, noting the address and data patterns of observed errors for post-processing.

During the experimental period the range of supply voltages used in this study varies from 0.35-1.0 V. The SRAM test chips used in this work are commercial parts *designed* to operate and remain stable between 0.5-1.0 V. In functionality and parametric bench testing, the test chips were confirmed to be stable down to 0.35 V during a one hour testing period, which is much longer than typical X-ray exposure times in these experiments. Extensive testing was done prior to irradiation to demon-

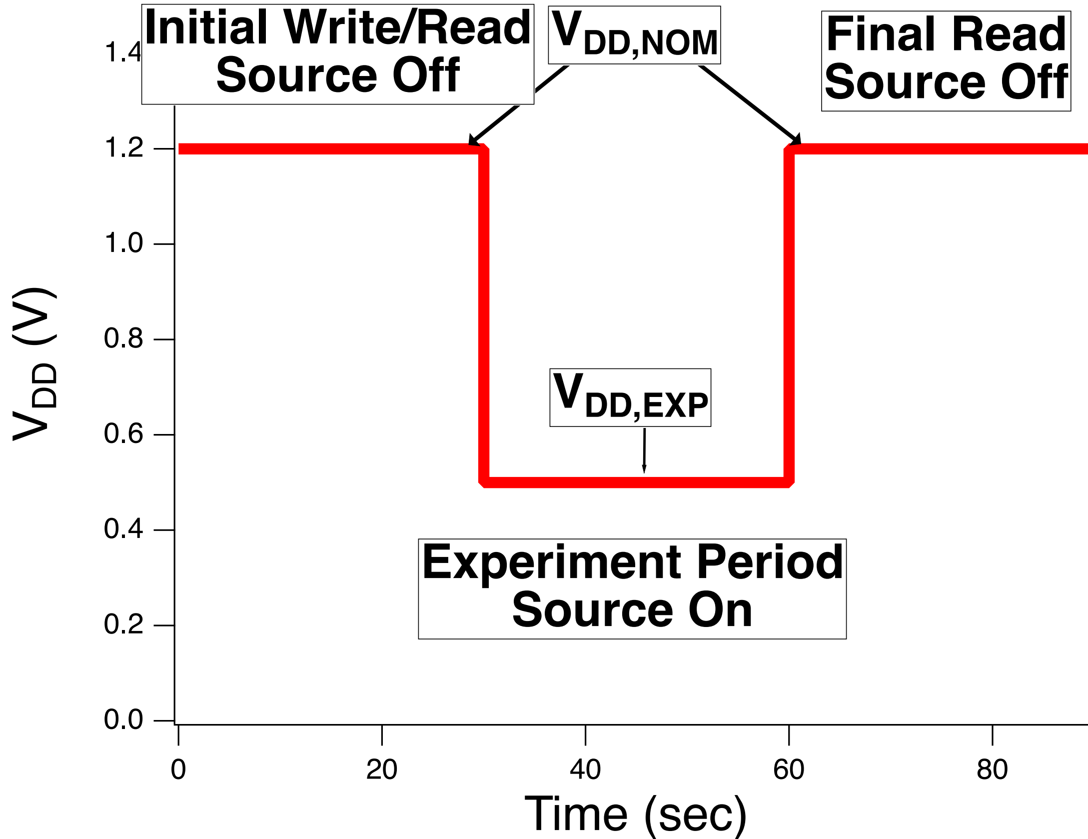

Figure 3.2 Example timing diagram for measuring upsets at reduced bias. Read and write operations are performed under nominal bias condition, V_{DDNOM}. During exposure the rail is reduced to a value, V_{DDEXP}, for the duration of the experiment. Upon conclusion of the exposure, the nominal rail is restored, a final read operation is performed, and any errors recorded.

strate that no bit flips occurred under any bias conditions, indicating the memory was written properly and held valid information through the timing sequence shown in Figure 3.2 and in all other cases shown in this work. Functionality and parametric testing was performed before and after each radiation exposure for equivalent time periods to ensure the integrity of the SRAM under all bias conditions. This procedure verifies that the data remain intact and stable at all supply voltage conditions and that no degradation of the DUT due to TID has occurred during or after each X-ray exposure.

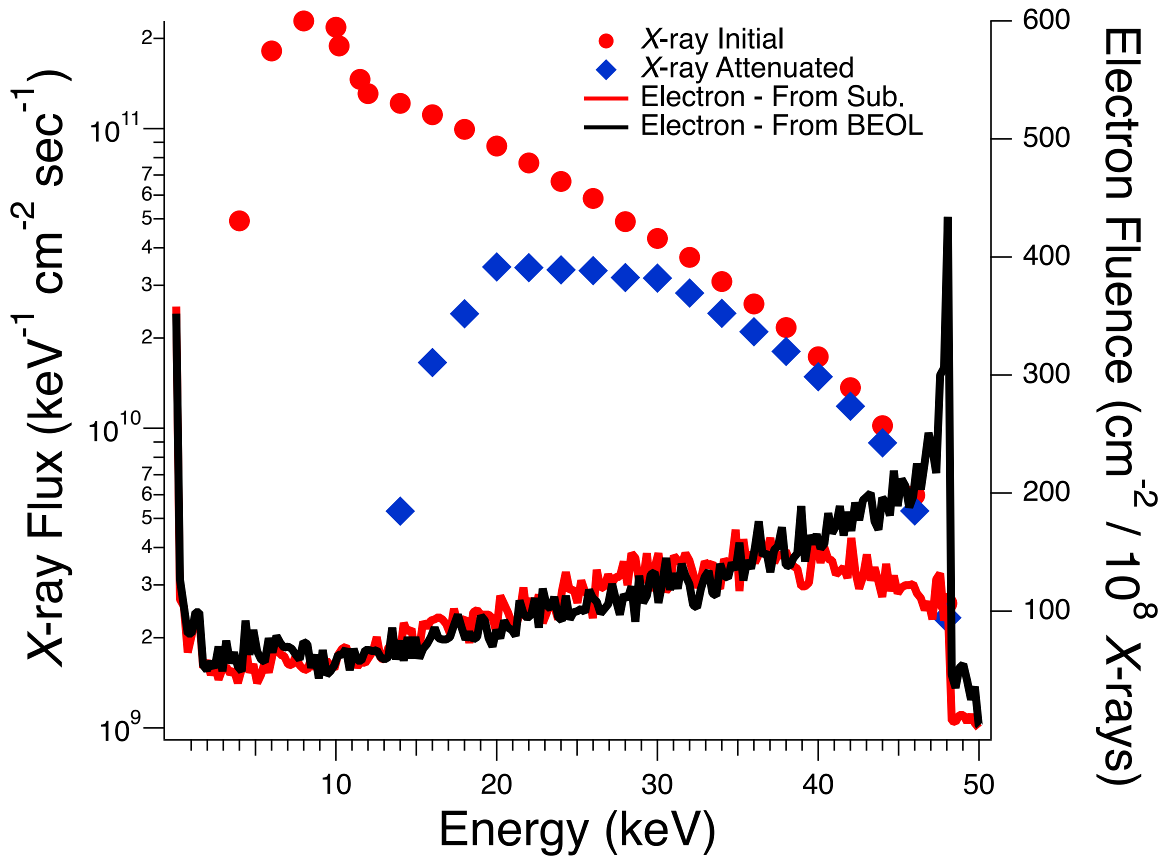

Figure 3.3 X-ray and electron spectra produced by the ARACOR 4100 X-ray irradiator. The average energy is 10 keV and the maximum energy is 50 keV, corresponding to the endpoint bremsstrahlung energy [124,125]. For the error rate testing in this study, the spectrum is modified by a 1 mm aluminum attenuator, which reduces the flux of low-energy X-rays incident onto the DUT. The electron fluences corresponding to monoenergetic 50 keV X-rays interacting with the active silicon region in the "forward" (scattering events in the active device overlayer materials, denoted BEOL) and "reverse" (scattering events in the device substrate) beam directions are shown on the right.

Irradiation was performed with a beam current of 1 mA and beam voltage of 50 kV. The X-ray spectra produced under these conditions are shown in Figure 3.3 [124,125]. For the unattenuated spectrum in Figure 3.3, 10 keV is the average energy and 50 keV is the endpoint bremsstrahlung energy. The interaction between X-rays in this energy range and electrons is dominated by the photoelectric effect, however, near the bremsstrahlung edge Compton scattering becomes a non-negligible contribution. The generated photo-electrons in these interactions are emitted omnidirectionally. As discussed in Section 2.1.3, for highly energetic photons, where the energy of the incident photon is much greater than the photo-electron shell binding energy ($\hbar\omega \gg E_b$), most of the absorbed photon energy is transferred to the photo-electron.

A 1 mm aluminum attenuator was placed above the DUT with an air gap of 3.5 cm between the attenuator and the test chip. The attenuator filters the low-energy X-ray spectrum, passing the more energetic X-rays that are likely to produce observable electron-induced effects. This reduces the dose-rate and TID effects. Attenuation of the initial spectrum by the 1 mm layer of aluminum is calculated using the Beer-Lambert law, Equation 2.8 and plotted in Figure 3.3. The prominent 10 keV X-ray peak is absent from the attenuated spectrum; only the high energy tail of the X-ray distribution is capable of transporting through the attenuator and interacting with the DUT. The majority of photo-electrons generated in the attenuator are reabsorbed before leaving the Al.

MRED [126] was used to evaluate the transport of maximal energy, 50 keV, photo-electrons generated at the Al-to-air interface. Representative electron trajectories from those simulations are shown in Figure 3.4. The Al is on top and the air gap is the large rectangle. The DUT is very thin and on the bottom of the figure. Photo-electrons have random trajectories. The few electrons that transport through the air gap to the DUT stop within the first few micrometers of the back end of line

Figure 3.4 50 keV photo-electrons exiting the aluminum attenuator have insufficient energy to transport through the 3.5 cm air gap and back end of line (BEOL) materials to reach the active silicon. Only photo-electrons generated in the DUT itself can interact with the device material in the sensitive silicon region.

(BEOL) materials (metallization and dielectric layers) [127]. Therefore, only X-rays absorbed within the DUT itself generate photo-electrons that can interact with the target material in the sensitive volume of the device. An example of this type of interaction is shown in Figure 3.5 where the absorption of an incident 10 keV X-ray leads to the generation of an initially free, energetic electron that deposits 9.3 keV of energy when it scatters within the sensitive volume of a 45 nm SRAM.

The electron fluence spectrum corresponding to a monoenergetic beam of 50 keV X-rays in the "forward" and "reverse" beam direction is plotted on the right hand side of Figure 3.3. The most frequent energy corresponds to the incident X-ray energy in the forward direction, which corresponds to photo-electrons generated in the BEOL materials and the active silicon region. In the reverse beam direction, corresponding to electrons generated in the substrate that transport back to the active silicon, the situation is more complicated due to the random trajectory of the generated photo-electrons. This demonstrates the random nature, in energy and trajectory, of the

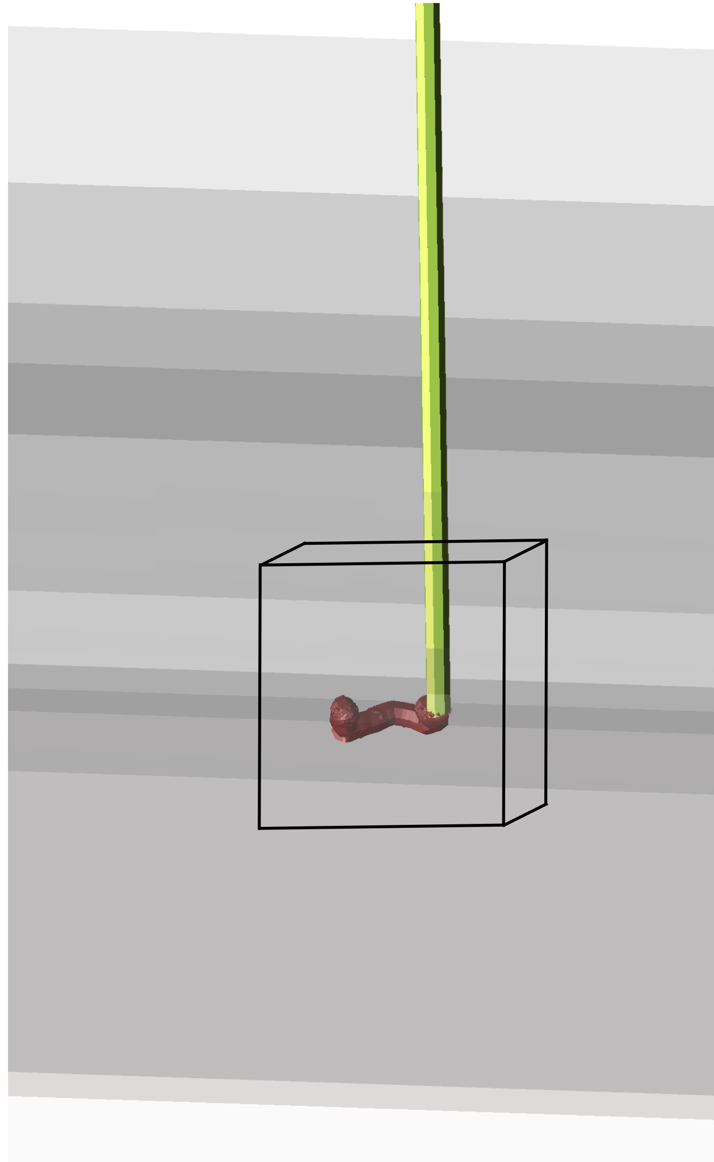

Figure 3.5 A 10 keV X-ray is normally incident on the simulated device structure of a 45 nm SRAM. It subsequently undergoes photoabsorption resulting in the generation of a energetic electron. The resulting electron then transports through the device material, depositing energy in excess of 9.3 keV within the sensitive volume of the SRAM.

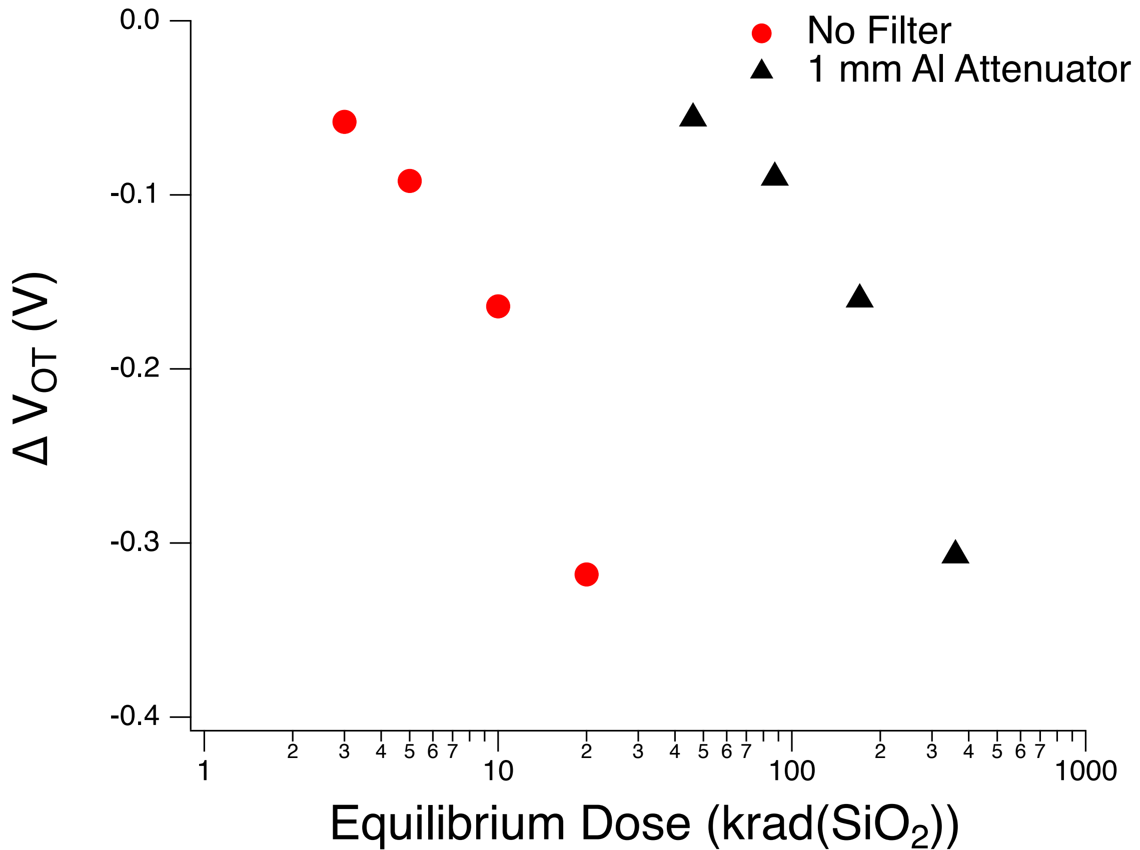

Figure 3.6 ΔV_{OT} as a function of equilibrium dose for MOS capacitors irradiated with beam current and voltage of 1 mA and 50 kV, respectively. Devices were biased with 10 V on the gate during irradiation. The use of a 1 mm Al attenuator causes a increase in equilibrium dose required to achieve equivalent shifts in ΔV_{OT} by a factor of 17, indicating the nominal dose rate of 1.7 krad(SiO_2)/min is reduced to 100 rad(SiO_2)/min.

electron environment local to the sensitive volume.

Following the method used in [125], flatband voltage, V_{FB}, shifts were measured with MOS capacitors to calibrate the dose-rate. The devices were fabricated and packaged at Sandia National Laboratories; lids were removed for the X-ray irradiations. The calibration devices were n-type substrate MOS capacitors featuring aluminum dot gates with an area of 0.01 cm^2 and SiO_2 gate oxide thickness of 101 nm [128]. The dose-rate calibration data are plotted in Figure 3.6, which shows the change in oxide-trapped charge as determined by shifts in C-V characteristics. The equilibrium

dose shown in Figure 3.6 represents the nominal, unattenuated dose from the X-ray source. The measured dose-rate incident on the MOS capacitor is reduced by a factor of 17 when compared to the nominal dose-rate [125]. The attenuated dose-rate is 100 rad(SiO_2)/min.

The X-ray flux is calculated by integrating over the attenuated energy spectrum in Figure 3.3 and can be calculated as

$$\phi_{total} = \sum_{i=0}^{\infty} \phi(E_i) \tag{3.1}$$

where $\phi(E_i)$ is the flux of photons with energy E_i, and ϕ_{total} represents a cumulative photon flux. Evaluating Equation 3.1 with the attenuated photon spectrum yields a cumulative photon flux of 1.5×10^{12} cm^{-2} s^{-1}.

High-energy protons cause single-event effects through secondary ions produced in nuclear reactions [1, 13, 14, 81]. For a given proton energy, experimental cross-sections are expressed with reference to the primary proton flux, regardless of the upset mechanism. In this sense, the case of single-event effects caused by secondary electrons is analogous. Results in this work are therefore plotted as a function of the incident X-ray fluence, which provides the most consistent reference for analyzing SEUs caused by secondary photo-electrons.

3.2 Experimental Results

Using the methods described in Section 3.1, several experiments exposing SRAMs to energetic X-rays were performed to investigate the plausibility of electron-induced upset events. Four types of devices were used. Test Chips A and B are 28 nm SRAMs with a capacity of 23 Mbit and nominal operating voltage of 0.9 V in triple-well (TW) and dual-well (DW) processes, respectively. Test Chip C is a 28 nm SRAM with a capacity of 32 Mbit and nominal operating voltage of 1.0 V. Test Chip D is

a 45 nm SRAM with a capacity of 4 Mbit and nominal operating voltage of 1.1 V. The probability of an upset in a single bit per incident particle is obtained for each applied bias condition using the following relationship,

$$Pr(V_{DD}) = \frac{N}{M} \frac{1}{A_{cell} \Phi} \tag{3.2}$$

where N is the number of observed errors, M is the number of bits in the test chip, A_{cell} is the cell area of the SRAM being tested, and Φ is the photon fluence. The form of Equation 3.2 describes the fraction of upsets per bit, $\frac{N}{M}$, and the number of photons incident on a single bit, $A_{cell}\Phi$. Combining these terms as in Equation 3.2 provides a description of the probability for a single incident particle to cause an error. Error bars are shown at the one-sigma confidence interval in all experimental and simulated probabilities. Table 3.1 shows the experimental supply voltage conditions, exposure time, and corresponding X-ray fluence for measurements on each test chip.

Figure 3.7 plots the SEU probability per incident photon, as described in Equation 3.2, as a function of supply voltage for SRAM test chips exposed to X-rays. Figure 3.7 shows that errors are observed when these devices are biased between 0.35 V and 0.8 V while exposed to X-rays. The resulting upset probability of all test chips exhibits an exponential dependence on applied bias because of the voltage dependence on critical charge. This is consistent with well established test procedures used for assessing the SEU cross-section and error rates for protons and muons [1, 2] and previous SEU results for alpha particles and heavier ions [73, 75, 76]. In the case of Test Chip B, upsets were observed within 10% of the nominal supply voltage of 0.9 V, which is within the designed operating voltage range for the SRAMs. Each of the SRAM test chips exhibits an SEU probability less than the total cell area at all supply voltages, resulting in probabilities less than unity. All observed errors had unique memory addresses, indicating that errors occurred randomly within the mem-

Table 3.1 X-ray Supply Voltage, Exposure Time, and Fluence

	Test Chip A		Test Chip B	
V_{DD} (V)	Time (s)	Fluence (cm^{-2})	Time (s)	Fluence (cm^{-2})
0.35	40	6×10^{13}	40	6×10^{13}
0.4	130	1.95×10^{14}	120	1.8×10^{14}
0.5	310	4.65×10^{14}	300	4.5×10^{14}
0.6	620	9.3×10^{14}	630	9.45×10^{14}
0.7			1260	1.89×10^{15}
0.8			630	9.45×10^{14}

	Test Chip C		Test Chip D	
V_{DD} (V)	Time (s)	Fluence (cm^{-2})	Time (s)	Fluence (cm^{-2})
0.45	90	1.35×10^{14}	270	4.05×10^{14}
0.5	180	2.7×10^{14}	30	4.5×10^{13}
0.55	180	2.7×10^{14}	360	5.4×10^{14}
0.6	540	8.1×10^{14}	860	1.29×10^{15}
0.65	300	4.5×10^{14}	1080	1.62×10^{15}
0.7	600	9×10^{14}	528	7.92×10^{14}

ory array during experiments and were not caused by repeated bit-flips in “weak” cells. Again it is noted that no bit-flips occurred due to reduced bias conditions during functionality and parametric tests before and after X-ray irradiation of all test chips under all bias conditions, indicating the memory operated under stable conditions during experiments.

Photocurrents produced by the overall photon flux are generated as the result of X-ray irradiation. The generated photocurrent produced by the collective effect of

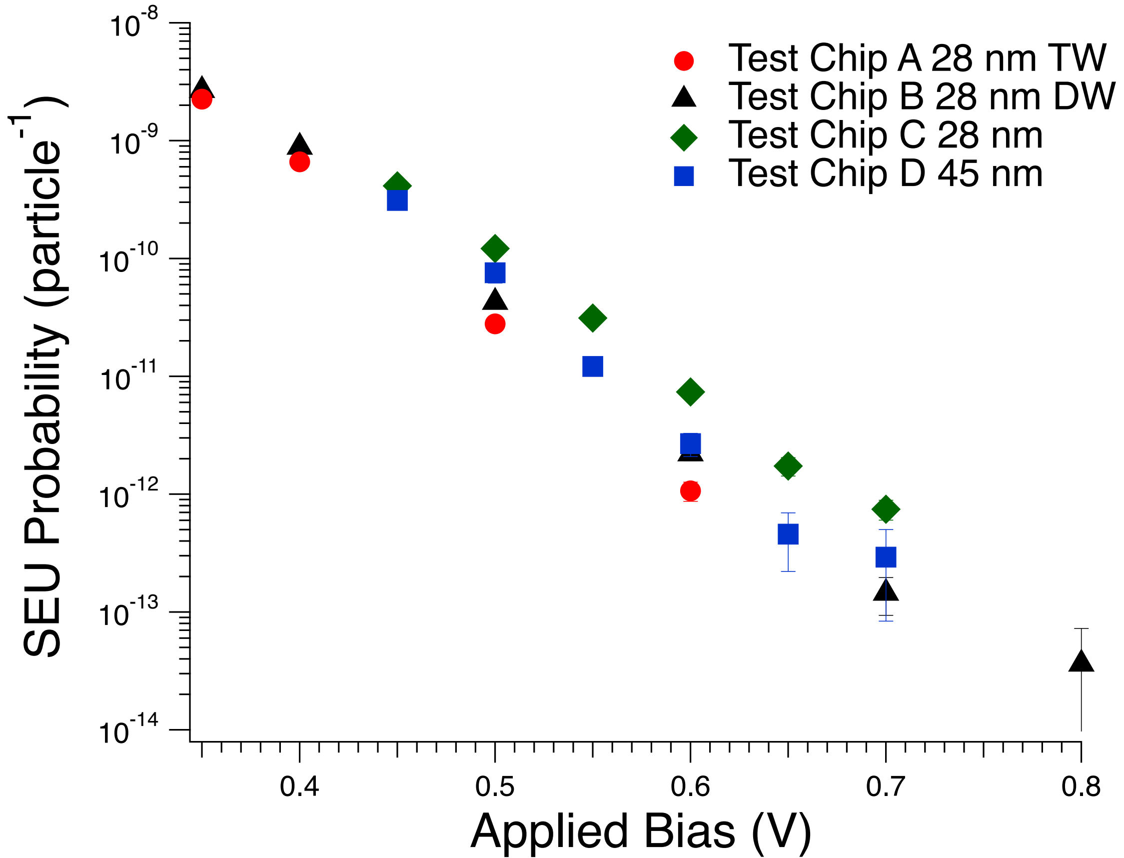

Figure 3.7 Experimental errors induced during irradiation with X-rays in an ARACOR 4100 X-ray irradiator. The bias sensitivity of critical charge in SRAMs provides strong evidence of energetic electron-induced upsets in modern SRAMs.

the X-ray source can be calculated as

$$I_{PC} = qV\dot{D}_{SiO_2}\dot{R}_{SiO_2} \tag{3.3}$$

where q is elementary charge, V is the volume of an SRAM cell, $\dot{D}_{SiO_2}$ is the dose-rate in SiO_2, and $\dot{R}_{SiO_2}$ is the density of e-h pairs generated per rad(SiO_2). The generated collective photocurrent in an individual SRAM cell is calculated with Equation 3.3 to be approximately 1 fA. SPICE simulations were performed for 28 nm SRAM test chips A and B for each experimental bias condition. The simulation results indicate restoring currents are greater than 100 nA at the lowest experimental supply voltage,

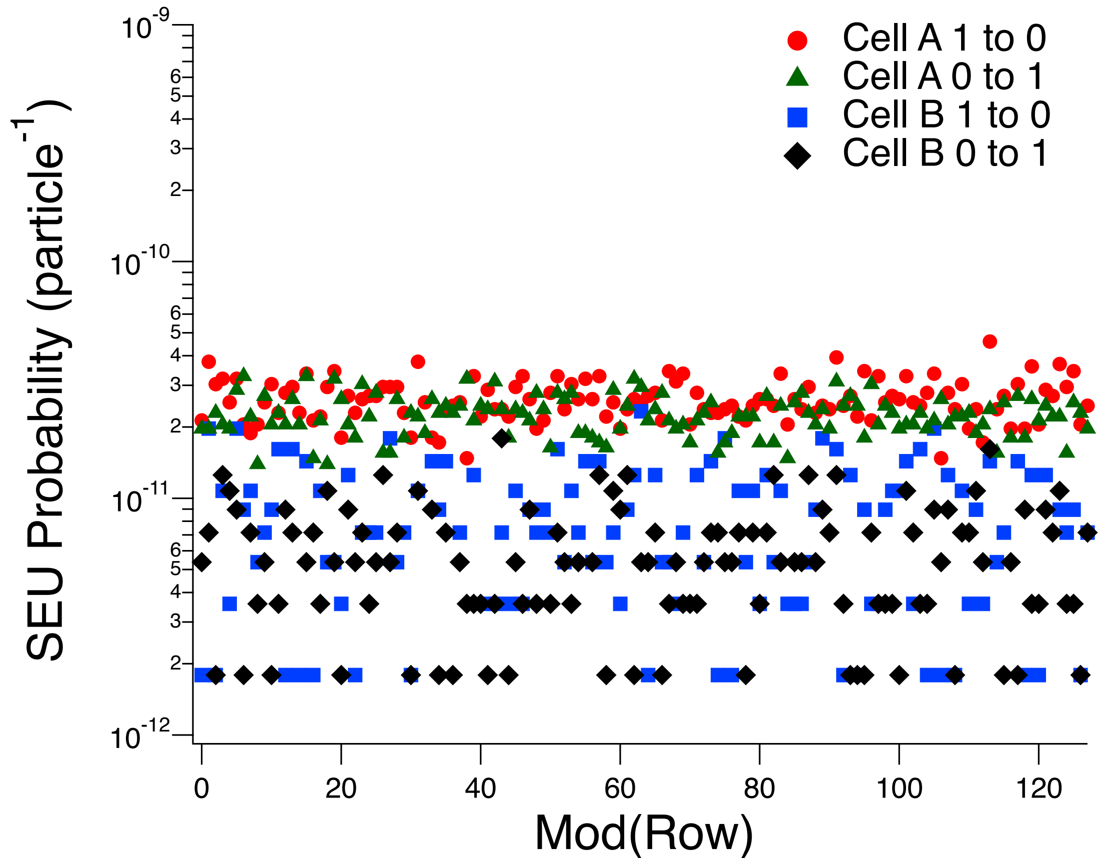

Figure 3.8 Experimental errors induced during irradiation with X-rays in an ARACOR 4100 X-ray irradiator. Results are for Test Chip B, errors are plotted as a function of distance from row 0, corresponding to V_{DD} lines, and row 128, corresponding to V_{SS} lines at a supply voltage of 0.35 V. Errors occur randomly within the SRAM cell and do not preferentially occur near supply voltage or ground rails.

0.35 V. Figure 3.8 shows the upset probability for Test Chip B at 0.35 V as a function of distance from V_{DD} and V_{SS} lines. Errors are shown to occur randomly between supply voltage and ground power metallization and do not preferentially occur near the supply voltage or ground lines, indicating that dose-rate effects do not contribute to the error rate in these experiments. Hence, as expected, collective photocurrents generated in X-ray experiments are much smaller than the restoring current of SRAM cells and are incapable of causing the observed errors.

Furthermore, the probability of coincident photon events contributing to the error rate can be calculated as,

$$Pr(X_1||X_2) = (\phi A_{cell}\tau)^2 \tag{3.4}$$

where ϕ is the incident photon flux, A_{cell} is the cell area, and τ is the characteristic time for an upset event (assumed to be 10 ns). Evaluation of Equation 3.4 for the 28 nm and 45 nm SRAMs results in probabilities of 6.45×10^{-10} and 1.9×10^{-9}, respectively, of coincident photons contributing a single upset to the experimental results. The contribution of coincident photons to the observed upsets on the time scale considered is therefore negligible.

Lastly, it is important to monitor the TID accumulated by the test chip, since this can lead to degradation of the memory and result in a loss of functionality [129]. The dose accumulated in the experiments for the triple-well 28 nm bulk SRAM, Test Chip A, was less than 1.9 krad(SiO_2). The dual-well SRAM, Test Chip B, accumulated 5 krad(SiO_2) during the experiments. Test Chip C, a 28 nm SRAM, accumulated a dose of 5.4 krad(SiO_2), and Test Chip D, a 45 nm SRAM, accumulated a total dose of 11.1 krad(SiO_2). Test Chip C, a 28 nm, 32 Mbit bulk SRAM, underwent the largest change in power supply current based on measurements before and after irradiation, where the pre- and post-irradiation power supply currents were 82.7 mA and 81.5 mA, respectively. This is a decrease in power supply current of less than 1.5%. Similarly, none of the other devices discussed in these experiments accumulated sufficient dose to compromise memory operation or cell integrity.

The above results and analysis demonstrate that, for the experimental conditions considered here, single energetic electrons produced by X-ray irradiation are by far the most likely cause of the observed errors within the SRAMs.

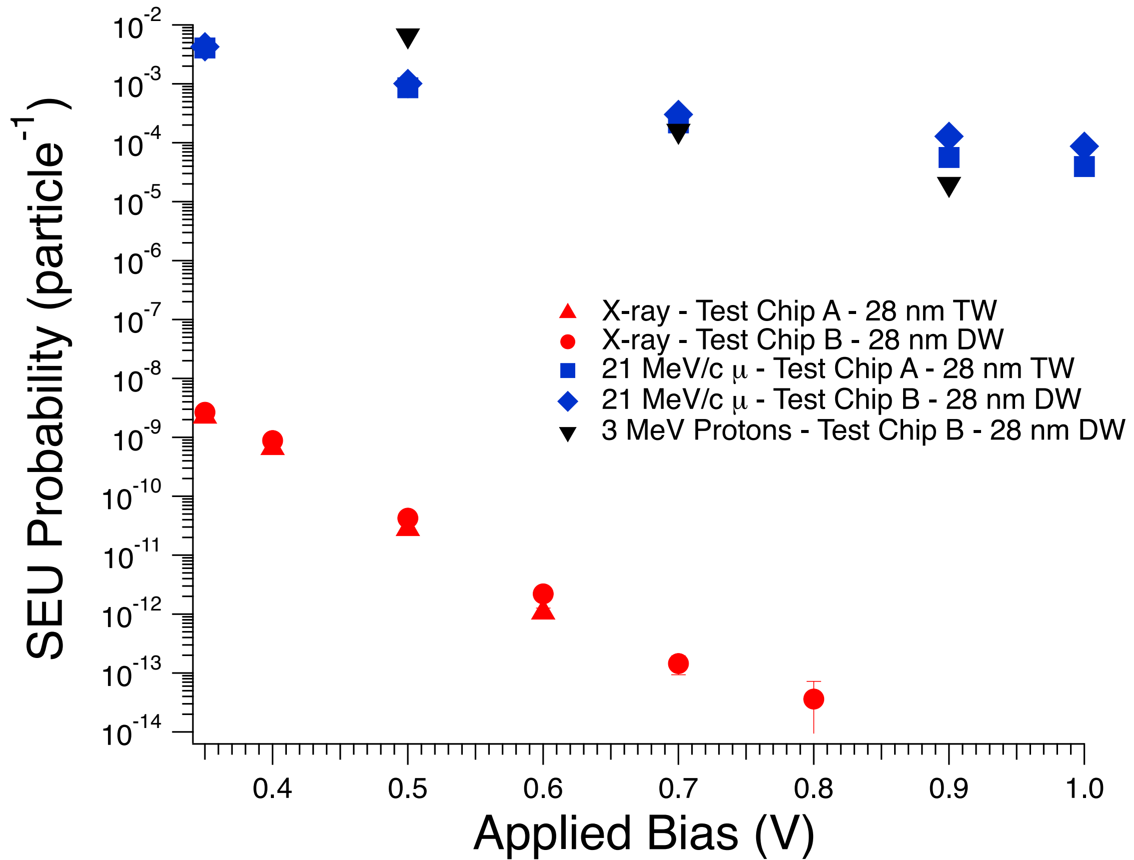

Figure 3.9 SEU probability dependence on supply voltage for X-ray irradiation, compared to low-energy protons and muons in 28 nm SRAMs. Results show that under nominal bias conditions protons and muons are capable of inducing upsets in 28 nm SRAMs while this sensitivity is absent for energetic electrons generated during X-ray exposure. Under reduced bias conditions, X-ray SEUs exhibit a larger dependence on supply voltage than muons and protons in the 28 nm technology nodes.

3.3 Comparison to Low-Energy Proton and Muon SEUs

With the observation of SEUs arising from X-ray irradiation, it is quite useful to quantify the significance of this effect relative to other well-understood phenomena. To this purpose, the data set presented in Figure 3.7 is compared to SEU data sets obtained with low-energy protons and muons.

Low-energy proton experiments were performed in the Pelletron facility at Vanderbilt University. Experiments were performed under vacuum with a monoenergetic proton beam at an energy of 3 MeV normally incident on Test Chip B and 1 MeV normally incident on Test Chip D. The sensitivity of the 28 nm SRAM test chip was investigated for supply voltage in the range of 0.35-1.0 V. The 45 nm SRAM test chip was investigated for applied biases of 0.8-1.2 V. The timing sequence for applied bias during experiments with low-energy protons is identical to that of Figure 3.2. Parts were tested to a fluence of 10^{12} cm^{-2}.

Muon experiments were performed at TRIUMF using the M15 beam line. Low-energy positively charged muons with a known energy distribution were normally incident on Test Chips A and B, 28 nm bulk SRAM, and Test Chip D, a 45 nm SRAM. The muon beam energy characterization at TRIUMF is described in [2]. The incident muon energy was varied by means of a tunable momentum filter [2, 16]. The timing sequence for applied bias during experiments with low-energy muons is identical to that of Figure 3.2. Parts were exposed to a total fluence of 6.2×10^{8} cm^{-2}. An SEU probability is obtained for muon and low-energy proton experiments using the particle fluence for each, respectively, from Equation 3.2.

Figures 3.9 and 3.10 show SEU probabilities from low-energy proton and muon experiments plotted alongside X-ray SEU data from Figure 3.7 for 28 nm and 45 nm test chips. All test chip samples exhibit exponential SEU probability dependence on

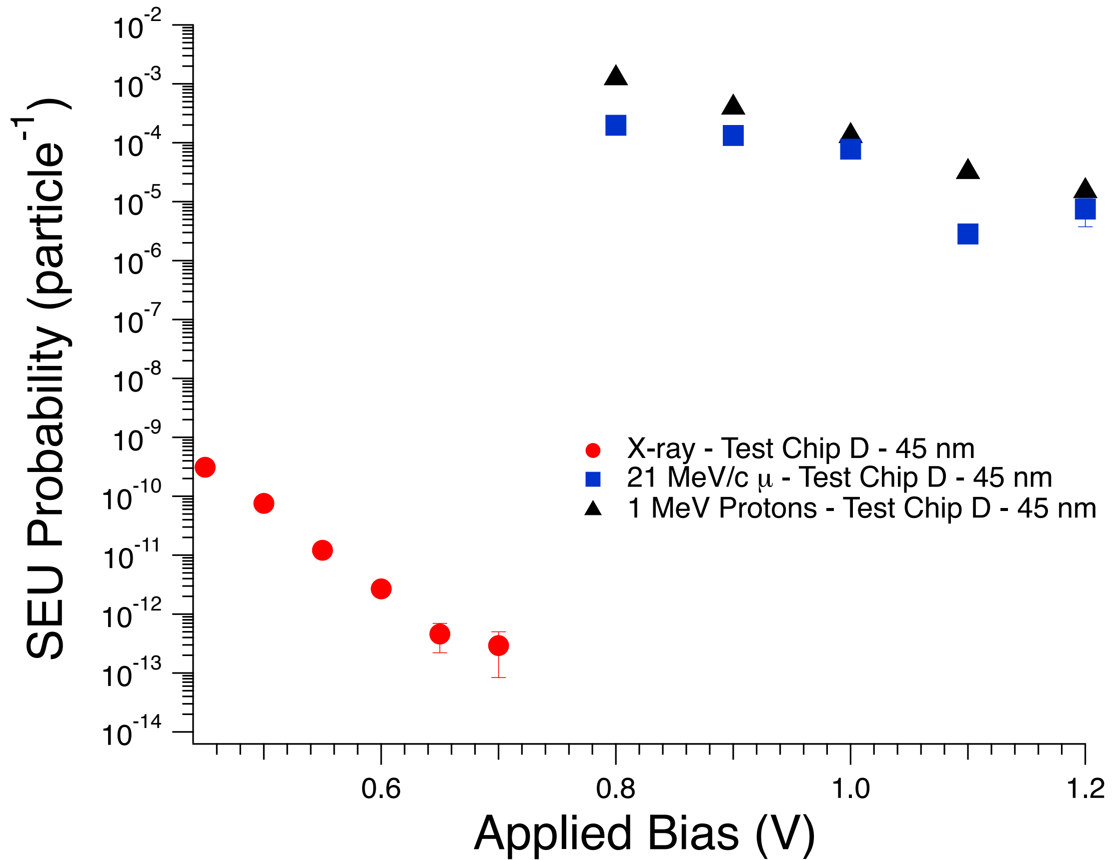

Figure 3.10 SEU probability dependence on supply voltage for X-ray irradiation, compared to low-energy protons and muons in 45 nm SRAMs. Results show that under nominal bias conditions protons and muons are capable of inducing upsets in 45 nm SRAMs while this sensitivity is absent for energetic electrons generated during X-ray exposure. Under reduced bias conditions, X-ray SEUs exhibit a larger dependence on supply voltage than muons and protons in the 45 nm technology nodes.

applied bias, consistent with previous results [1,2]. Additionally, higher LET particles also exhibit a smaller slope than that of low LET particles, in this case low-energy protons and muons exhibit a smaller dependence on applied bias than measured X-ray SEU probabilities. These results are consistent with previous work that shows similar trends in heavy-ion, alpha particle, and low-energy proton SEU cross-sections and their supply voltage dependence [1, 73, 75, 76]. Furtheremore, electron sensitivity is observed within 10% of nominal bias conditions for test chip B, indicating that SEUs initiated by high energy electrons may be observable in more sensitive present-generation ICs, and at nominal supply voltages for future technology nodes. It is noted that, under nominal bias conditions, test chips A, B, and D exhibit sensitivity to muons and protons, while no events initiated by single high-energy electrons are observed. This indicates that high-energy electrons are much less important than protons and muons for SRAMs from these technology nodes, operating at or near nominal bias conditions.

As discussed in Chapter 2.2, design constraints often place restrictions on device operating frequency and power, forcing designers to vary the supply voltage as a means of meeting design specifications. These results show that as the applied bias is reduced, X-ray SEUs exhibit a larger dependence on supply voltage (a larger slope) than muons and protons in the 28 nm and 45 nm technology nodes.

Chapter 4

Simulation of Electron-Induced SEUs

The experimental results from Chapter 3 show that 28 and 45 nm SRAMs exhibit SEU sensitivity when exposed to energetic X-rays. Analysis of those results indicates that the observed errors are electron-induced SEUs. This chapter presents simulations and analysis of Monte Carlo radiation transport codes investigating the experimental results of Chapter 3. Section 4.1 presents simulations of an X-ray spectrum, consistent with that used in Chapter 3, incident on a target structure representative of 45 nm bulk SRAMs. Simulation results are shown to be in good agreement with the experimental data from Chapter 3 and show that photo-electrons generated by incident X-rays deposit energy in excess of the estimated critical charge under a wide range of applied bias. The relative impact of electron-induced SEUs in the space radiation environment is presented by performing error-rate calculations for a 45 nm SRAM in the geosynchronous orbit and environment during the solar minimum cycle in Section 4.2. Additional error-rate analysis is performed for the Jovian environment. Analysis of δ-ray contributions to single- and multiple-bit upset rates for SRAMs irradiated with heavy ions is discussed in Section 4.3.

4.1 Simulation of X-ray Energy Deposition in SRAMs

Radiation transport simulations were performed with MRED [126], a Geant4-based code [130] with Fortran extensions that include PENELOPE 2008 [44], to evaluate the potential impact of electrons produced by energetic X-rays on the device SEU response. The use of the PENELOPE 2008 package [44] increases the fidelity and resolution of calculations involving low energy (less than 50 keV) electrons, photons

and positrons. PENELOPE 2008 extends the low-energy range for electromagnetic processes from 250 eV down to approximately 100 eV and also tracks electrons with greater spatial resolution. These refinements produce increased fidelity of energy deposition estimates in the small sensitive volumes of interest in this work.

The attenuated X-ray energy spectrum from Figure 3.3 is used in the simulations to simulate the full X-ray exposure environment and range of generated electron energies incident on the exposed SRAM test chip. A 4 kbit SRAM array is simulated, using a sensitive volume structure consistent with a 45 nm bulk SRAM using MRED. Energy deposition is calculated for individual X-rays on an event-by-event basis. The sensitive volume geometry used was 0.22 $\mu m^2 \times 500$ nm, which is representative of 45 nm processes in the ITRS roadmap [77]. Additionally, the simulated structure includes the 1 mm aluminum attenuator and appropriate BEOL thickness with 15 μm of oxide and metallization. The SRAM was simulated to a total photon fluence of 2×10^9 cm^{-2}. This fluence was found to be sufficient to determine the energy deposited and ultimately estimate the resulting error rate with adequate precision to compare with the experimental data. The vertical black lines in Figure 4.1 represent estimates of critical charge for 45 nm SRAMs as in [9] for supply voltages of 0.55 V and 1.1 V, which correspond to 0.19 fC and 0.38 fC of generated charge, respectively, and are used to indicate the charge generation required to upset cells.

The simulated SEU probability of a 45 nm SRAM is shown in Figure 4.1, indicating that secondary electrons generated by incident X-rays are capable of depositing sufficient energy to exceed critical charge estimations. The eventual upsets result from collection of thermalized *e*-*h* pairs generated by the high-energy electrons. These results, suggesting energetic electrons are capable of depositing sufficient ionizing energy to exceed the critical charge of 45 nm SRAMs operating under reduced supply voltage, are consistent with previous computational results reported in [9, 10]. The

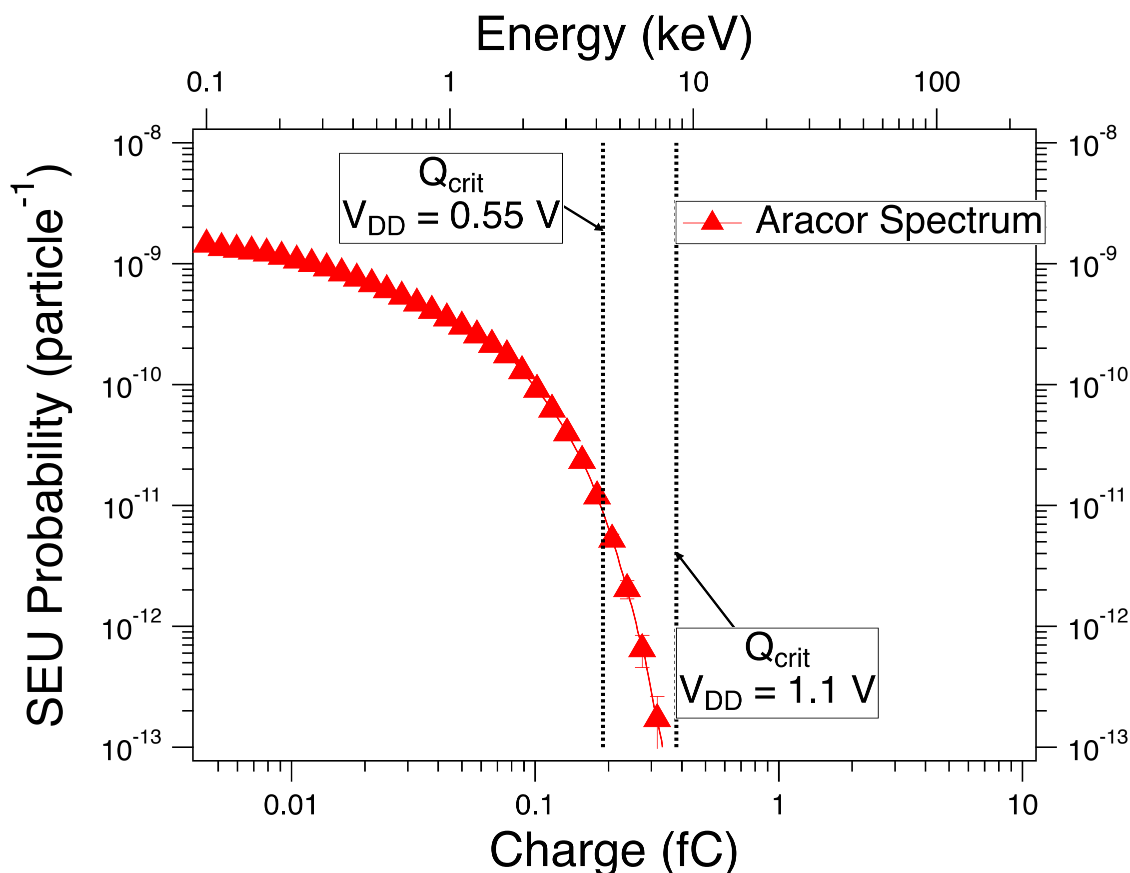

Figure 4.1 MRED simulation results of the attenuated ARACOR spectrum, seen in Figure 3.3, normally incident on a 45 nm bulk SRAM structure. The vertical black lines represent the lower-limit estimates of critical charge for a 45 nm SRAM. The results provide supporting evidence suggesting that energetic electrons generated by incident X-rays are capable of depositing sufficient energy to exceed the estimated upset threshold.

probability distribution shown in Figure 4.1 at a supply voltage of 0.55 V agrees with experimental test results from Test Chip D in Figure 3.7 within a factor of two. These results suggest that the 45 nm SRAM is insensitive to single electron-induced SEU at nominal supply voltage, consistent with the SEU data in Figure 3.7.

Further analysis of individual events shows that single electrons scattering within the sensitive volumes representative of sub-65 nm bulk and SOI technology frequently deposit energy in excess of the estimated critical charge thresholds in Figure 4.1. Figure 4.2 shows 10 keV electrons transporting through a 500 nm silicon cube and

depositing 2.1 keV and 2.6 keV within an embedded 50 nm cube as shown in Figures 4.2(a) and 4.2(b), respectively. Each event shown in Figure 4.2 results in the generation of additional energetic electrons, in either single or multiple scattering events, that subsequently transport and come to rest within the sensitive volume structure, losing all of their energy and reabsorbing into the material. While the incident electron does not stop within the 50 nm silicon cube in either of the events depicted in Figure 4.2, energy is transferred to secondary electrons. The total energy deposited in these volumes exceeds the estimation of critical energy required to produce a SEU in the sub-65nm nm bulk and SOI technology operated at reduced voltage [1].

These simulation results confirm that energy deposition from energetic electrons generated in photoabsorption events is the most likely explanation for the experimentally observed upsets in Figure 3.7.

The sensitive volume geometry chosen in this research was a static, uncalibrated model for the simulation results reported in Figure 4.1. The vertical lines shown in Figure 4.1 represent simple calculations of critical charge in a 45 nm SRAM from Equation 2.9. Using the experimental X-ray upset probability for a 45 nm SRAM from Figure 3.7 the critical charge as a function of supply voltage can be extrapolated from the simulation results of Figure 4.1.

Figure 4.3 shows the critical charge extrapolated from simulation results and values calculated from Equation 2.9 as a function of supply voltage for a 45 nm SRAM. Each estimation of critical charge exhibits a linear dependence on applied bias between 0.45-0.7 V, however, the slopes differ in significant ways. Critical charge estimates using Equation 2.9 would cause simulation results to underestimate the SEU probability for applied bias conditions less than 0.55 V and overestimate for higher bias conditions. The linear slope of the extrapolated critical charge with respect to supply

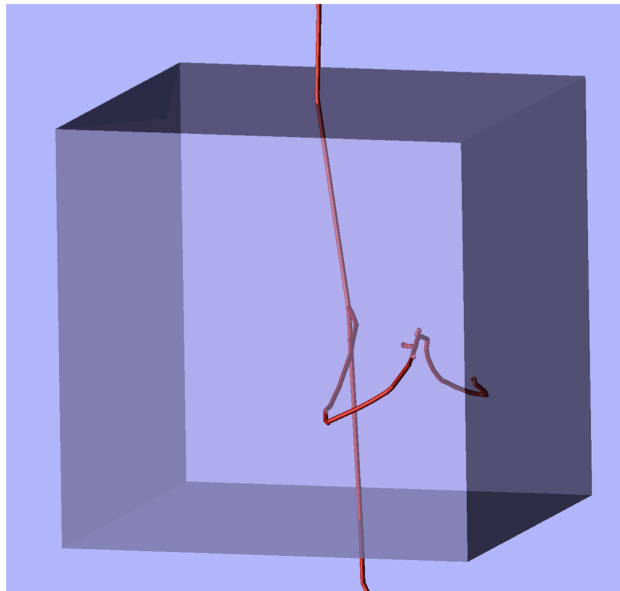

(a)

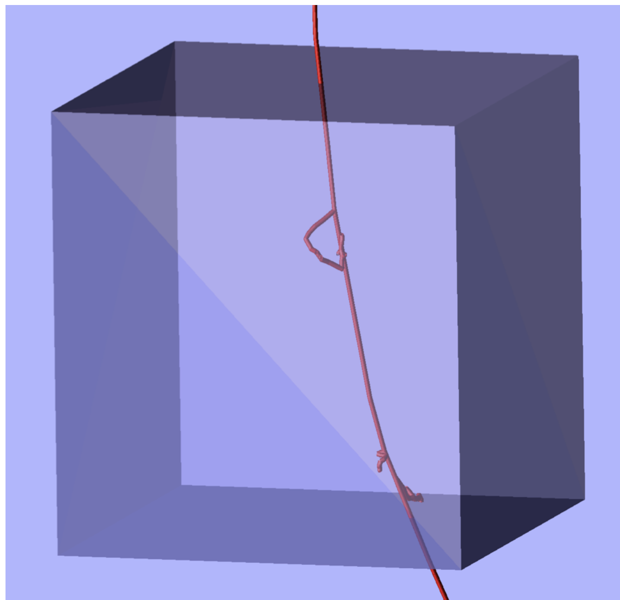

(b)

Figure 4.2 Incident 10 keV electrons/δ-rays are shown scattering in a 50 nm cube of silicon. Event 4.2(a) shows a 2.1 keV energy deposition event that produces additional electrons/δ-rays in a chain of inelastic scattering events. Event 4.2(b) shows a 2.6 keV energy deposition event that produces several tertiary electrons/δ-rays in a series of inelastic scattering events.

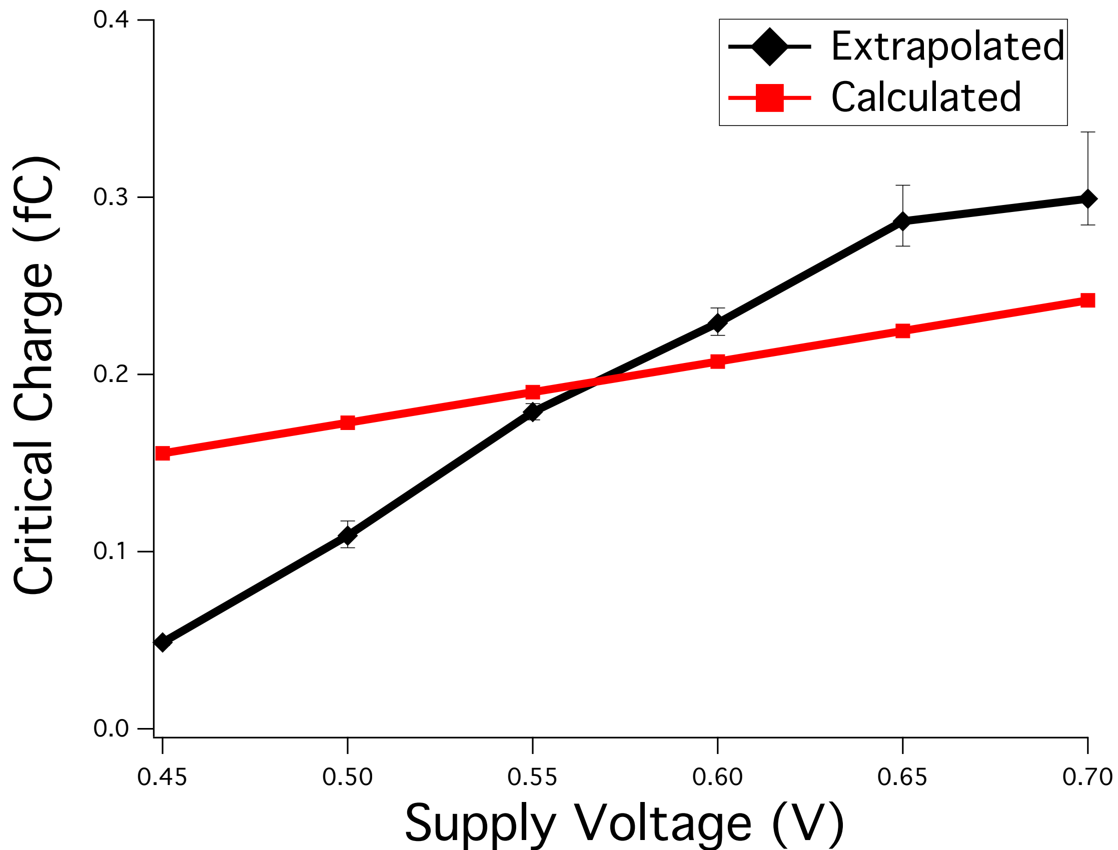

Figure 4.3 Comparison of simulated versus experimental normalized cross-section for Test Chip D, a 45 nm bulk SRAM.

voltage is interesting and consistent with previous attempts to quantify the critical charge and SEU cross-section dependence on supply voltage [73–76].

The transient response of an SRAM to charge generated by ionizing radiation is a complicated time-dependent function of the gate capacitance, resupply current, and feedback from the cross-coupled inverter. Many of these factors are not accounted for in Equation 2.9. The resulting disagreement between the extrapolated and estimated critical charge in Figure 4.3 is, therefore, not surprising. When determining the critical charge of SRAMs fabricated in advanced technology nodes it is necessary to consider the complicated circuit-level transient response.

In the next section, the extrapolated critical charge values from Figure 4.3 will be used evaluate electron-induced error rates in the geosynchronous near-Earth and Jovian environments.

4.2 Electron-Induced SEU Event Rates

Comparing the experimental probabilities in Figures 3.9 and 3.10 indicates the sensitivity of SRAMs to protons, muons, and electrons, however, error rates depend on the flux of these particles for different environments. Trapped electrons form two different belts in the near Earth radiation environment, each with distinct characteristics [3, 4]. The Jovian electron environment is equally formidable as it contains electrons with higher energy and flux than that of the near-Earth environment. This section investigates the potential for electron-induced SEUs in the near-Earth and Jovian environments using MRED simulations.

Simulations were performed to estimate SEU event rates for trapped electrons at geosynchronous orbit during solar maximum with 150 mils of aluminum shielding using spectra obtained from the AE-8 model for the near-Earth environment. The differential flux spectrum of incident electrons through 150 mils of aluminum shielding is plotted in Figure 4.4. The trapped electron environment described in Figure 4.4 is much more energetic than the generated electron spectrum used in X-ray experiments described in Chapter 3. The most energetic electrons at geosynchronous orbit during solar maximum have energy of approximately 10 MeV, which would require more than 500 mils of aluminum shielding to attenuate completely [3, 4].

Characteristics of the Jovian electron environment were discussed in Section 2.4.3. Simulations of electron-induced SEU event rates were performed for the differential flux spectrum shown in Figure 2.37. Additionally, attenuated differential electron and proton spectra are presented in Figures 4.5 and 4.6 showing the impact of 100 mils,

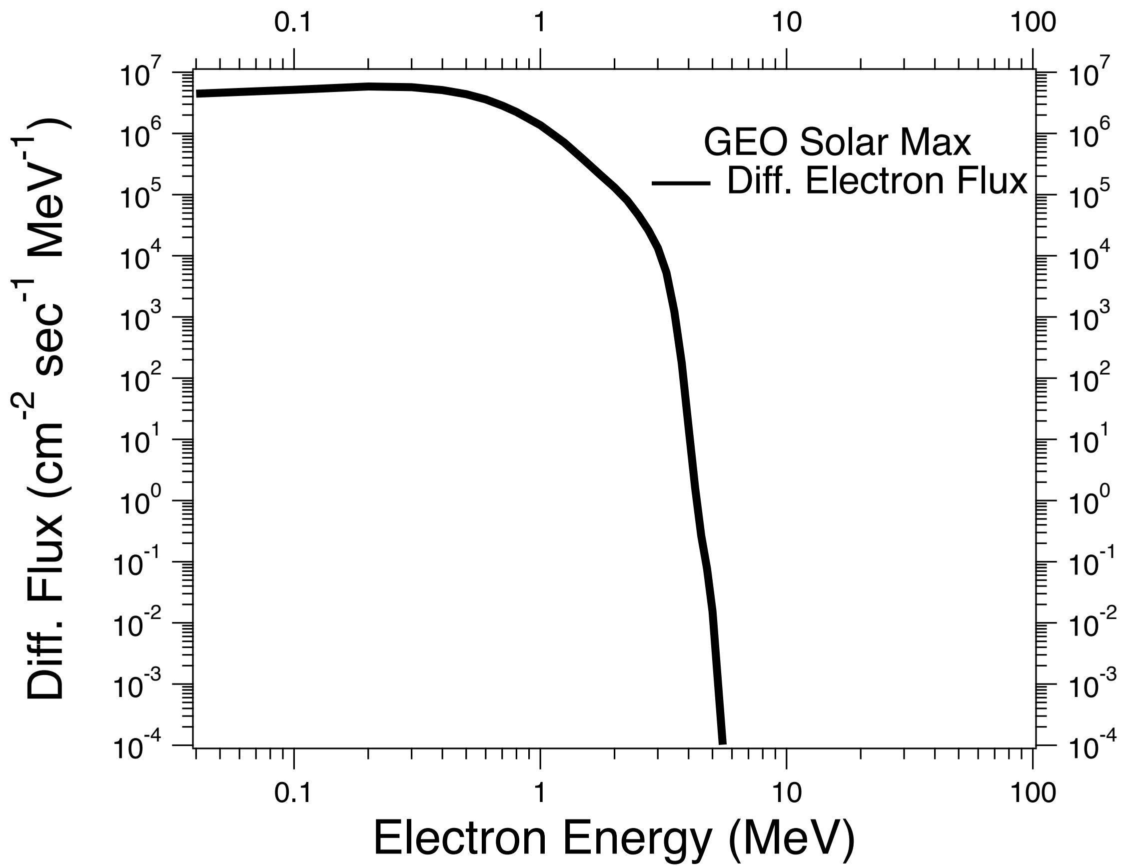

Figure 4.4 The differential flux spectrum of incident electrons is plotted using the AE-8 description of the electron environment, at geosynchronous orbit during solar maximum with 150 mils aluminum shielding. It is noted that 150 mils of aluminum is sufficient to shield the simulated SRAM from protons in this environment.

730 mils, and 870 mils of aluminum shielding on the differential flux of electrons and protons during the Jovian and Europa phases of the Juno spacecraft mission to the Jupiter planetary system. The electron flux spectrum shown in Figure 4.5 indicates that 100 mils of aluminum shielding has minimal impact on the flux of low-energy electrons (<100 keV). The proposed higher shielding thicknesses of 730 and 870 mils, however, have a significant impact on the flux of low-energy electrons, reducing it by over two orders of magnitude.

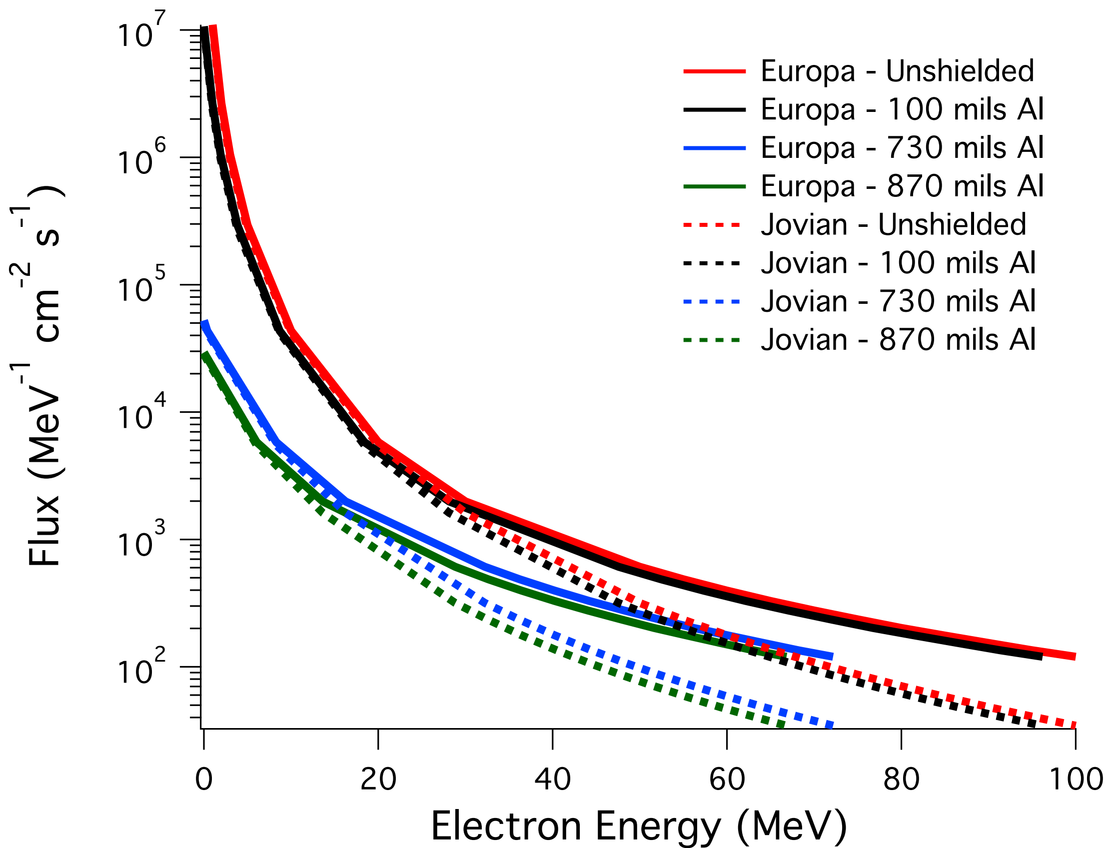

Figure 4.5 Differential electron flux for unshielded, 100 mils, 730 mils, and 870 mils of aluminum shielding in the Jovian and Europa tour phase of the Juno spacecraft mission to the Jupiter planetary system.

In contrast to electrons, Figure 4.6 shows that shielding of protons has a much greater impact on the proton flux in the Europa environment, reducing the high-flux

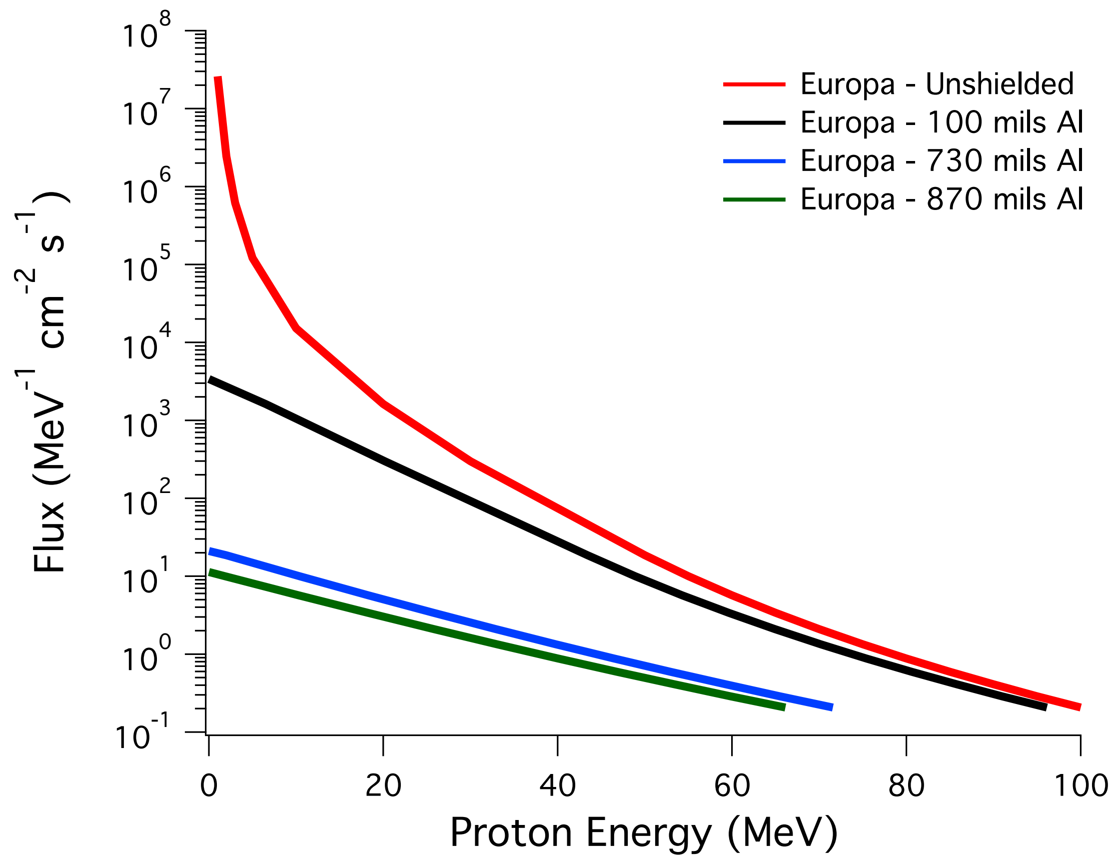

Figure 4.6 Differential proton flux for unshielded, 100 mils, 730 mils, and 870 mils of aluminum shielding in the Europa tour phase of the Juno spacecraft mission to the Jupiter planetary system.

region of low-energy (<5 MeV) protons from the unshielded spectrum. As mentioned previously, the flux and energy of electrons and protons in the Jovian environment is significantly higher than that of the near-Earth environment. The simulations of the Jovian environment investigate an unshielded part, and parts with varying shielding thicknesses, in the Europa and Jovian tour segments of the Juno spacecraft mission.

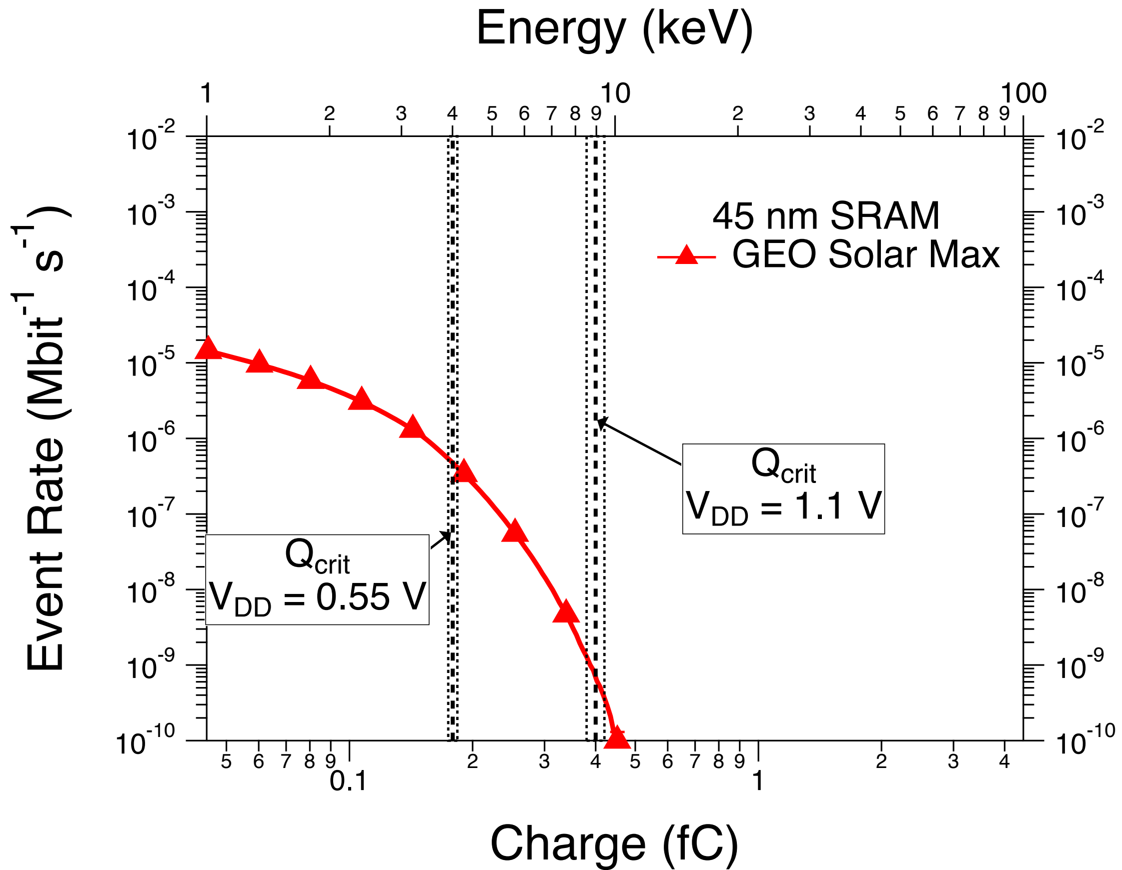

Figure 4.7 MRED simulations performed on the 45 nm structure from Figure 4.1 using the AE-8 description of the electron environment, at geosynchronous orbit during solar maximum with 150 mils aluminum shielding. Simulation results show that the event rate of electrons is small for devices operated at nominal supply voltage. However, more sensitive devices will experience a significant increase in single electron events. These results suggest that operating SRAMs under reduced bias conditions will result in a dramatic increase in single electron events.

MRED was used to model the interaction of the particle spectrum with the semi-

conductor materials. The material structure is identical to the structure from Figure 4.1, corresponding to a 45 nm bulk SRAM. The vertical lines shown in Figure 4.7 are the extrapolated critical charge from Figure 4.3 and indicate the expected error rates for 45 nm SRAMs operating at 0.55 V and 1.1 V at geosynchronous orbit. Figure 4.7 shows the resulting simulated event rates (left/right axis) as a function of generated charge (bottom axis) or energy deposited (top axis) within the sensitive volume of a single 45 nm SRAM cell for the near-Earth environment. Electron energy deposition events rarely exceed 10 keV, which is consistent with Figure 4.1 and previous studies of δ-rays [9, 10]. Figure 4.7 demonstrates the rare nature of electron-induced SEU events in the near-Earth space radiation environment, indicating that many years of flight time may elapse before the observation of such an event is expected for a typical 45 nm bulk SRAM operating under nominal bias conditions.

Figure 4.7 shows that the electron-induced SEU event rates depend strongly on the critical charge of the SRAM; a reduction of critical charge from 0.4 fC to 0.2 fC results in a change in event rate of approximately two orders of magnitude. Employing more sensitive SRAM technologies or operating at reduced supply voltage conditions has a direct and significant impact on SRAM error rates. In contrast, total error rate predictions for a 65 nm SRAM at geosynchronous orbit in the solar minimum environment are on the order of 2.4×10^{-6} Mbit^{-1} sec^{-1} [15]. At geosynchronous orbit in "worst-day" conditions, error rates for the same 65 nm SRAM are as high as 3.6×10^{-3} Mbit^{-1} sec^{-1} [15]. This indicates that the error rates at geosynchronous orbit of larger technology nodes with higher critical charge are roughly 2.5–5 orders of magnitude higher than estimates of electron-induced error rates at nominal bias conditions.

Conclusions are similar for the Jovian trapped particle environment to those of the near-Earth environment when evaluating SEU error rate estimations. Here, the

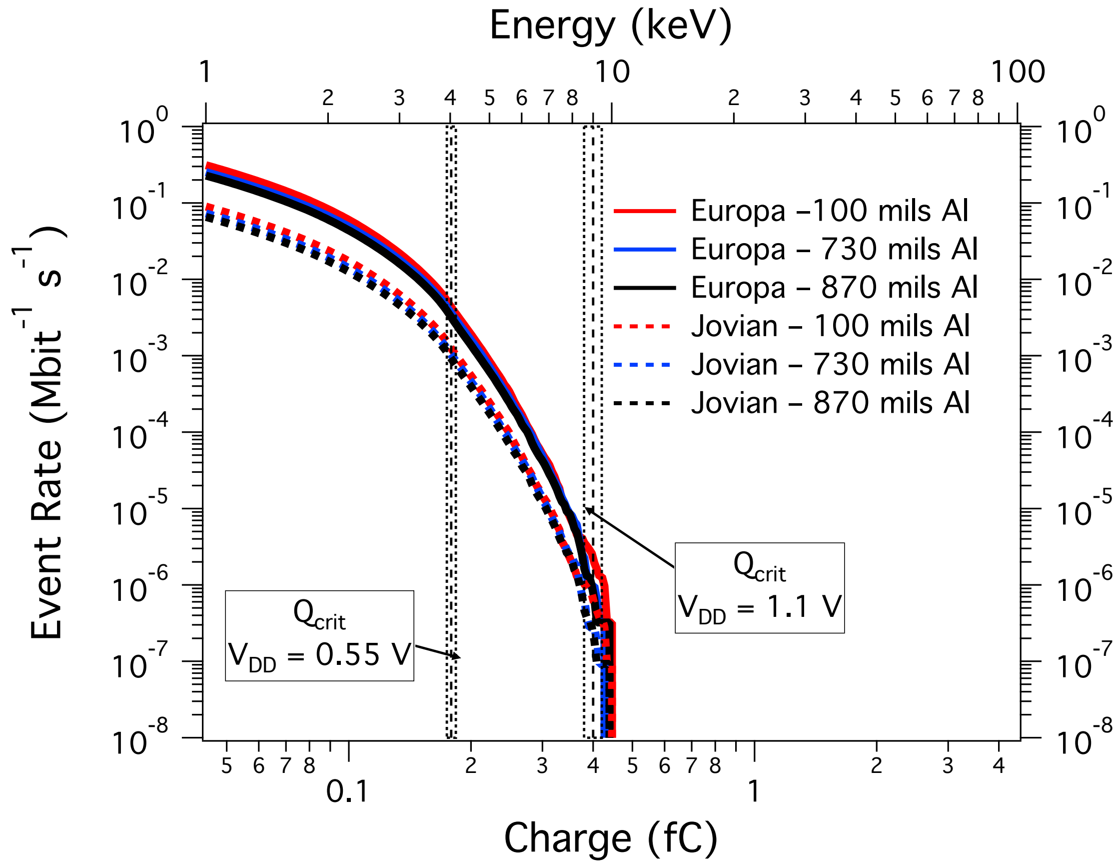

Figure 4.8 MRED simulations performed on the 45 nm structure from Figure 4.1 using the differential electron flux of Figure 4.5 for shielding thicknesses of 100, 730, and 870 mils of aluminum. Results show that shielding has some impact on the overall electron-induced SEU error rate in the Jovian and Europa environments as shown by the slight reduction in event rates for equivalent orbits. Devices operated in a low-power or quiescent mode are likely to experience an unacceptably large upset rate while in proximity to the Jupiter planetary system.

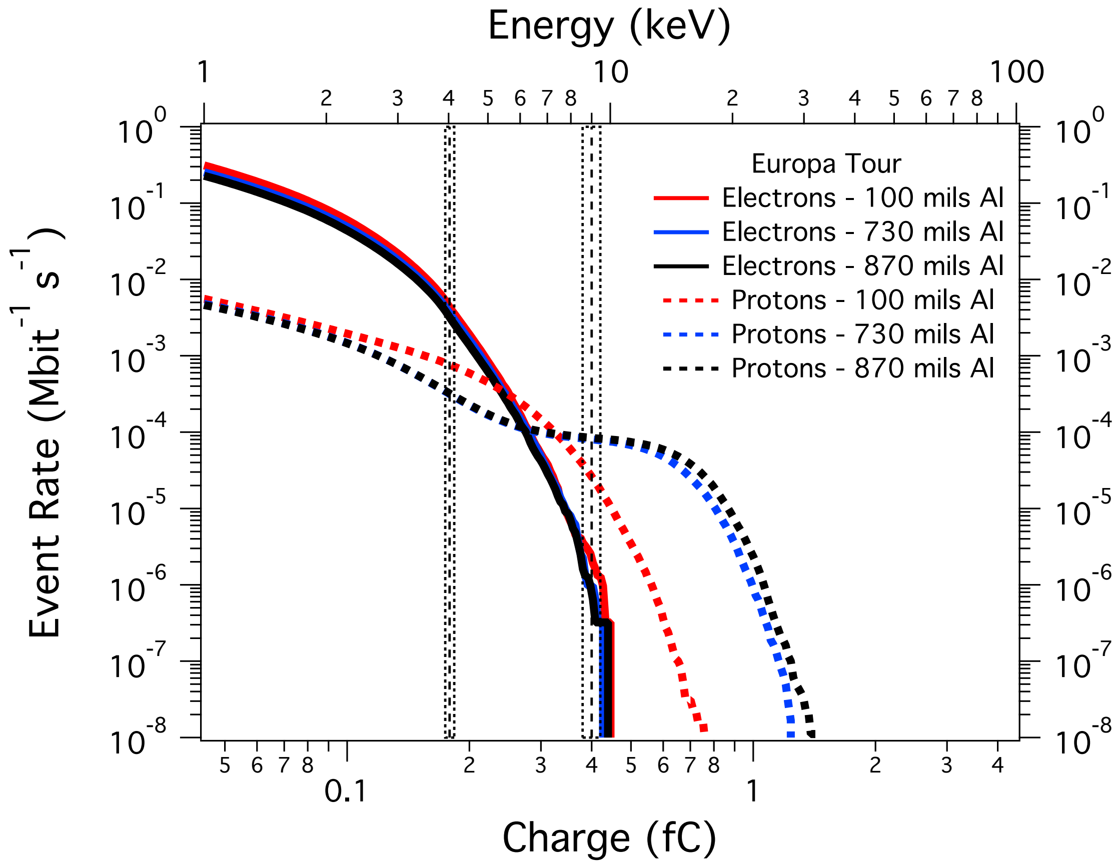

Figure 4.9 MRED simulations performed on the 45 nm structure from Figure 4.1 using the electron environment of Figure 4.5 and proton environment of Figure 4.6 for shielding thicknesses of 100, 730, and 870 mils of aluminum. Proton-induced SEU error rates are observed to be higher than electron-induced SEU error rates at nominal supply voltage. Electron-induced SEU error rates become higher than proton-induced error rates under reduced bias conditions.

vertical lines shown in Figures 4.8 and 4.9 are the extrapolated critical charge from Figure 4.3 and indicate the expected error rates for 45 nm SRAMs operating at 0.55 V and 1.1 V in the Jovian environment. Figure 4.8 shows the electron-induced SEU error rate as calculated by MRED simulations performed on the 45 nm structure from Figure 4.1 using the differential electron flux of Figure 4.5 for shielding thicknesses of 100, 730, and 870 mils of aluminum. Results show that shielding has some impact on the overall electron-induced SEU error rate in the Jovian and Europa environments as shown by the slight reduction in event rates for equivalent orbits. The difference in error rates for increasing shielding thicknesses appears to be negligible near nominal operating voltages for the 45 nm SRAM test chip while there is some indication that thicker shielding decreases the SEU error rate *slightly* under reduced bias conditions. Increasing shield thickness appears to provide diminishing returns for attenuating the electron-induced SEU error rate in near Jupiter and Europa as it is impractical to use sufficient shielding to stop the 100 MeV electrons present in those environments. The presence of higher energy electrons in the Europa electron flux spectrum does have an impact on the calculated error rates shown in Figure 4.8 as noted by their consistently higher event rates for all shielding thicknesses as compared to those of the Jovian environment. Devices operated in a low-power or quiescent mode are likely to experience an unacceptably large upset rate while in proximity to the Jupiter planetary system.

Figure 4.9 shows MRED simulations performed on the 45 nm structure from Figure 4.1 using the electron environment of Figure 4.5 and proton environment of Figure 4.6 for shielding thicknesses of 100, 730, and 870 mils of aluminum. Proton-induced SEU error rates are observed to be higher than electron-induced SEU error rates at nominal supply voltage conditions. While the proton flux is significantly attenuated by the presence of the aluminum shielding, this results in a proton spec-

trum that is more likely to cause bit-flips within the SRAM cell. This is shown by the slight increase in event rate for shielding thicknesses of 730 and 870 mils as compared to that of 100 mils. Interestingly, Figure 4.9 suggests that electron-induced SEU error rates are estimated to be higher than proton-induced error rates under reduced bias conditions. This is similar to trends observed in Figures 3.9 and 3.10 where the measured SEU probability for protons was higher than that of X-rays near nominal supply voltage conditions. However, as supply voltage decreases, the X-ray SEU probability increases at a much higher rate than the proton SEU probability and could result in higher SEU error rates at reduced bias conditions.

Comparing the electron-induced SEU error rates for the near-Earth and Jovian environments yields consistent results. Although the environments are dramatically different, the calculated SEU error rates suggest that electron-indued SEUs at or near nominal bias conditions are extremely rare events and unlikely to contribute to error rates in SRAMs fabricated in current sub-65 nm technology nodes. The presence of high fluxes of energetic electrons, as high as 100 MeV, has a significant impact on error rates, especially under reduced bias conditions, in the Jovian environment when compared to that of the lower energy electrons found in the Van Allen radiation belts. The differences between the Jovian and near-Earth environments is most significant at reduced bias conditions where electron-induced SEU error rates are higher than those of the geosynchronous environment by more than an order of magnitude. Furthermore, the estimated error rates in Figures 4.7 and 4.8 suggest that spacecraft operating near an enegertic electron environment, like those found in the Van Allen radiaiton belts or the Jupiter planetary system, that enter into a power-saving or quiescent mode would significantly increase the likelihood of SEUs contributing to anomalous behavior in the onboard electronics systems.

4.3 Impact of Delta-rays on Microelectronics

In this section, single ionizing particles are simulated. The resulting tracks are analyzed, and energy deposited by δ-rays within small volumes is evaluated as a function of position within a large silicon structure. The evaluation volumes are 50 nm cubes, representing regions where energy deposition results in the generation and collection of charge that contributes to the device response.

The sensitive volume model and approach for evaluating upset events in SOI used in this section is consistent with [9, 10, 53]. The sensitive volumes are 50 nm cubes that are representative of typical active regions in modern SOI technology [53]. A concentric cylindrical target of silicon is utilized to characterize the radial dependence of energy deposition from the incident ion track structure; the thickness of the target structure is 50 μm. The range of all incident particles evaluated in this section is much longer than the thickness of the target. The threshold for an upset event is defined as in previous sections, the amount of energy deposited in the sensitive volume required to generate the devices critical charge. IBM has reported their 65 nm SOI technology node to have a critical charge between 0.14-0.28 fC [1], which corresponds to energy deposition of 3.15-6.3 keV within the sensitive volume. Additionally, the critical charge estimate of 0.08 fC for upset from [9] corresponds to 1.8 keV of energy deposited within the sensitive volume and is used to evaluate the sensitivity of future technology nodes. It is assumed that energy below this threshold does not result in an upset event, and energy deposition greater than or equal to the threshold results in an upset.

Events are simulated using He and Ne ions; the energy distribution of δ-rays generated will be similar for fixed incident ion energy, their generation rate will depend on the incident ion LET. The target geometry is chosen to be cylindrically symmetric

about the incident ion path, energy deposition is evaluated as a function of orthogonal distance from the trajectory of the incident ion. The energy deposited within a 50 nm cube is sorted by the orthogonal distance from the incident ion trajectory and the magnitude of energy deposited. The resulting histograms are described by a function $f(E, R)$ which represents the differential energy spectrum in a 50 nm cube at radius R.

Using this method, the sensitive volumes generated consistently account for the largest energy deposited by the ensemble of δ-rays in a local region of target material during a simulated heavy-ion event. Consequently, this calculation represents a worst-case analysis of "track structure" contributions to SEUs. The representation of a 560 MeV N event using this technique can be seen in Figure 4.10. Each cube represents the location of energy deposited by δ-ray(s) and illustrates the spatial non-uniformity and variation in magnitude of δ-ray energy deposition events along their trajectory. The color intensity scale shows the magnitude of energy deposited, where warmer colors, red for example, represent larger energy deposition events and cooler colors, such as green, represent smaller energy deposition. This allows the visual representation of heavy-ion track structure and identification of the spatial location of large energy deposition events.

Figures 4.11 and 4.12 compare the energy deposited within a 50 nm cube for the analytical expectation of the Katz model,[119, 120] shown as the solid red line, with results obtained using MRED, represented by the box and whisker data set in black. MRED data represents the average energy within a 50 nm cube, shown as the lower edge of the box, the 90th percentile of events, shown as the upper edge of the box, and the whisker, representing the largest energy deposition event observed. Simulation results indicate that MRED agrees well with the Katz model expectation of energy within a 50 nm cube as shown by the lower edge of each box and the red line. The Katz

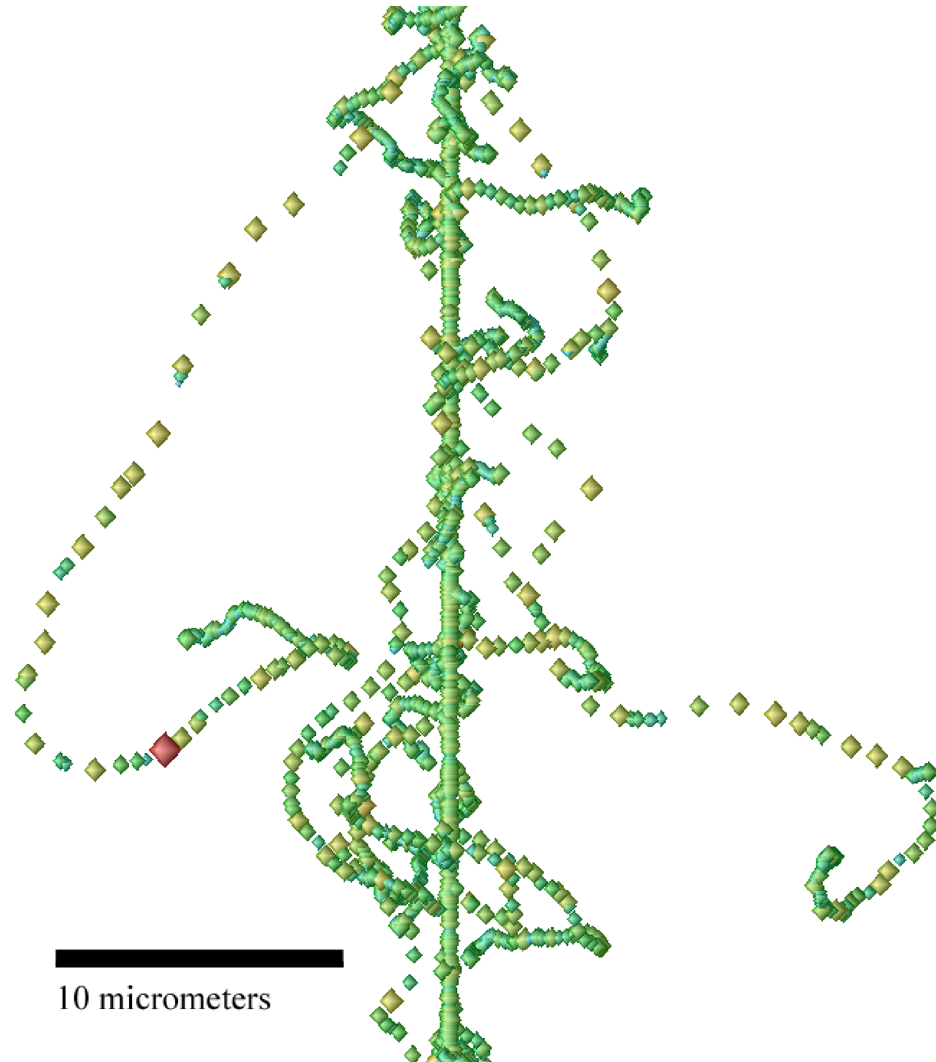

Figure 4.10 Representation of a the energy deposition from δ-rays generated by a single 560 MeV N ion incident on a large silicon structure. Each box represents the energy deposited by δ-rays in a specific region. The magnitude of energy deposited at each location is represented as color intensity, where warmer colors are larger energy deposition events.

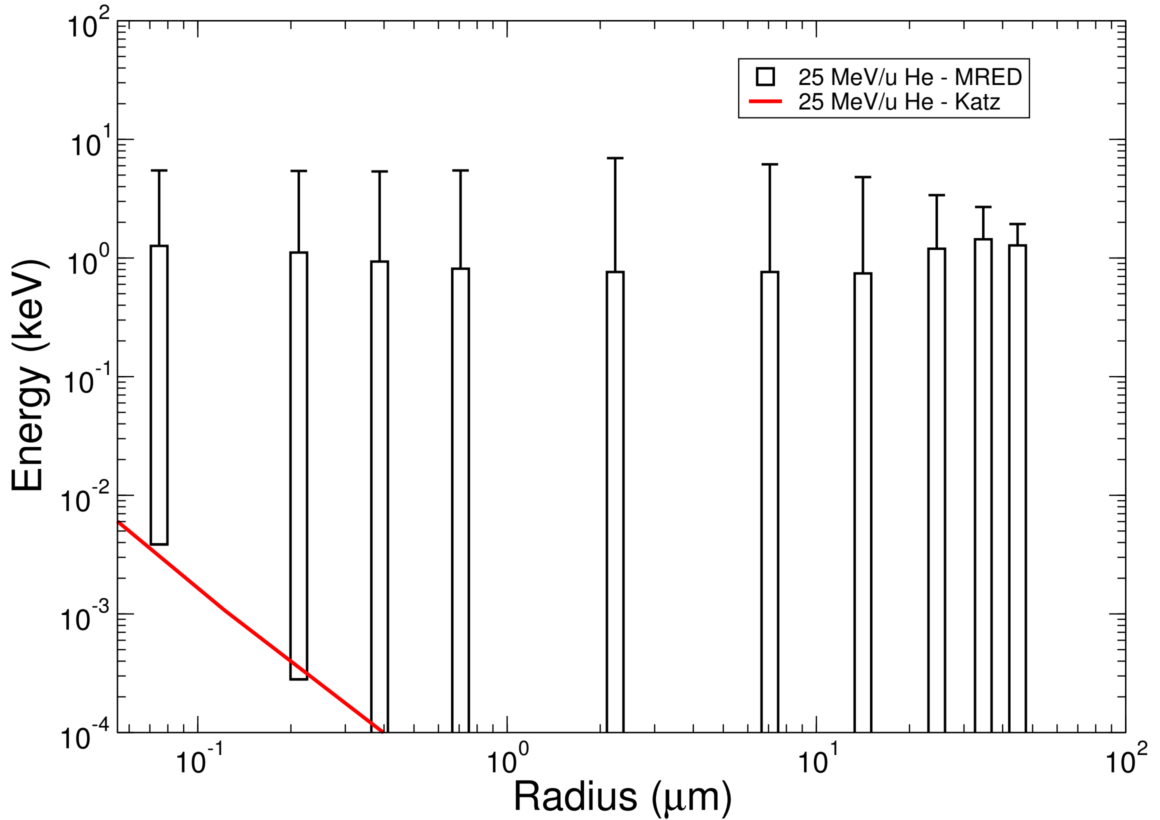

Figure 4.11 Simulation results show good agreement for energy deposited within a 50 nm cube by the Katz model (solid red line) and MRED for 25 MeV/u He. The lower edge of the box is the average energy, the upper edge of the box is the 90th percentile event, and the whisker is the largest energy deposition event. While the average energy within a 50 nm cube shows a strong dependence on the radial distance, MRED shows that large energy deposition events occur at radial distances greater than 10 μm.

model expectation represents the total energy deposited within a cylindrical shell for a single ion event. Figures 4.11 and 4.12 demonstrate that the Katz model contains no information regarding the frequency or magnitude of individual energy deposition events involving δ-rays. Individual scattering events may deposit significantly more energy within a 50 nm cube than the average would predict, as illustrated by the 90th percentile and extreme values shown in Figures 4.11 and 4.12. Information regarding the magnitude of energy deposited and spatial resolution of individual δ-ray scattering events is lost when averaging the total energy deposited in large volumes, as in the

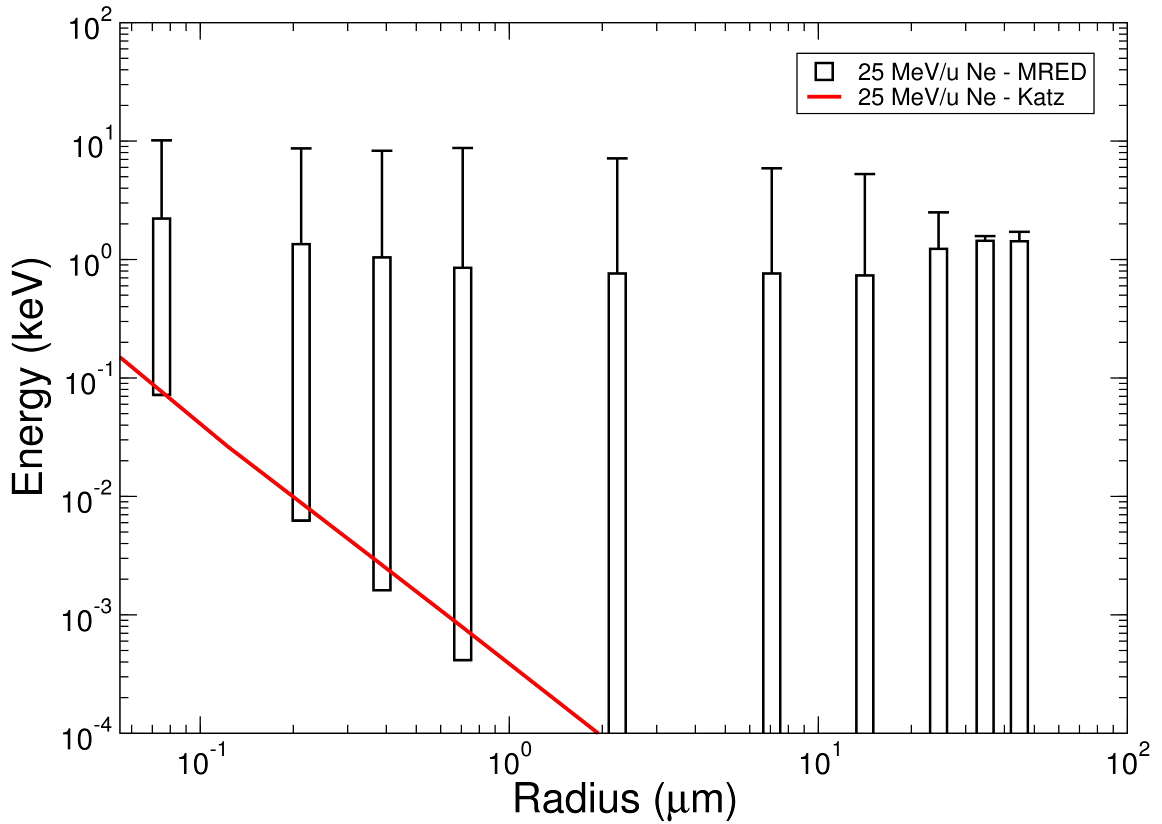

Figure 4.12 Simulation results show good agreement for energy deposited within a 50 nm cube by the Katz model (solid red line) and MRED for 25 MeV/u Ne. The lower edge of the box is the average energy, the upper edge of the box is the 90th percentile event, and the whisker is the largest energy deposition event. Large energy deposition events are again shown to occur at radial distances larger than 10 μm.

Katz model.

MRED indicates that δ-ray scattering events can deposit up to 10 keV of energy within a 50 nm cube at radial distances tens of micrometers away from the incident ion trajectory. By contrast, the average energy obtained from Katz model is less than 3.6 eV, the average energy required to produce a single *eh* pair in silicon, after several hundred nanometers for both 25 MeV/u He and Ne. Under-predicting the magnitude of energy deposited results in inaccurate charge generation and collection profiles. Scaling the expected energy deposition obtained using the Katz model into small volumes introduces error and results in inaccurate conditions for evaluating the device response. Figures 4.11 and 4.12 demonstrate that MRED captures a level of detail greater than the Katz model provides, allowing further analysis of δ-ray events and their impact on device response.

Events occurring more than 25 μm from the incident ion trajectory are near the maximum range of δ-rays generated by 25 MeV/u He and Ne and occur with a frequency up to six orders of magnitude lower than those of events at smaller radial distances. Fifty micrometers is therefore used as the evaluation limit in these simulations. The δ-rays involved in energy deposition events at radial distances greater than 25 μm are near their stopping range, which results in a reduction in the maximum energy deposition event and increase in the 90th percentile event as seen in Figures 4.11 and 4.12.

The differential energy spectrum $f(E, R)$ is represented as a cumulative energy distribution by the expression

$$\frac{d}{dx}F(E_i, R) = \frac{1}{\theta(R)N}\frac{l_{cube}}{x}\sum_{j\geq i}^{\infty} f(E_i, R) \tag{4.1}$$

where R is the orthogonal distance from the incident particle trajectory, N is the number of incident particles evaluated, l_{cube} is the side length of an evaluation volume

parallel to the z-axis, x is the ion path length through the target material, $\theta(R)$ is the (one-dimensional) solid angle subtended by a cubic volume at an orthogonal distance R from the incident particle trajectory, and $f(E, R)$ is the differential energy distribution. The formulation of Equation 4.1 for a single ionizing particle event represents the probability per radian of observing a δ-ray energy deposition event greater than or equal to E_i. Equivalently, Equation 4.1 represents the probability of a single ionizing particle event depositing a given amount of energy, E_i, or more within a cube with dimensions l_{cube} at a distance R. Normalizing to the thickness of the evaluation volume, l_{cube}, and total thickness of the target material, x, reduces the problem to a two dimensional space in the plane normal (the $y - z$ plane) to the incident ion trajectory. Because the target geometry is cylindrically symmetric about the incident ion path, normalizing to the angle θ allows a direct comparison of the probability to observe events of a given energy magnitude or greater at different radial distances from the incident ion trajectory.

From this, relationships about the frequency of δ-ray events at different radial distances can be inferred. When Equation 4.1 evaluates close to unity, this implies a high likelihood of observing an event of a given magnitude within a geometric volume at a particular distance. A reduction in the frequency of events with increasing distance indicates the termination of δ-ray trajectories.

Figure 4.13 plots the cumulative energy distribution calculated by Equation 4.1 as a function of radial distance for one thousand simulated particle events. Data points are plotted for energy deposition events greater than or equal to 1.8 keV and 3.2 keV within a 50 nm cube for 15 MeV/u and 40 MeV/u Ne. These incident ion energies are representative of several energy tunes available at the TAMU cyclotron facility. The corresponding LETs are 2.6 MeV·cm^2/mg and 1.2 MeV·cm^2/mg, respectively. Scattering and stopping of δ-rays is evident in Figure 4.13 due to the construction

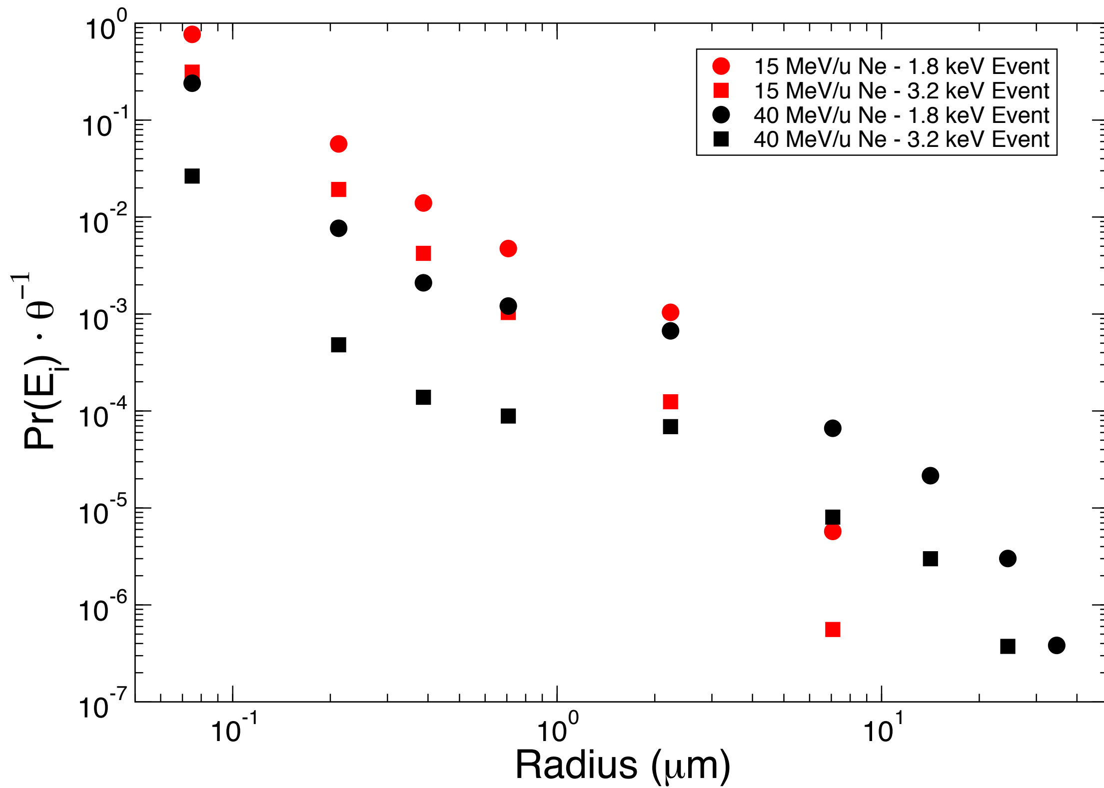

Figure 4.13 Cumulative energy distribution as a function of radial distance for 15 MeV/u and 40 MeV/u Ne ions. Results show the frequency of δ-ray energy deposition events depend on LET and energy of the incident particle.

of Equation 4.1 and is shown by the decreasing probability of events with increasing distance. Figure 4.13 also indicates that smaller energy deposition events occur much more frequently than larger energy deposition events as shown by the 1.8 keV curves compared to the 3.2 keV curves. The relationships shown in Figure 4.13 also show that while large energy deposition events, on the order of 1 keV or more, may occur at radial distances tens of micrometers from an incident ion path, as indicated in Figures 4.11 and 4.12, the likelihood of such events occurring decreases with increasing distance from the incident ion path.

This suggests that the regions most likely to be affected by δ-rays in a single ionizing particle event are likely to occur within five micrometers surrounding the

incident ion strike location, the distance at which the likelihood of an event depositing sufficient energy to exceed the estimated critical charge of a 22 nm SRAM falls below $Pr(E_i) = 10^{-6}$.

Figure 4.13 also illustrates the role of incident ion LET and energy in δ-ray events. At radii near the incident ion trajectory, higher LET particles have a higher probability of depositing large amounts of energy than lower LET particles. This is easily observed in the relative frequency of 1.8 keV energy deposition events for 15 MeV/u Ne compared to 40 MeV/u Ne. This is due to the generation of many low-energy, short-range δ-rays depositing energy around the incident ion's trajectory. The maximum transferable energy from Equation 2.12 limits the radial extent of the ion track radius, as shown by decreasing probability of energy deposition events with increasing distance from the incident ion trajectory. Consequently, higher energy incident particles can produce undesirable effects in microelectronics at larger radial distances and with greater frequency than lower energy ions.

Monte-Carlo simulation results indicate that in technology nodes where less than 0.5 fC of charge result in circuit-level effects, δ-rays may contribute to the upset error rate. A comparison of MRED with the Katz model demonstrates average track structure models alone are inadequate in capturing the device response. The probability of δ-ray related effects exhibits a strong dependence on both incident ion energy and LET. Additionally, the likelihood of δ-ray induced effects exhibits a strong dependence on radial distance from the incident ion path.

These results have strong implications for ground-based parts qualification testing and space radiation environments, where varying incident ion energy and LET result in differing contributions from δ-rays to device and circuit level effects.

Chapter 5

Summary and Conclusions

Evidence of single electron-induced SEU in 28 and 45 nm CMOS SRAMs is presented. Energetic electrons are generated by exposure of the SRAMs to an X-ray source and an aluminum attenuator.

The experimental SEU probabilities depend exponentially on applied bias, consistent with previous experimental results obtained with muons and low-energy protons. No errors were observed in functionality and parametric testing before and after irradiation of all test chips under all applied bias conditions. This demonstrates that test chips remained stable during X-ray irradiation. Thus, errors are not due to "weak bits" or photocurrents resulting from the collective energy deposition of the X-rays. Instead, experimental results and analysis strongly suggest that the observed errors result from scattering of single energetic electrons within SRAM cells.

In the space radiation environment, the event rate of electron-induced SEU is low under nominal bias conditions at geosynchronous orbits for the devices that were evaluated. Similarly, electron-induced SEUs in the Jovian environment are predicted to be rare events occuring slightly more frequently than in the near-Earth environment. Simulation results suggest proton SEU event rates in the Europa environment are likely to remain a much higher concern for SEUs in modern sub-65 nm SRAMs, this is consistent with previous estimates for solar particle events and the near-Earth trapped radiation environment. However, operating microelectronic systems in power-saving or quiescent mode would significantly increase the likelihood of electron-induced SEUs contributing to anomalous behavior in the onboard electronics systems while within the Jovian electron belts.

Monte Carlo radiation transport simulation results indicate that in technology nodes where less than 0.5 fC of charge result in circuit-level effects, δ-rays generated in heavy-ion irradiation may contribute to the single- and multiple-bit error rate. Error rates of δ-ray and electron-induced upsets for SRAMs in ground-based parts-qualification and the space radiation environment are likely dominated by extreme energy deposition events. A comparison of MRED with the Katz model demonstrates average track-structure models alone are inadequate in capturing the SEU response of small sensitive geometries with low critical charge that are susceptible to electron (or δ-ray) effects. The probability of δ-ray related effects exhibits a strong dependence on the incident ion species, energy, and LET. Additionally, the probability of δ-ray induced effects exhibits a strong dependence on radial distance from the incident ion trajectory. These results have strong implications for ground-based parts qualification testing and space radiation environments, where varying incident ion energy and LET result in differing contributions from δ-rays to device and circuit level effects.

Moreover, electron-induced upsets have only been observed to occur at measurable rates under reduced bias conditions for SRAMs fabricated in present-generation technology nodes. This suggests that the overall contribution of energetic electrons to error rates is small in current-generation technology. The conclusion being that electronics designed to operate with ultra-low power will likely exhibit higher relative sensitivity to energetic electron-induced upsets. This represents an additional design concern for both space and terrestrial environments, to avoid unexpectedly high SEU error rates from lightly ionizing particles.

Bibliography

[1] K. P. Rodbell, D. F. Heidel, H. Tang, M. Gordon, P. Oldiges, and C. Murray, "Low-energy proton-induced single-event-upsets in 65 nm node, silicon-on-insulator, latches and memory cells," *IEEE Trans. Nucl. Sci.*, vol. 54, pp. 2474–2479, Dec. 2007.

[2] B. D. Sierawski, M. H. Mendenhall, R. A. Reed, M. A. Clemens, R. A. Weller, R. D. Schrimpf, E. W. Blackmore, M. Trinczek, B. Hitti, J. A. Pellish, R. C. Baumann, S.-J. Wen, R. Wong, and N. Tam, "Muon-induced single event upsets in deep-submicron technology," *IEEE Trans. Nucl. Sci.*, vol. 57, pp. 3273–3278, Dec. 2010.

[3] S. Bourdarie and M. Xapsos, "The near-earth space radiation environment," *IEEE Trans. Nucl. Sci.*, vol. 55, pp. 1810–1832, Aug. 2008.

[4] M. Xapsos, P. M. O'Neill, and T. P. O'Brien, "Near-earth space radiation models," *IEEE Trans. Nucl. Sci.*, vol. 60, pp. 1691–1705, June 2013.

[5] R. A. Weller, A. L. Sternberg, L. W. Massengill, R. D. Schrimpf, and D. M. Fleetwood, "Evaluating average and atypical response in radiation effects simulations," *IEEE Trans. Nucl. Sci.*, vol. 50, pp. 2265–2271, Dec. 2003.

[6] M. Raine, M. Gaillardin, J.-E. Sauvestre, O. Flament, A. Bournel, and V. Aubry-Fortuna, "Effect of the ion mass and energy on the response of 70-nm SOI transistors to the ion deposited charge by direct ionization," *IEEE Trans. Nucl. Sci.*, vol. 57, pp. 1892–1899, Aug. 2010.

[7] M. Raine, G. Hubert, M. Gaillardin, L. Artola, P. Paillet, S. Girard, J.-E. Sauvestre, and A. Bournel, "Impact of the radial ionization profile on SEE prediction for SOI transistors and SRAMs beyond the 32-nm technological node," *IEEE Trans. Nucl. Sci.*, vol. 58, pp. 840–847, June 2011.

[8] M. Raine, A. Valentin, M. Gaillardin, and P. Paillet, "Improved simulation of ion track structures using new Geant4 models–impact on the modeling of advanced technologies response," *IEEE Trans. Nucl. Sci.*, vol. 59, pp. 2697–2703, Dec. 2012.

[9] M. P. King, R. A. Reed, R. A. Weller, M. H. Mendenhall, R. D. Schrimpf, M. L. Alles, E. C. Auden, S. E. Armstrong, and M. Asai, "The impact of delta-rays on single-event upsets in highly scaled SOI SRAMs," *IEEE Trans. Nucl. Sci.*, vol. 57, pp. 3169–3175, Jan. 2010.

[10] M. P. King, R. A. Reed, R. A. Weller, M. H. Mendenhall, R. D. Schrimpf, N. D. Pate, E. C. Auden, and S. L. Weeden-Wright, "Radial characteristics of heavy-ion track structure and implications of delta-ray events for microelectronics," *Appl. Phys. Lett.*, vol. 101, pp. 053509–053509–3, Aug. 2012.

[11] J. Barak, M. Murat, and A. Akkerman, "SEU due to electrons in silicon devices with nanometric sensitive volumes and small critical charge," *Nucl. Instrum. Meth. B*, vol. 287, pp. 113–119, Sept. 2012.

[12] T. Loveless, M. L. Alles, D. R. Ball, K. M. Warren, and L. W. Massengill, "Parametric variability affecting 45 nm SOI SRAM single event upset cross-sections," *IEEE Trans. Nucl. Sci.*, vol. 57, no. 6, pp. 3228–3233, 2010.

[13] D. F. Heidel, P. W. Marshall, K. A. LaBel, J. R. Schwank, K. P. Rodbell, M. C. Hakey, M. D. Berg, P. E. Dodd, M. R. Friendlich, A. D. Phan, C. M. Seidleck, M. R. Shaneyfelt, and M. A. Xapsos, "Low energy proton single-event-upset test results on 65 nm SOI SRAM," *IEEE Trans. Nucl. Sci.*, vol. 55, pp. 3394–3400, Dec. 2008.

[14] D. F. Heidel, P. W. Marshall, J. A. Pellish, K. P. Rodbell, K. A. LaBel, J. R. Schwank, S. Rauch, M. C. Hakey, M. D. Berg, and C. Castaneda, "Single-event upsets and multiple-bit upsets on a 45 nm SOI SRAM," *IEEE Trans. Nucl. Sci.*, vol. 56, pp. 3499–3504, Dec. 2009.

[15] B. D. Sierawski, J. A. Pellish, R. A. Reed, R. D. Schrimpf, K. M. Warren, R. A. Weller, M. H. Mendenhall, J. D. Black, A. D. Tipton, M. A. Xapsos, R. C. Baumann, X. Deng, M. J. Campola, M. R. Friendlich, H. S. Kim, A. M. Phan, and C. M. Seidleck, "Impact of low-energy proton induced upsets on test methods and rate predictions," *IEEE Trans. Nucl. Sci.*, vol. 56, pp. 3085–3092, Dec. 2009.

[16] B. D. Sierawski, R. A. Reed, M. H. Mendenhall, R. A. Weller, R. D. Schrimpf, S. Wen, R. Wong, N. Tam, and R. C. Baumann, "Effects of scaling on muon-induced soft errors," *2011 IEEE International Reliability Physics Symposium*, p. 3, April 2011.

[17] National Aeronautics and Space Administration – Jet Propulsion Laboratory, "Juno Launch - Press Kit," *[Online] http://www.jpl.nasa.gov/news/press_kits/JunoLaunch.pdf*, Aug., 2011.

[18] National Aeronautics and Space Administration, "James Webb Space Telescope – Frequently Asked Questions," *[Online] http://jwst.nasa.gov/faq.html*.

[19] H. Tang, C. Murray, G. Fiorenza, K. P. Rodbell, and M. Gordon, "Importance of BEOL Modeling in Single Event Effect Analysis," *IEEE Trans. Nucl. Sci.*, vol. 54, no. 6 Part 1, pp. 2162–2167, 2007.

[20] H. Tang, C. Murray, G. Fiorenza, K. P. Rodbell, and D. F. Heidel, "Modeling of alpha-induced single event upsets for 45 nm node SOI devices using realistic C4 and 3D circuit geometries," *IEEE Trans. Nucl. Sci.*, vol. 56, no. 6, pp. 3093–3097, 2009.

[21] B. D. Sierawski, *The role of singly-charged particles in microelectronics reliability.* PhD thesis, Ph.D. dissertation, Electrical Engineering and Computer Science Dept., Vanderbilt University, Nashville, TN., 2011.

[22] J. T. Wallmark and S. M. Marcus, "Minimum size and maximum packing density of nonredundant semiconductor devices," *Proceedings of the IRE*, vol. 50, no. 3, pp. 286–298, 1962.

[23] P. K. Grieder, *Cosmic rays at Earth.* Access Online via Elsevier, 2001.

[24] J. F. Ziegler, M. D. Ziegler, and J. P. Biersack, "Srim–the stopping and range of ions in matter (2010)," *Nucl. Instrum. Meth. B*, vol. 268, no. 11, pp. 1818–1823, 2010.

[25] H. Bichsel, D. Groom, and S. Klein, "Passage of particles through matter," *Physics Letters B*, vol. 592, p. 2004, 2010.

[26] R. Pehl, F. Goulding, D. Landis, and M. Lenzlinger, "Accurate determination of the ionization energy in semiconductor detectors," *Nuclear Instruments and Methods*, vol. 59, no. 1, pp. 45–55, 1968.

[27] R. Ryan, "Precision measurements of the ionization energy and its temperature variation in high purity silicon radiation detectors," *IEEE Trans. Nucl. Sci.*, vol. 20, no. 1, pp. 473–480, 1973.

[28] F. Scholze, H. Henneken, P. Kuschnerus, H. Rabus, M. Richter, and G. Ulm, "Determination of the electron–hole pair creation energy for semiconductors from the spectral responsivity of photodiodes," *Nucl. Instrum. Meth. A*, vol. 439, no. 2, pp. 208–215, 2000.

[29] H. Bichsel, "Straggling in thin silicon detectors," *Reviews of Modern Physics*, vol. 60, no. 3, p. 663, 1988.

[30] W. Stapor and P. McDonald, "Practical approach to ion track energy distribution," *J. Appl. Phys.*, vol. 64, p. 4430, 1988.

[31] J. W. Howard, R. C. Block, H. Dussault, W. Stapor, P. McDonald, A. Knudson, and M. R. Pinto, "A novel approach for measuring the radial distribution of charge in a heavy-ion track," *IEEE Trans. Nucl. Sci.*, vol. 41, pp. 2077–2084, Jan. 2002.

[32] A. S. Kobayashi, A. L. Sternberg, L. W. Massengill, R. D. Schrimpf, and R. A. Weller, "Spatial and temporal characteristics of energy deposition by protons and alpha particles in silicon," *IEEE Trans. Nucl. Sci.*, vol. 51, no. 6, pp. 3312–3317, 2004.

[33] P. E. Dodd, O. Musseau, M. R. Shaneyfelt, F. W. Sexton, C. D'hose, G. Hash, M. Martinez, R. Loemker, J. Leray, and P. Winokur, "Impact of ion energy on single-event upset," *IEEE Trans. Nucl. Sci.*, vol. 45, no. 6, pp. 2483–2491, 1998.

[34] P. E. Dodd, "Mechanisms and modeling of single-event upset," *osti.gov*, Jan. 1998.

[35] P. E. Dodd, A. Shaneyfelt, K. Horn, D. Walsh, G. L. Hash, T. A. Hill, B. L. Draper, J. R. Schwank, F. Sexton, and P. Winokur, "SEU-sensitive volumes in bulk and SOI SRAMs from first-principles calculations and experiments," *IEEE Trans. Nucl. Sci.*, vol. 48, no. 6, pp. 1893–1903, 2001.

[36] R. A. Reed, P. W. Marshall, H. Kim, P. McNulty, B. Fodness, T. Jordan, R. Reedy, C. Tabbert, M. Liu, and W. Heikkila, "Evidence for angular effects in proton-induced single-event upsets," *IEEE Trans. Nucl. Sci.*, vol. 49, no. 6, pp. 3038–3044, 2002.

[37] A. S. Kobayashi, D. R. Ball, K. M. Warren, R. A. Reed, N. Haddad, M. H. Mendenhall, R. D. Schrimpf, and R. A. Weller, "The effect of metallization layers on single event susceptibility," *IEEE Trans. Nucl. Sci.*, vol. 52, pp. 2189–2193, Dec. 2005.

[38] R. A. Reed, R. A. Weller, R. D. Schrimpf, M. H. Mendenhall, K. M. Warren, and L. W. Massengill, "Implications of nuclear reactions for single event effects test methods and analysis," *IEEE Trans. Nucl. Sci.*, vol. 53, no. 6, pp. 3356–3362, 2006.

[39] R. A. Reed, R. A. Weller, M. H. Mendenhall, J. Lauenstein, K. Warren, J. Pellish, R. D. Schrimpf, B. D. Sierawski, L. W. Massengill, and P. E. Dodd, "Impact of ion energy and species on single event effects analysis," *IEEE Trans. Nucl. Sci.*, vol. 54, no. 6, pp. 2312–2321, 2007.

[40] K. M. Warren, R. A. Weller, B. D. Sierawski, R. A. Reed, M. H. Mendenhall, R. D. Schrimpf, L. W. Massengill, M. E. Porter, J. D. Wilkinson, K. A. LaBel, and J. H. Adams, "Application of RADSAFE to model the single event upset response of a 0.25 μm CMOS SRAM," *IEEE Trans. Nucl. Sci.*, vol. 54, no. 4, pp. 898–903, 2007.

[41] H. Bethe, "Zur theorie des durchgangs schneller korpuskularstrahlen durch materie," *Annalen der Physik*, vol. 397, no. 3, pp. 325–400, 1930.

[42] H. Bethe, "Bremsformel für elektronen relativistischer geschwindigkeit," *Zeitschrift für Physik*, vol. 76, no. 5-6, pp. 293–299, 1932.

[43] U. Fano, "Penetration of protons, alpha particles, and mesons," *Studies in Penetration of Charged Particles in Matter*, no. 39, p. 287, 1964.

[44] F. Salvat, J. Fernández-Varea, and J. Sempau, "PENELOPE-2008: A code system for Monte Carlo simulation of electron and photon transport," *[Online] http://www.oecd-nea.org/science/pubs/2009/nea6416-penelope.pdf.*

[45] E. Segre, *Nuclei and particles: an introduction to nuclear and subnuclear physics.* WA Benjamin New York, 1964.

[46] M. J. Berger and S. M. Seltzer, "Stopping powers and ranges of electrons and positrons," tech. rep., Dec. 1982.

[47] G. Knoll, *Radiation detection and measurement.* 2010.

[48] E. L. Alpen, *Radiation biophysics.* Access Online via Elsevier, 1997.

[49] B. L. Henke, E. M. Gullikson, and J. C. Davis, "X-ray interactions: photoabsorption, scattering, transmission, and reflection at E = 50-30,000 eV, Z = 1-92," *Atomic data and nuclear data tables*, 1993.

[50] J. Ingle and S. Crouch, "Spectrochemical measurements," *Spectrochemical Analysis (Prentice Hall, New Jersey, USA, 1988)*, 1988.

[51] G. Semeraro, G. Magklis, R. Balasubramonian, D. H. Albonesi, S. Dwarkadas, and M. L. Scott, "Energy-efficient processor design using multiple clock domains with dynamic voltage and frequency scaling," in *IEEE International Symposium on High-Performance Computer Architecture*, pp. 29–40, IEEE, 2002.

[52] H. David, C. Fallin, E. Gorbatov, U. R. Hanebutte, and O. Mutlu, "Memory power management via dynamic voltage/frequency scaling," in *Proceedings of the 8th ACM International Conference on Autonomic Computing*, pp. 31–40, ACM, 2011.

[53] B. Haran, A. Kumar, L. Adam, J. Chang, V. Basker, S. Kanakasabapathy, D. Horak, S. Fan, J. Chen, and J. Faltermeier, "22 nm technology compatible fully functional 0.1 μm^2 6T-SRAM cell," *IEEE International Electron Devices Meeting, 2008. IEDM 2008*, pp. 1–4, 2008.

[54] F. McLean and T. Oldham, "Charge funneling in n-and p-type si substrates," *IEEE Trans. Nucl. Sci.*, vol. 29, no. 6, pp. 2017–2023, 1982.

[55] T. Oldham and F. McLean, "Charge collection measurements for heavy ions incident on n-and p-type silicon," *IEEE Trans. Nucl. Sci.*, vol. 30, no. 6, pp. 4493–4500, 1983.

[56] T. Oldham, F. McLean, and J. Hartman, "Revised funnel calculations for heavy particles with high dE/dx," *IEEE Trans. Nucl. Sci.*, vol. 33, no. 6, pp. 1646–1650, 1986.

[57] P. Dodd, F. Sexton, and P. Winokur, "Three-dimensional simulation of charge collection and multiple-bit upset in Si devices," *IEEE Trans. Nucl. Sci.*, vol. 41, no. 6, pp. 2005–2017, 1994.

[58] L. D. Edmonds, "Charge collection from ion tracks in simple epi diodes," *IEEE Trans. Nucl. Sci.*, vol. 44, no. 3, pp. 1448–1463, 1997.

[59] L. D. Edmonds, "Electric currents through ion tracks in silicon devices," *IEEE Trans. Nucl. Sci.*, vol. 45, no. 6, pp. 3153–3164, 1998.

[60] G. Hubert, J.-M. Palau, P. Roche, B. Sagnes, J. Gasiot, and M. Calvet, "Study of basic mechanisms induced by an ionizing particle on simple structures," *IEEE Trans. Nucl. Sci.*, vol. 47, no. 3, pp. 519–526, 2000.

[61] L. D. Edmonds, "A theoretical analysis of steady-state charge collection in simple diodes under high-injection conditions," *IEEE Trans. Nucl. Sci.*, vol. 57, no. 2, pp. 818–830, 2010.

[62] L. D. Edmonds, "A proposed transient version of the adc charge-collection model tested against tcad," *IEEE Trans. Nucl. Sci.*, vol. 58, no. 1, pp. 296–304, 2011.

[63] L. D. Edmonds, "A theoretical analysis of the role of ambipolar diffusion in charge-carrier transport in a quasi-neutral region under high injection," *IEEE Trans. Nucl. Sci.*, vol. 58, no. 5, pp. 2459–2469, 2011.

[64] L. D. Edmonds, "Extension of the ADC charge-collection model to include multiple junctions," *IEEE Trans. Nucl. Sci.*, vol. 58, no. 6, pp. 3333–3342, 2011.

[65] N. Hooten, L. Edmonds, W. Bennett, J. Ahlbin, N. Dodds, R. Reed, R. Schrimpf, and R. Weller, "The significance of high-level carrier generation conditions for charge collection in irradiated devices," *IEEE Trans. Nucl. Sci.*, vol. 59, no. 6, pp. 2710–2721, 2012.

[66] S. DasGupta, A. Witulski, B. Bhuva, M. Alles, R. Reed, O. Amusan, J. Ahlbin, R. Schrimpf, and L. Massengill, "Effect of well and substrate potential modulation on single event pulse shape in deep submicron CMOS," *IEEE Trans. Nucl. Sci.*, vol. 54, no. 6, pp. 2407–2412, 2007.

[67] L. W. Massengill, "SEU modeling and prediction techniques," in *1993 IEEE NSREC Short Course*, (Pascataway, NJ), IEEE Publishing, 1993.

[68] M. J. Gadlage, R. D. Schrimpf, J. M. Benedetto, P. H. Eaton, D. G. Mavis, M. Sibley, K. Avery, and T. L. Turflinger, "Single event transient pulse widths in digital microcircuits," *IEEE Trans. Nucl. Sci.*, vol. 51, no. 6, pp. 3285–3290, 2004.

[69] J. S. Kauppila, A. L. Sternberg, M. L. Alles, A. M. Francis, J. Holmes, O. A. Amusan, and L. W. Massengill, "A bias-dependent single-event compact model implemented into BSIM4 and a 90 nm CMOS process design kit," *IEEE Trans. Nucl. Sci.*, vol. 56, no. 6, pp. 3152–3157, 2009.

[70] K. M. Warren, B. D. Sierawski, R. A. Weller, and R. A. Reed, "Predicting thermal neutron-induced soft errors in static memories using TCAD and physics-based monte carlo simulation tools," *IEEE Elec. Dev. Lett.*, Jan. 2007.

[71] A. Kauppila, B. L. Bhuva, J. Kauppila, L. W. Massengill, and W. Holman, "Impact of process variations on SRAM single event upsets," *IEEE Trans. Nucl. Sci.*, vol. 58, no. 3, pp. 834–839, 2011.

[72] A. Kauppila, B. Bhuva, L. Massengill, W. Holman, and D. Ball, "Impact of process variations and charge sharing on the single-event-upset response of flip-flops," *IEEE Trans. Nucl. Sci.*, vol. 58, no. 6, pp. 2658–2663, 2011.

[73] M. Buehler and B. Blaes, "Alpha-particle sensitive test SRAMs," *IEEE Trans. Nucl. Sci.*, vol. 37, no. 6, pp. 1849–1854, 1990.

[74] D. Roth, P. McNulty, W. Abdel-Kader, L. Strauss, and E. Stassinopoulos, "Monitoring SEU parameters at reduced bias CMOS SRAM," *Nuclear Science, IEEE Transactions on*, vol. 40, no. 6, pp. 1721–1724, 1993.

[75] J. Barak, J. Levinson, A. Akkerman, E. Adler, A. Zentner, D. David, Y. Lifshitz, M. Hass, B. Fischer, M. Schlogl, *et al.*, "Scaling of SEU mapping and cross section, and proton induced SEU at reduced supply voltage," *IEEE Trans. Nucl. Sci.*, vol. 46, no. 6, pp. 1342–1353, 1999.

[76] J. Barak, A. Haran, E. Adler, M. Azoulay, J. Levinson, A. Zentner, D. David, B. Fischer, M. Heiss, and D. Betel, "Use of light-ion-induced SEU in devices under reduced bias to evaluate their SEU cross section," *IEEE Trans. Nucl. Sci.*, vol. 51, no. 6, pp. 3486–3493, 2004.

[77] Semiconductor Industry Association (SIA), "International roadmap for semiconductors 2012 update," *[Online] http://www.itrs.net*, 2012.

[78] R. Reed, P. McNulty, and W. Abdel-Kader, "Implications of angle of incidence in SEU testing of modern circuits," *IEEE Trans. Nucl. Sci.*, vol. 41, no. 6, pp. 2049–2054, 1994.

[79] R. Reed, M. Carts, P. Marshall, C. Marshall, O. Musseau, P. McNulty, D. Roth, S. Buchner, J. Melinger, and T. Corbiere, "Heavy ion and proton-induced single event multiple upset," *IEEE Trans. Nucl. Sci.*, vol. 44, no. 6, pp. 2224–2229, 1997.

[80] R. A. Reed, P. W. Marshall, H. S. Kim, P. J. McNulty, B. Fodness, T. Jordan, R. Reedy, C. Tabbert, M. S. Liu, W. Heikkila, *et al.*, "Evidence for angular effects in proton-induced single-event upsets," *IEEE Trans. Nucl. Sci.*, vol. 49, no. 6, pp. 3038–3044, 2002.

[81] D. F. Heidel, K. P. Rodbell, P. Oldiges, M. Gordon, H. Tang, E. Cannon, and C. Plettner, "Single-event-upset critical charge measurements and modeling of 65 nm silicon-on-insulator latches and memory cells," *IEEE Trans. Nucl. Sci.*, vol. 53, no. 6, pp. 3512–3517, 2006.

[82] J. F. Ziegler and W. A. Lanford, "Effect of cosmic rays on computer memories," *Science*, vol. 206, no. 4420, pp. 776–788, 1979.

[83] P. V. Dressendorfer, J. M. Soden, J. J. Harrington, and T. V. Nordstrom, "The effects of test conditions on MOS radiation-hardness results," *IEEE Trans. Nucl. Sci.*, vol. 28, pp. 4281–4287, Dec. 1981.

[84] K. F. Galloway and R. D. Schrimpf, "MOS device degradation due to total dose ionizing radiation in the natural space environment: a review," *Microelectronics Journal*, vol. 21, pp. 67–81, Jan. 1990.

[85] D. M. Fleetwood, P. Winokur, R. Reber, T. Meisenheimer, J. R. Schwank, M. R. Shaneyfelt, and L. Riewe, "Effects of oxide traps, interface traps, and "border traps"on metaloxidesemiconductor devices," *J. Appl. Phys.*, vol. 73, no. 10, pp. 5058–5074, 1993.

[86] D. M. Fleetwood, M. R. Shaneyfelt, and W. Warren, "Border traps: issues for MOS radiation response and long-term reliability," *Microelectronics Reliability*, Jan. 1995.

[87] J. T. Schott and M. H. Zugich, "Pattern imprinting in CMOS static RAMs from Co-60 irradiation," *IEEE Trans. Nucl. Sci.*, vol. 34, pp. 1403–1407, Dec. 1987.

[88] D. M. Fleetwood and P. V. Dressendorfer, "A simple method to identify radiation and annealing biases that lead to worst-case CMOS static RAM postirradiation response," *IEEE Trans. Nucl. Sci.*, vol. 34, pp. 1408–1413, Dec. 1987.

[89] J. A. Felix, P. E. Dodd, M. R. Shaneyfelt, J. R. Schwank, and G. L. Hash, "Radiation response and variability of advanced commercial foundry technologies," *IEEE Trans. Nucl. Sci.*, vol. 53, pp. 3187–3194, Dec. 2006.

[90] I. Arimura, R. A. Kennerud, and L. Kolb, "Hardness assured device specification for 4K X 1 CMOS/SOS static RAM," *Boeing Aerospace Co. Report D180-28295-2 under Contract No. DNA*, 1985.

[91] H. J. Barnaby, "Total-ionizing-dose effects in modern CMOS technologies," *IEEE Trans. Nucl. Sci.*, vol. 53, pp. 3103–3121, Dec. 2006.

[92] X. Yao, N. Hindman, L. T. Clark, K. E. Holbert, D. R. Alexander, and W. M. Shedd, "The impact of total ionizing dose on unhardened SRAM cell margins," *IEEE Trans. Nucl. Sci.*, vol. 55, pp. 3280–3287, Dec. 2008.

[93] D. Nair, R. Gale, and T. Karp, "Total ionizing dose effects on data retention capabilities of battery-backed CMOS SRAM," *IEEE Trans. Nucl. Sci.*, 2013.

[94] B. Bhuva, R. L. Johnson, R. S. Gyurcsik, K. W. Fernald, S. E. Kernstt, W. Stapor, Campbell, AB, and M. Xapsos, "Quantification of the memory imprint effect for a charged particle environment," *IEEE Trans. Nucl. Sci.*, vol. 34, no. 6, pp. 1414–1418, 1987.

[95] G. J. Brucker, J. Wert, and P. Measel, "Transient imprint memory effect in MOS memories," *IEEE Trans. Nucl. Sci.*, vol. 33, no. 6, pp. 1483–1486, 1986.

[96] J. L. Wirth and S. C. Rogers, "The transient response of transistors and diodes to ionizing radiation," *IEEE Trans. Nucl. Sci.*, vol. 11, pp. 24–38, Nov. 1964.

[97] D. M. Long, J. R. Florian, and R. H. Casey, "Transient response model for epitaxial transistors," *IEEE Trans. Nucl. Sci.*, vol. 30, pp. 4131–4134, Dec. 1983.

[98] L. W. Massengill and S. E. Diehl-Nagle, "Transient radiation upset simulations of CMOS memory circuits," *IEEE Trans. Nucl. Sci.*, vol. 31, no. 6, pp. 1337–1343, 1984.

[99] L. W. Massengill, S. E. Diehl-Nagle, and T. F. Wrobel, "Analysis of transient radiation upset in a 2K SRAM," *IEEE Trans. Nucl. Sci.*, vol. 32, pp. 4026–4030, Dec. 1985.

[100] L. W. Massengill, S. E. Diehl, and J. S. Browning, "Dose-rate upset patterns in a 16K CMOS SRAM," *IEEE Trans. Nucl. Sci.*, vol. 33, pp. 1541–1545, Dec. 1986.

[101] A. J. Tylka, J. H. Adams Jr, P. R. Boberg, B. Brownstein, W. F. Dietrich, E. O. Flueckiger, E. L. Petersen, M. A. Shea, D. F. Smart, and E. C. Smith, "CREME96: a revision of the cosmic ray effects on micro-electronics code," *IEEE Trans. Nucl. Sci.*, vol. 44, no. 6, pp. 2150–2160, 1997.

[102] A. S. Keys, J. H. Adams, M. C. Patrick, M. A. Johnson, and J. D. Cressler, "A review of NASA's radiation-hardened electronics for space environments project," in *2008 Space Conf*, 2008.

[103] B. Sierawski, M. Mendenhall, R. Weller, R. Reed, J. Adams, J. Watts, and A. Barghouty, "CRÈME-MC: A physics-based single event effects tool," in *2010 IEEE Nucl. Sci. Symp. Conf. Rec. (NSS/MIC)*, pp. 1258–1261, IEEE, 2010.

[104] M. A. Xapsos, "Modeling the space radiation environment," in *2006 IEEE NSREC Short Course*, (Pascataway, NJ), IEEE Publishing, 2006.

[105] E. N. Parker, "The passage of energetic charged particles through interplanetary space," *Planetary and Space Science*, vol. 13, no. 1, pp. 9–49, 1965.

[106] G. Badhwar and P. O'Neill, "An improved model of galactic cosmic radiation for space exploration missions," *International Journal of Radiation Applications and Instrumentation. Part D. Nuclear Tracks and Radiation Measurements*, vol. 20, no. 3, pp. 403–410, 1992.

[107] G. D. Badhwar and P. O'Neill, "Galactic cosmic radiation model and its applications," *Advances in Space Research*, vol. 17, no. 2, pp. 7–17, 1996.

[108] J. A. Van Allen, C. E. McIlwain, and G. H. Ludwig, "Radiation observations with satellite 1958 ε," *Journal of Geophysical Research*, vol. 64, no. 3, pp. 271–286, 1959.

[109] D. M. Sawyer and J. I. Vette, "AP-8 trapped proton environment for solar maximum and solar minimum," *NASA STI/Recon Technical Report N*, vol. 77, p. 18983, 1976.

[110] J. I. Vette, "The AE-8 trapped electron model environment," *NASA STI/Recon Technical Report N*, vol. 92, p. 24228, 1991.

[111] J. L. Barth, C. Dyer, and E. Stassinopoulos, "Space, atmospheric, and terrestrial radiation environments," *IEEE Trans. Nucl. Sci.*, vol. 50, no. 3, pp. 466–482, 2003.

[112] A. S. Piet, S. Bourdarie, D. Boscher, and R. Friedel, "A model for the geostationary electron environment: POLE, from 30 keV to 5.2 MeV," *IEEE Trans. Nucl. Sci.*, vol. 53, no. 4, pp. 1844–1850, 2006.

[113] N. Divine and H. Garrett, "Charged particle distributions in jupiter's magnetosphere," *Journal of Geophysical Research: Space Physics (1978–2012)*, vol. 88, no. A9, pp. 6889–6903, 1983.

[114] H. Garrett, M. Kokorowski, I. Jun, and R. Evans, "Galileo interim radiation electron model: update 2012," 2012.

[115] H. Garrett, I. Jun, J. Ratliff, R. Evans, G. Clough, and R. McEntire, *Galileo interim radiation electron model.* Jet Propulsion Laboratory, National Aeronautics and Space Administration, 2003.

[116] H. B. Garrett, S. M. Levin, S. J. Bolton, R. W. Evans, and B. Bhattacharya, "A revised model of jupiter's inner electron belts: Updating the divine radiation model," *Geophysical research letters*, vol. 32, no. 4, 2005.

[117] E. Kobetich and R. Katz, "Energy deposition by electron beams and δ rays," *Physical Review*, vol. 170, pp. 391–396, June 1968.

[118] R. Katz and E. Kobetich, "Formation of etchable tracks in dielectrics," *Physical Review*, vol. 170, pp. 401–405, June 1968.

[119] Z. Chunxiang, D. E. Dunn, and R. Katz, "Radial distribution of dose and cross-sections for the inactivation of dry enzymes and viruses," *Radiation Protection Dosimetry*, vol. 13, no. 1, p. 4, 1985.

[120] O. Fageeha, J. Howard, and R. C. Block, "Distribution of radial energy deposition around the track of energetic charged particles in silicon," *J. Appl. Phys.*, vol. 75, no. 5, pp. 2317–2321, 1994.

[121] R. Katz and E. Kobetich, "Particle tracks in emulsion," *Physical Review*, Jan. 1969.

[122] M. A. Xapsos, "Applicability of LET to single events in microelectronic structures," *IEEE Trans. Nucl. Sci.*, vol. 39, pp. 1613–1621, Jan. 1992.

[123] M. Murat, A. Akkerman, and J. Barak, "Electron and ion tracks in silicon: Spatial and temporal evolution," *IEEE Trans. Nucl. Sci.*, vol. 55, no. 6, pp. 3046–3054, 2008.

[124] C. M. Dozier and D. B. Brown, "The use of low energy x-rays for device testing - a comparison with Co-60 radiation," *IEEE Trans. Nucl. Sci.*, vol. 30, pp. 4382–4387, Dec. 1983.

[125] D. M. Fleetwood, P. S. Winokur, L. J. Lorence, W. Beezhold, P. V. Dressendorfer, and J. R. Schwank, "The response of MOS devices to dose-enhanced low-energy radiation," *IEEE Trans. Nucl. Sci.*, vol. 33, pp. 1245–1251, Dec. 1986.

[126] R. A. Weller, M. H. Mendenhall, R. A. Reed, R. D. Schrimpf, K. M. Warren, B. D. Sierawski, and L. W. Massengill, "Monte Carlo simulation of single event effects," *IEEE Trans. Nucl. Sci.*, vol. 57, pp. 1726–1746, Aug. 2010.

[127] A. Dasgupta, D. M. Fleetwood, R. A. Reed, R. A. Weller, and M. H. Mendenhall, "Effects of metal gates and back-end-of-line materials on x-ray dose in HfO_2 gate oxide," *IEEE Trans. Nucl. Sci.*, vol. 58, no. 6, pp. 3139–3144, 2011.

[128] J. R. Schwank, D. M. Fleetwood, P. S. Winokur, P. V. Dressendorfer, D. C. Turpin, and D. T. Sanders, "The role of hydrogen in radiation-induced defect formation in polysilicon gate MOS devices," *IEEE Trans. Nucl. Sci.*, vol. 34, pp. 1152–1158, Dec. 1987.

[129] D. M. Fleetwood and P. V. Dressendorfer, "A simple method to identify radiation and annealing biases that lead to worst-case CMOS static RAM postirradiation response," *IEEE Trans. Nucl. Sci.*, vol. 34, pp. 1408–1413, Dec. 1987.

[130] S. Agostinelli, J. Allison, K. Amako, J. Apostolakis, H. Araujo, P. Arce, M. Asai, D. Axen, S. Banerjee, and G. Barrand, "Geant4—a simulation toolkit," *Nucl. Instrum. Meth. A*, vol. 506, pp. 250–303, July 2003.